NONLINEAR CIRCUITS FOR SIGNAL GENERATION AND PROCESSING IN CMOS

A Dissertation

Presented to the Faculty of the Graduate School

of Cornell University

in Partial Fulfillment of the Requirements for the Degree of

Doctor of Philosophy

by

Wooram Lee

August 2012

NONLINEAR CIRCUITS FOR SIGNAL GENERATION AND PROCESSING
IN CMOS

Wooram Lee, Ph.D.

Cornell University 2012

As Moore's law predicted, transistor scaling has continued unabated for more than half a century, resulting in significant improvement in speed, efficiency, and integration level. This has led to rapid growth of diverse computing and communications technologies, including the Internet and mobile telephony. Nevertheless, we still face the fundamental limit of noise from transistors and passive components. This noise limit becomes more critical at higher frequencies due to the decrease in intrinsic transistor gain as well as with voltage scaling that accompanies the transistor scaling. On the other hand, insufficient transistor gain and breakdown in silicon limits high-power signal generation at sub-millimeter frequencies that is essential in many security and medical applications, including detection of concealed weapons and bio/molecular spectroscopy for drug detection and breath analysis for disease diagnosis.

To go beyond these limits, we propose a new circuit design methodology inspired by nonlinear wave propagation. This method is closely related to intriguing phenomena in other disciplines of physics such as nonlinear optics, fluid mechanics, and plasma physics. Based on this, in the first part of this study, we propose a passive 20-GHz frequency divider for the first time implemented in CMOS. This device has close to ideal noise performance with no DC power consumption, which can potentially reduce overall system power and phase noise in high-frequency synthesizers. Next, to achieve sensitivity toward

the thermal noise limit, we propose a 10-GHz CMOS noise-squeezing amplifier. This amplifier enhances sensitivity of an input signal in one quadrature phase by 2.5 dB at the expense of degrading the other quadrature component. Lastly, we introduce an LC lattice to generate 2.7 V_{p-p}, 6 ps pulses in CMOS using constructive nonlinear wave interaction. The proposed lattice exhibits the sharpest pulse width achieved for high-amplitude pulses (>1 V) in any CMOS processes.

BIOGRAPHICAL SKETCH

Wooram Lee received his B.Sc. and M.S. degrees in electrical engineering from the Korea Advanced Institute of Science and Technology (KAIST) in 2001 and 2003, respectively, and is currently working towards his Ph.D degree at Cornell University. He has held a summer internship at the IBM T. J. Watson Research Center, NY, where he worked on a millimeter-wave frequency multiplier in a 90 nm SiGe process. Before joining Cornell, he was a research engineer at the Electronics and Telecommunications Research Institute (ETRI), Korea, where he worked on optical transceivers and links from 2003 to 2007. His research interests include high performance RF IC design exploiting nonlinear electronics for low noise amplification and oscillation.

Mr. Lee received the IEEE Solid-State Circuits Predoctoral Fellowship for 2010-2011 and the Samsung Graduate Fellowship for 2007-2012. He was a recipient of the Best Paper Award of the IEEE Radar Conference in 2009 and the IEEE Workshop on Passive Microwave Circuits in 2010, and the Silver Medal at the National Physics Competition in 1996

To my Wife and my Mother

for their endless love, patience and support

and to my Son

who has brightened up my life

ACKNOWLEDGEMENTS

As my five-year-long journey on the road to my PhD is nearing the end and I look back time at Cornell, I realize how blessed I am to have experienced such a great environment and such wonderful people. Ithaca has shown me in different form of natural beauty season by season, and Cornell has provided everything that I have needed for my studies. However, the greatest blessing that I have here is that I have been able to interact with so many nice and bright individuals. At times, they have challenged me and thereby helped me to take one step further in my career, and at other times they have warmly encouraged me to stand up when it felt like I had hit bottom.

I would like to thank Prof. Ehsan Afshari, my great teacher and role model. His endless pursuit of creativity and excellence as well as his broad understanding of seemingly everything from pure science to engineering have set a standard for me to reach in my life. In addition, he has always been supportive and patient without losing his high expectations of my academic capacity. Without his valuable inspiration and guidance, this thesis would not have been possible.

I would like to show my deep gratitude to Prof. Alyssa Apsel. I learned every fundamental of analog circuits from her classes, which provided me with a solid background for this thesis. Her technical feedback on my research was essential to completing this thesis. She has been a friendly and warm advisor with a great smile that I will never forget. It is also a great honor for me to have had Prof. Clifford Pollock and Prof. Alexander Gaeta on my committee. They helped me pursue interesting research that lies at the intersection of optics and electronics. Their deep insight inspired me to carry my research beyond electronics.

I would like to thank my friends at the UNIC, with whom I have spent most

TABLE OF CONTENTS

LIST OF TABLES

LIST OF FIGURES

CHAPTER 1

INTRODUCTION

1.1 Motivation

Ever since the first transistor was invented at Bell Laboratories in 1947, transistors have become the basis of integrated circuits design. As Moore's law predicted, transistor scaling in silicon has continued unabated for more than half a century, and has resulted in significant improvement in speed, efficiency, and integration level. In 2011, for instance, Intel announced its 22 nm technology with a 3-D transistor structure [1]. This 22-nm-process-based CPU was expected to run 4000 times faster and with about 5000 times less energy than Intel's first microprocessor (the 4004), released in 1971. Along with the significant performance improvement, the price per transistor has dropped by a factor of about 5000. Such transistor scaling has led to the rapid growth of diverse computing and communications technologies.

Nevertheless, we still face fundamental performance limits that include noise, power, and frequency in the integrated circuits. First, noise remains one of the key challenges in many cutting-edge applications. For example, Fig. 1.1 shows how noise degrades the system performance in an RF-receiver front end. In this system, the total noise generated from the entire receiver chain, mostly caused by a low noise amplifier at the first stage, determines sensitivity. Shannon's theorem in eq. (1.1) states that the minimum received signal power (sensitivity) is determined by receiver noise power for a given bandwidth to achieve
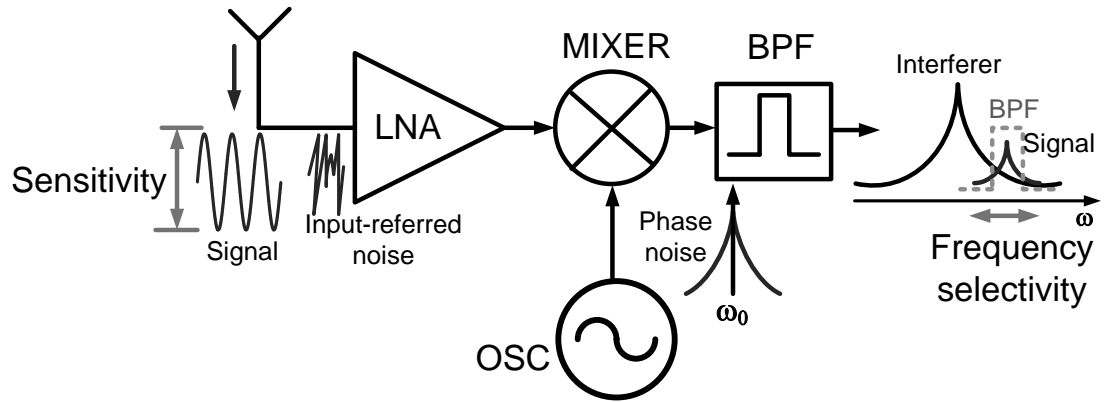
Figure 1.1: Noise of an RF frontend system consisting of a LNA, a mixer, and an oscillator.
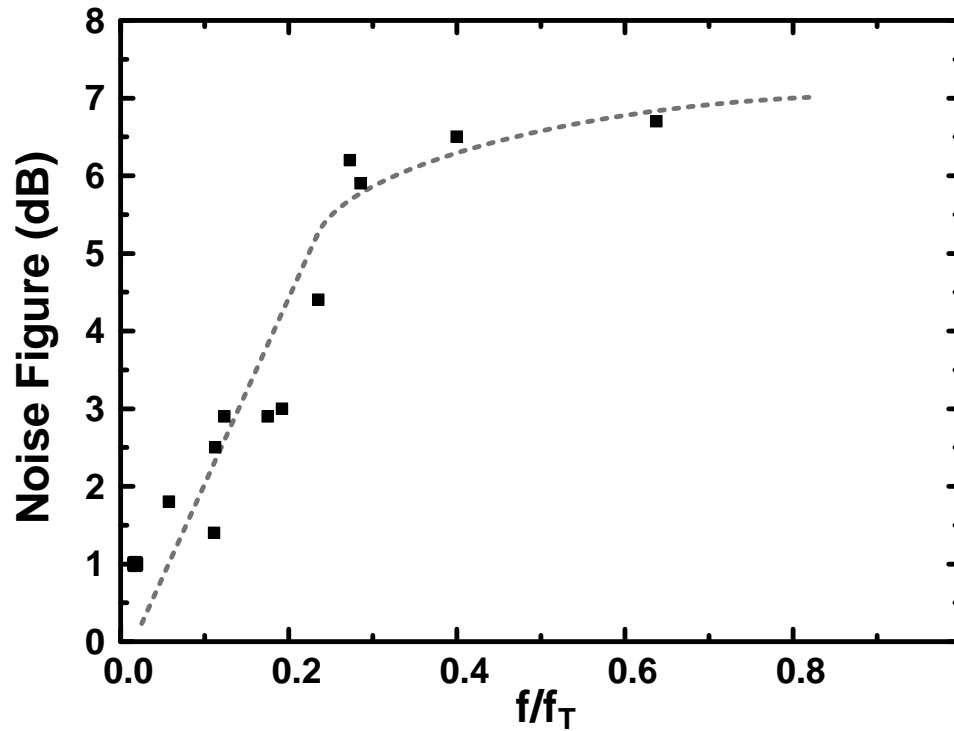
Figure 1.2: Recently-published CMOS LNA performance.

a required channel capacity [3].

$$C = B \cdot \log_2(1 + \frac{S}{N})$$ (1.1)

where C is the channel capacity, B is the bandwidth of the channel, S is total received signal power over bandwidth, and N is total noise power over bandwidth. Here, the receiver noise can be represented by input-referred noise defined as the total output noise divided by the entire signal gain [2].

Still, it is very challenging to improve noise performance in a CMOS process due to excess transistor noise (e.g., channel noise and flicker noise) as well as high loss of passive elements. Fig. 1.2 reports recently-published CMOS LNA performance. As operation frequency approaches transistor cut-off frequency f_T, the noise figure becomes more degraded due to higher loss of passive elements, mainly caused by skin effect and substrate coupling, along with reduced transistor gain. Therefore, this noise limit becomes more critical at higher frequencies.

On the other hand, the phase noise of an oscillator makes a "skirt" around its ideal output signal, represented as a delta function in the frequency domain, as shown in Fig. 1.1. An adjacent interferer mixed with the "skirt" of the LO can fall on a weak IF signal from the desired channel. In other words, phase noise determines frequency selectivity, the minimum frequency spacing with adjacent channels in an RF frontend system. Phase noise $L(\Delta\omega)$ can be predicted from the semi-empirical model, also known as the Lesson-Culter phase noise model [4,5], as follows,

$$L(\Delta\omega) = 10 \cdot \log\left[\frac{2FkT}{P_s} \cdot [1 + (\frac{\omega_0}{2Q\Delta\omega})^2](1 + \frac{\Delta\omega_{1/f^3}}{|\Delta\omega|})\right],$$ (1.2)

3
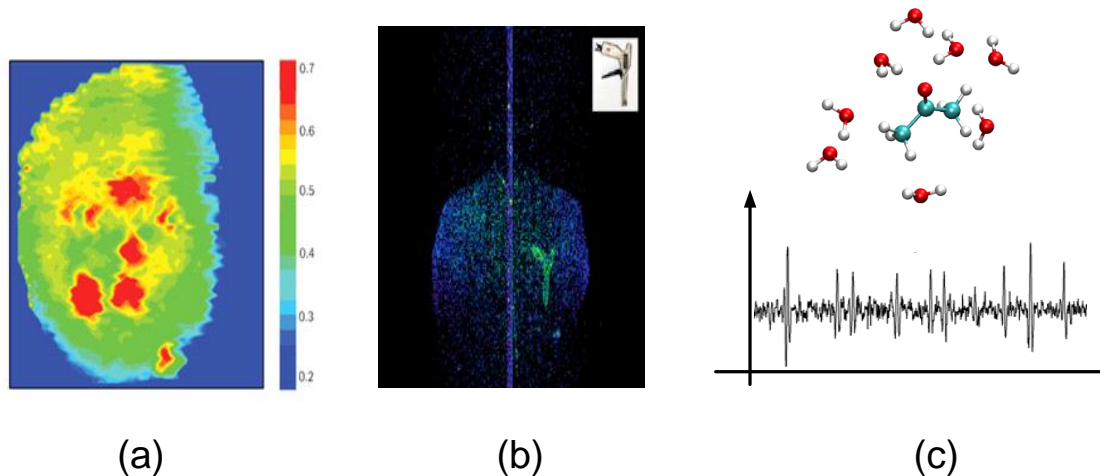
Figure 1.3: Sub-millimeter and THz signal source application for (a) skin tumor detection (red), (b) airport security, and (c) molecular spectroscopy.

where F is a device's excess noise factor, k is Boltzmann's constant, T is absolute temperature, P_s is the average power dissipated in the tank, Q is the effective quality factor including all loadings, ω_0 is oscillation frequency, and $\Delta\omega$ is offset from the carrier. Equation (1.2) indicates that the phase noise is a strong function of quality factor Q and excess noise factor F. However, both parameters Q and F do not have much room to improve further in a CMOS process. For instance, the excess noise factor increases even more due to hot electrons and the velocity saturation effects in short-channel devices. In addition, scaling down the supply voltage, which comes with transistor scaling, limits the maximum P_s, thereby making improvement more difficult.

Next, generating high-power signals in sub-millimeter frequencies for silicon remains challenging due to insufficient transistor gain and breakdowns along with lossy passive components. As shown in Fig. 1.3, high-power signal generation in sub-millimeter frequencies is essential for many security and med-

ical applications, including detection of concealed weapons and bio/molecular spectroscopy for drug detection and breath analysis for disease diagnosis. For security and medical applications, sub-millimeter frequency has advantages over X-rays because it provides excellent penetration properties and high resolution with minimal health risks due to its non-ionizing characteristics. Moreover, due to the the wealth of molecular resonances in this band, sub-millimeter and THz radar signal sources have led to new radar science applications for detecting and sensing particles, chemical compositions, molecular structures, bio-particles, and bacteria detection as well as aiding in characterizing the cold (10-20K) dust found in the interstellar medium in the Milky Way.

Fig. 1.4 shows the maximum power that can be generated from an electrical or an optical source versus frequency, based on recent publications [6]. Electronic technology using frequency multipliers, resonant tunneling diodes, and Impatts and Gunn oscillators, is progressing upward, while optical technology using quantum cascade lasers is progressing downward from higher frequencies. As shown in Fig. 1.4, it is clear that the maximum generation power of electronic technology is degraded for higher frequencies, which is due to parasitic circuit elements like series resistance and shunt capacitance as well as electron transport limited by transit and scattering time. For optical approaches, as the generation frequency becomes lower, the generation power also decreases due to the parametric relationship. A significant gap exists between these two approaches around THz frequencies; thus, a new solution is required to bridge the gap.

In addition, transistor scaling in silicon has almost reached the end of its physical dimensions in approaching atomic and quantum mechanical bound-
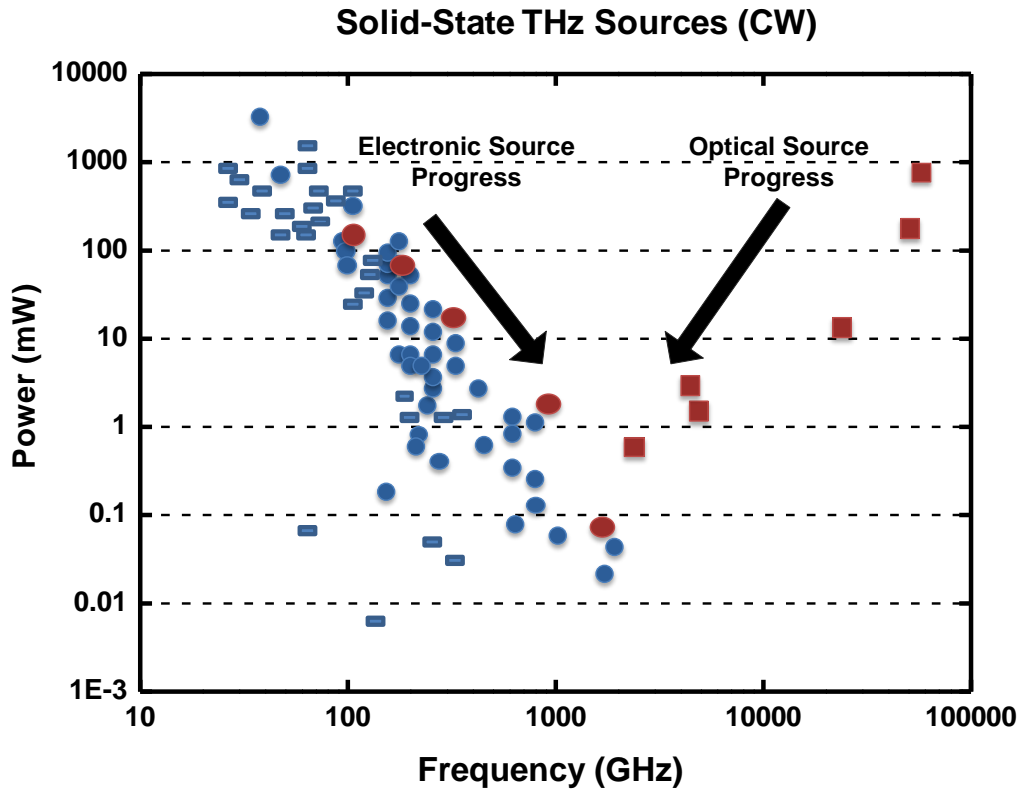
Figure 1.4: Recently-published Solid-State THz Source [6].

aries, and the fabrication techniques are also hitting their physical and economic limits. Reducing gate dielectric thickness and channel length increases tunneling and leakage current, and the small device size requires lithography-based fabrication techniques that can provide a resolution below the wavelength of light. Along with device scaling, scaling down the power supply causes several critical issues in conventional analog circuit design [7]
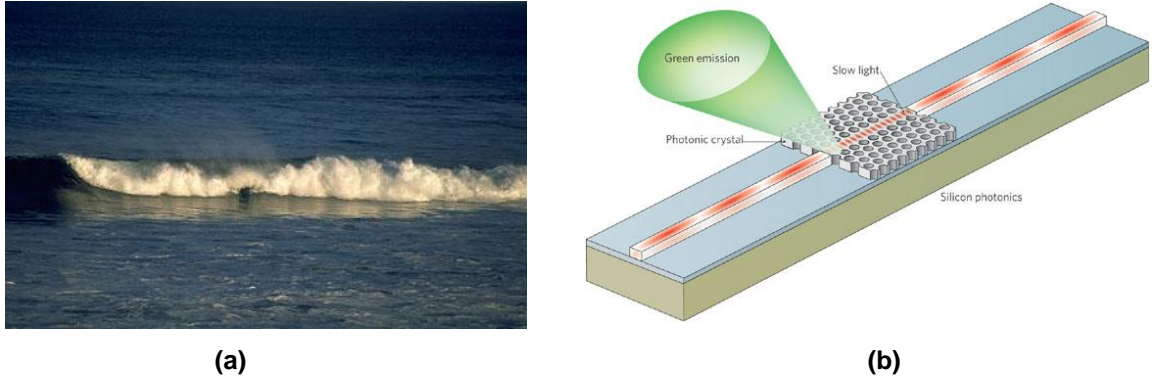
Figure 1.5: Examples of nonlinear phenomena in (a) solitary wave in the sea and (b) green light generation [10].

1.2 Proposed Solution

To overcome these limits, we propose a new circuit design methodology inspired by wave propagation in a nonlinear medium. In conventional CMOS circuit designs, transistors, which convert energy from DC to RF, are mainly used for signal amplification, generation, and processing. Such an energy conversion process in transistors is restricted by excess noise and parasitics, as discussed in the previous section. Instead of relying on transistors, in the proposed methodology, energy transfer among different frequencies through nonlinear wave interaction will be exploited.

We can find out several examples of nonlinear phenomena in different fields with a similar concept to the proposed methods. Fig. 1.5(a) shows solitary wave generation in the sea. Because nonlinearity compensates the dispersion that a sea wave tends to spread out due to gravity and surface tension, the sea wave can propagate like a particle with a well-defined shape. This phenomenon was initially discovered in 1834 by Scott Russell, and is know as "solitary wave"

7

or "soliton" [8], a discovery that has been significant in physics, electronics, biology, and fiber optics. For instance, using a nonlinear electrical medium described in Fig. 1.6, an electrical soliton was demonstrated to generate a 2.5-ps pulse in a standard CMOS process beyond the cut-off frequency of transistors [9].

The second example is a green light generation from the injection of red light in silicon exploiting the third order harmonic generation enhanced by slow-light pulses in a photonic crystal waveguide, as shown in Fig. 1.5(b) [10]. Because an optical gain medium is rarely available in silicon at the wavelength of green light; thus, a nonlinear optical material is exploited to move energy at the wavelength of input red light into that of green light. Here, a nonlinear optical material means that the response of a material system, represented as induced polarization $\tilde{P}(t)$, depends on the strength of an applied optical field strength $\tilde{E}(t)$ in a nonlinear manner. Hence, the optical response can be expressed as a power series of an applied electric field given by

$$\tilde{P}(t) = \epsilon_0[\chi^{(1)}\tilde{E}(t) + \chi^{(2)}\tilde{E}^2(t) + \chi^{(3)}\tilde{E}^3(t) + ...] \tag{1.3}$$

The third order harmonic generation mainly results from the $\tilde{P}^{(3)}(t) = \epsilon_0\chi^{(3)}\tilde{E}^3(t)$ term in eqn. (1.3). In addition to harmonic generation, in nonlinear optics, parametric processes are also studied such as sum-and-difference frequency generation and optical parametric amplification and oscillation, when lights at different wavelengths propagate together in a nonlinear optical material. These optical nonlinear phenomena have provided important insights for the proposed research in extending the concepts to CMOS circuit design.

As a platform of our circuit implementation of various nonlinear processes in the proposed research, a nonlinear propagation medium has been designed
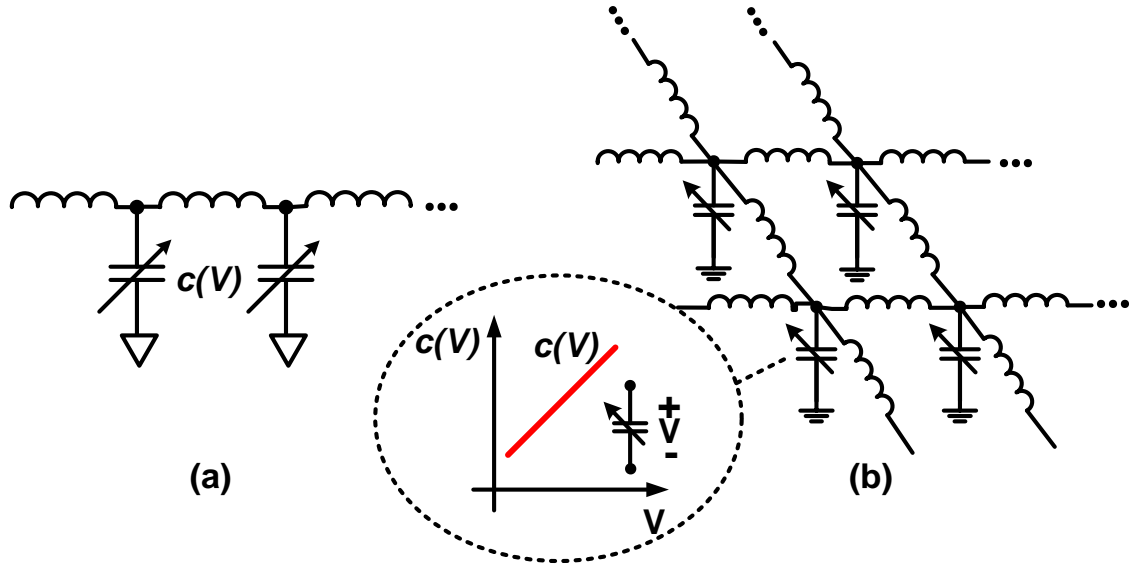
Figure 1.6: 1-D and 2-D nonlinear electrical medium consisting of voltage-dependent capacitors and inductors.

in electrical circuits as shown in Fig. 1.6. This medium is formed with voltage-dependent capacitors (varactors) along with inductors in one-dimensional or two-dimensional space. An applied voltage across a varactor generates electric current at new frequencies in a nonlinear manner, as an applied electric field induces polarization at new frequencies in a nonlinear optical material.

Lattices can be characterized in terms of the characteristic impedance Z_0 and the propagation constant β. For instance, in a one-dimensional low-pass transmission line as shown in Fig. 1.6(a), the characteristic impedance and propagation constant are given by $Z_0 = \sqrt{L/C}$ and $\beta = \sqrt{LC}$, respectively. By defining these two parameters at different spaces and conditions, electrical nonlinear medium can be easily engineered to implement the desired propagation and reflection properties. For instance, we have built a new electrical nonlinear medium simply by using a differential structure with additional capacitors to

9

achieve phase-matching, in which waves at different frequencies should propagate at the same velocities for the maximum nonlinear process. This structure enables perfect phase matching in the presence of dispersion by increasing propagation velocity at higher frequencies, whereas perfect phase matching in optics is still challenging.

As a nonlinear source in the proposed medium, voltage-dependent capacitors can be implemented with accumulation-mode MOS varactors or Schottky diodes fabricated in a standard CMOS process. Fig. 1.7 shows a model of an accumulation-mode NMOS varactor along with its physical structure. The varactor capacitance is a series combination of C_{ox} and C_{var}, where C_{ox} is oxide capacitance and C_{var} is depletion capacitance under the gate oxide that changes with the bias voltage. In a positive bias voltage, electrons are accumulated under the gate for the maximum C_{var}, while a negative bias enlarges a depletion region and decreases C_{var}. Because the variable capacitance is based on physical movement of electrons, MOS varactors can operate at very high frequencies. For instance, in our recent work, we demonstrated a dynamic cut-off frequency of around 870 GHz for a 480-GHz frequency doubler design in a standard 65-nm CMOS process [11].

Based on a nonlinear electrical medium with voltage-dependent capacitors, this study focuses primarily on different nonlinear phenomena including parametric oscillation and amplification, noise squeezing, and harmonic generation to design high-performance integrated circuits in the following areas:

I. A Passive CMOS Frequency Divider Using a Distributed Parametric Resonator

II. A Low Noise Parametric Resonant Amplifier with Noise Squeezing
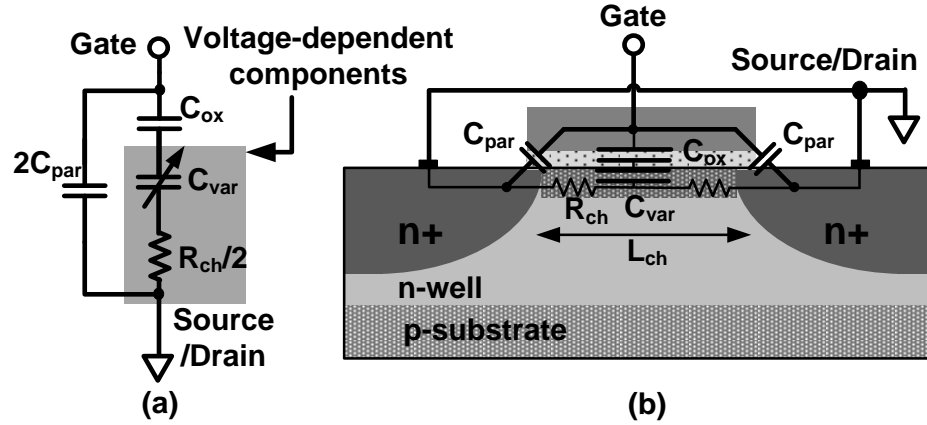
Figure 1.7: (a) a simple model of an accumulation-mode NMOS varactor and (b) its physical structure.

III. A Nonlinear Lattice for High-amplitude Picosecond Pulse Generation in CMOS.

These research contributions prove that the proposed approach not only results in superior noise and frequency performance, but also adds new dimensions to the circuit design such as phase-sensitive gain and noise squeezing. We describe our contributions regarding each of these topics in the following sections.

1.3   Organization

In Chapter 2, we provide an overview of the fundamentals of parametric amplification in different physical systems. Then, we extend the concept to traveling wave parametric amplification in a nonlinear transmission line, and theoretically analyze the principle starting from Kirchhoff's law to nonlinear wave equations and coupled-mode equations. We also discuss the performance limits of parametric amplification due to dispersion and loss effect in a standard

CMOS technology. To compensate for the dispersion, we propose a new method based on a differential nonlinear transmission line with common-mode capacitors.

In Chapter 3, we introduce the concept of parametric oscillation to design the first passive 20 GHz CMOS frequency divider, which consists of two parallel nonlinear transmission lines using MOS-varactors, forming a reflective distributed resonator. In this circuit, the oscillation at half the input frequency is sustained by energy injection from an input signal through parametric amplification. Its operational principle is the electronic analogue to that of the optical parametric oscillator. The distributed structure enables a stable start-up condition and a broad range of frequency tunability. Moreover, the reflective resonator minimizes the number of components and forms a standing wave, which suppresses the pump signal at the output while maintaining a large output signal amplitude. In addition to zero static power consumption, the proposed frequency divider shows better phase noise performance even at high offset frequencies, since it is free of the channel noise from the transistors.

In Chapter 4, we propose a parametric amplifier based on the distributed nonlinear resonator, and develop the theory of classical noise squeezing in the proposed system. The distributed nonlinear resonator operates as a regenerative amplifier by supplying pump amplitude below the oscillation threshold. As a result, the amplifier achieves a high close-loop gain using a less-than-unity open-loop gain. An important property of the proposed amplifier is its phase-sensitive gain, resulting in noise squeezing. One of the quadrature input noise components, e.g., out-of-phase, is suppressed when the input noise consists of two quadrature components: in-phase and out-of-phase relative to the pump

signal. This noise squeezing reduces the amplifier output noise by almost 3 dB compared with the phase-insensitive amplifier with the same gain. In other words, while a conventional amplifier increases the input noise of both quadratures, the noise-squeezing amplifier increases the noise of one quadrature and, at the same time, decreases the other one. To the best of our knowledge, our work is the first demonstration of noise squeezing for a low-noise amplifier in a CMOS process. In the measurement, we demonstrate that sensitivity for an in-phase component is improved by 2.5 dB after noise squeezing with a gain of 21 dB at 8.75 GHz in a standard 0.13-μm CMOS process, nearly approaching the ideal noise limit. For the quadrature, the sensitivity is degraded by 6.4 dB, with a gain of 12 dB, respectively.

In Chapter 5, we demonstrate high-amplitude picosecond generation method that goes beyond the cut-off frequency of transistors using a nonlinear lattice. When two waves collide orthogonally in the nonlinear lattice, they combine in a nonlinear fashion: The amplitude of the outgoing wave is greater than the sum of the incoming waves with much higher frequency components. As a result, we have implemented an integrated nonlinear lattice in a standard 0.13-μm CMOS process to demonstrate 2.7-V_{pp}, 6.3-ps pulses from a 22-GHz sinusoidal input. To the best of our knowledge, regarding the high-amplitude pulses (>1 V), this work shows the sharpest pulse in a CMOS process. We also show that the proposed structure exploits spatial power combining, higher cut-off frequency, and two-dimensional nonlinear interference to significantly enhance both the amplitude and pulse width, compared with results using a one-dimensional nonlinear transmission line.

BIBLIOGRAPHY

[1] Intel 22 nm Technology. [Online]. Available: http://www.intel.com/content/www/us/en/silicon-innovations/intel-22nm-technology.html.

[2] T.H. Lee, *The Design of CMOS Radio-Frequency Integrated Circuits*, Cambridge, New York, NY, 2004, p.348.

[3] C.E. Shannon, "A Mathematical Theory of Communication," *The Bell System Technical Journal*, vol. 27, pp. 379-423, July. 1948.

[4] L.S. Culter and C.L. Searle, "Some asepcts of the theory and measurement of frequency fluctuations in frequency standards," *Proc. IRE*, vol. 54, pp. 136-154, Feb 1966.

[5] D.B. Leeson,"A Simple Model of Feedback Oscillator Noises Spectrum," *Proc. IRE*, vol. 54, pp. 329-330, Feb 1966.

[6] T.W. Crowe, W.L. Bishop, D.W. Porterfield, J.L Hesler, and R.M. Weikle, "Opening the Terahertz Window With Integrated Diode Circuits," *IEEE J. Solid-Stat Circuits*, vol. 40, no. 10, pp. 2104-2109, Oct. 2005.

[7] N.Z. Haron and S. Hamdioui, "Why is CMOS scaling coming to an END?", in Proc. International Design and Test Workshop, Dec. 2008.

[8] J.S. Russell,"Report on Waves," Report of the fourteenth meeting of the British Association for the Advancement of Science, pp. 311-390, Plates XLVII-LVII, York, Sept. 1844.

[9] E. Afshari and A. Hajimiri, "Nonlinear Transmission Lines for Pulse Shaping in Silicon," *IEEE J. Solid-Stat Circuits*, vol. 40, no. 3, pp. 744-752, Mar. 2005.

[10] T. Baba, "Nonlinear optics: Sliicon gets the green light," *Nature Photonics*, vol. 3, pp. 190-192, 2009 (doi:10.1038/nphoton.2009.39).

[11] R. Han and E. Afshari, "A Broadband 480-GHz Passive Frequency Doubler in 65-nm Bulk CMOS with 0.23 mW Output Power," in Proc. IEEE RFIC Symp., Jun. 2012.

CHAPTER 2

FUNDAMENTALS OF PARAMETRIC AMPLIFICATION

Parametric amplification has been actively studied in various fields such as optics, quantum mechanics, plasma physics, and electronics [1–4]. Parametric amplification is based on nonlinear interaction between signal and pump, which results in signal gain through energy transfer. In the 1960s, considerable attention had been paid to electrical parametric amplification due to its low noise performance before the transistor technology dominated the integrated circuit design [5]. Recently, several interesting works have revisited parametric amplification for CMOS technology. Discrete-time parametric amplification has been implemented with a MOS varactor to achieve low power and low noise performance for low sampling frequencies [6–8]. The parametric process was also exploited for frequency conversion of a continuous signal [9–11].

In this chapter, we mainly discuss parametric amplification in a nonlinear transmission line in a standard CMOS process. This chapter is organized as follows. Section 2.1 is an overview of parametric amplification in an LC resonator and a nonlinear transmission line. Section 2.2 theoretically analyzes traveling wave parametric amplification and discusses the dispersion effect, phase matching techniques, and the pump loss effect.

2.1 Overview

Parametric amplification can be explained with a swing as shown in Fig. 2.1. There are two ways to swing higher. The first method is to push the swing with an external force at the resonance frequency of the swing. Alternatively,
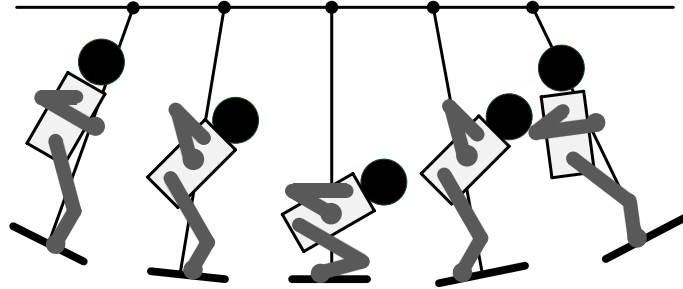
Figure 2.1: A swing as an example of degenerate parametric amplification. The center of mass moves with an appropriate phase at twice the swing frequency to swing higher.
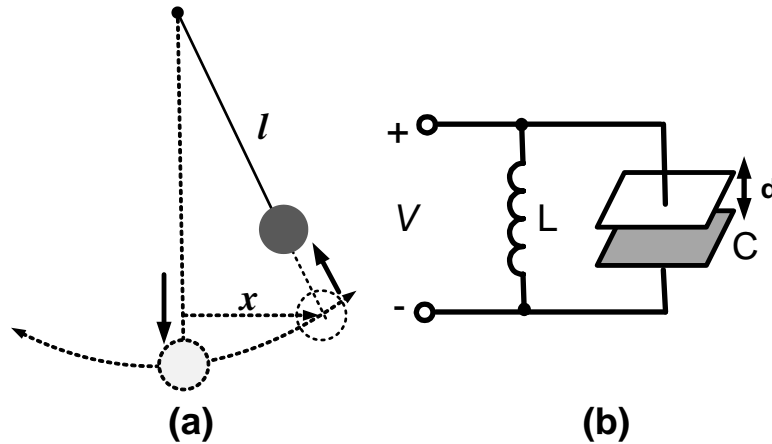
Figure 2.2: (a) Pendulum model of a swing and (b) an LC resonator with variable capacitor.

the person on the swing can move up and down at twice the swing frequency. In this method, the relative phase of the body movement and swing is critical: The person should lower the center of mass on the downswing and raise it on the upswing. This example shows that we can pump energy into a system to amplify a signal by changing one of the system parameters (e.g., effective length of the swing).

When the pump frequency is exactly twice the signal frequency, this pro-

cess is called *degenerate parametric amplification*. The swing can be modeled as a simple pendulum as shown in Fig. 2.2(a). Under the assumption of small displacement x, the governing differential equation of the pendulum can be written as

$$\frac{d^2x(t)}{dt^2} = -\frac{g}{l}x(t) = -\omega_{swing}^2 x(t), \tag{2.1}$$

where x is the swing amplitude, g is the acceleration of gravity, l is the length of the pendulum, and ω_{swing} is the natural oscillation frequency of the swing. A similar harmonic oscillation occurs in an LC resonator as shown in Fig. 2.2(b). In this case, the governing equation is

$$\frac{d^2V(t)}{dt^2} = -\frac{1}{LC}V(t) = -\omega_{LC}^2 V(t), \tag{2.2}$$

where L and C are the inductance and the capacitance of the resonator, ω_{LC} is the resonance frequency, and V is the voltage across the resonator. Equations (2.1) and (2.2) show an intriguing duality between the pendulum and the LC resonator by switching x with V and l with C. This analogue implies that the voltage V can be amplified by changing the capacitance C (e.g., by changing the distance d between two capacitor plates) at twice the resonance frequency with an appropriate phase.

Figure 2.3 shows the parametric amplification inside an LC resonator. Assume that initially the circuit is oscillating at its natural frequency. When the voltage is maximum, we decreases the capacitance by increasing d. Due to charge conversation, this results in increasing the voltage. It is noteworthy that pulling the two capacitor plates requires pumping energy into the system. When the voltage is zero, we return the capacitor plates to their original position. Since the voltage and charge of the capacitor are zero, no energy is required in this phase. By repeating the same process, we can keep increasing the voltage
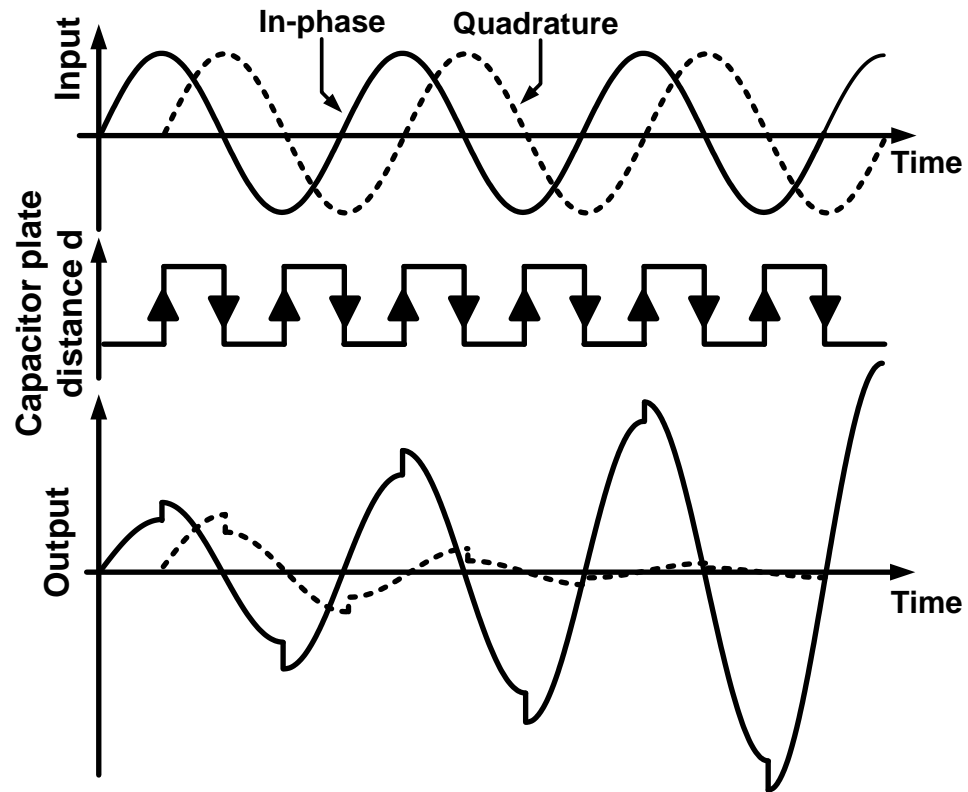
Figure 2.3: Voltage amplification in an LC resonator using a degenerate parametric process where the pump at twice the resonance frequency adds energy to or extracts energy from the signal.

magnitude by transferring the energy from pump to the signal. As illustrated in Fig. 2.3, the frequency of the capacitance change is twice the signal frequency. More importantly, the phase relation between the pump and signal is vital for amplification. If the signal phase is shifted by 90° (shown in dotted line in Fig. 2.3), the oscillation is damped out and the signal energy is transferred to the pump.
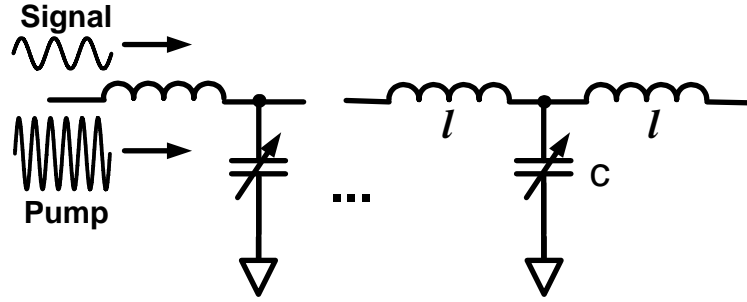
Figure 2.4: Parametric amplification in an LC transmission line with var-
actors.

2.2 Traveling-Wave Parametric Amplification

The amplification process in an LC resonator can be extended to an LC trans-
mission line, as shown in Fig. 2.4. The wave equation of an LC transmission
line using phasor notation is

$$\frac{d^2 V(z)}{dz^2} = -\omega^2 LC V(z) = -\beta^2 V(z),$$ (2.3)

where $V(z)$ is the voltage on the line with respect to the ground, L and C are unit
length inductance and capacitance, and β is the propagation constant. We can
see an interesting duality between (2.3) and (2.2) by switching β with ω_{LC} and
length z with time t. Therefore, without rigorous derivation, it is straightforward
to predict amplification over distance (instead of time) along the transmission
line. To do so, we need to periodically perturb the propagation constant β (in-
stead of the resonance frequency) at different points on the line (instead of at
different times). In other words, Figure 2.3 also explains traveling-wave para-
metric amplification by replacing time with distance on the horizontal axis. To
change β periodically along the transmission line, we use voltage-dependent ca-
pacitors and apply a large amplitude pump at twice the signal frequency, which
co-propagates with the signal. Depending on an initial phase between the pump
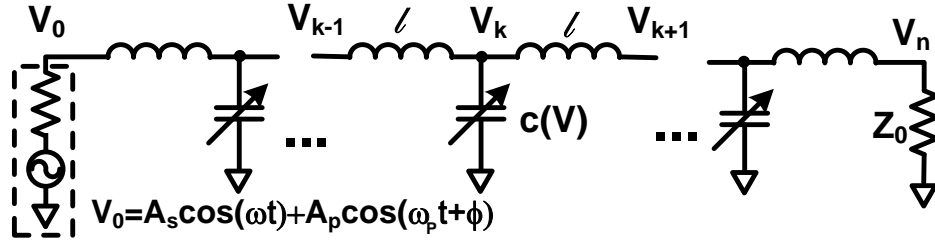
Figure 2.5: A uniform nonlinear transmission line for parametric amplification

and the signal, the parametric process can amplify or attenuate the signal.

2.2.1 Theoretical Analysis

Assume a uniform artificial transmission line consisting of inductors and voltage-dependent (and hence nonlinear) capacitors shown in Fig. 2.5. By applying KCL at node k, whose voltage with respect to ground is V_k, and applying KVL across the two inductors connected to this node, one can easily show the voltages of adjacent nodes on this transmission line are related via:

$$l\frac{d}{dt}\left[c(V_k)\frac{dV_k}{dt}\right] = V_{k+1} - 2V_k + V_{k-1}. \tag{2.4}$$

The nonlinear capacitor is approximated with a first-order function:

$$c(V) = c_0(1 + bV) \tag{2.5}$$

where c_0 is the capacitance at zero bias and b is the C/V slope. This first-order approximation is validated around zero-bias voltage in a conventional accumulation-mode NMOS varactor as shown in Fig. 2.6.

For now, we neglect the loss of the transmission line. Equation (2.4) can
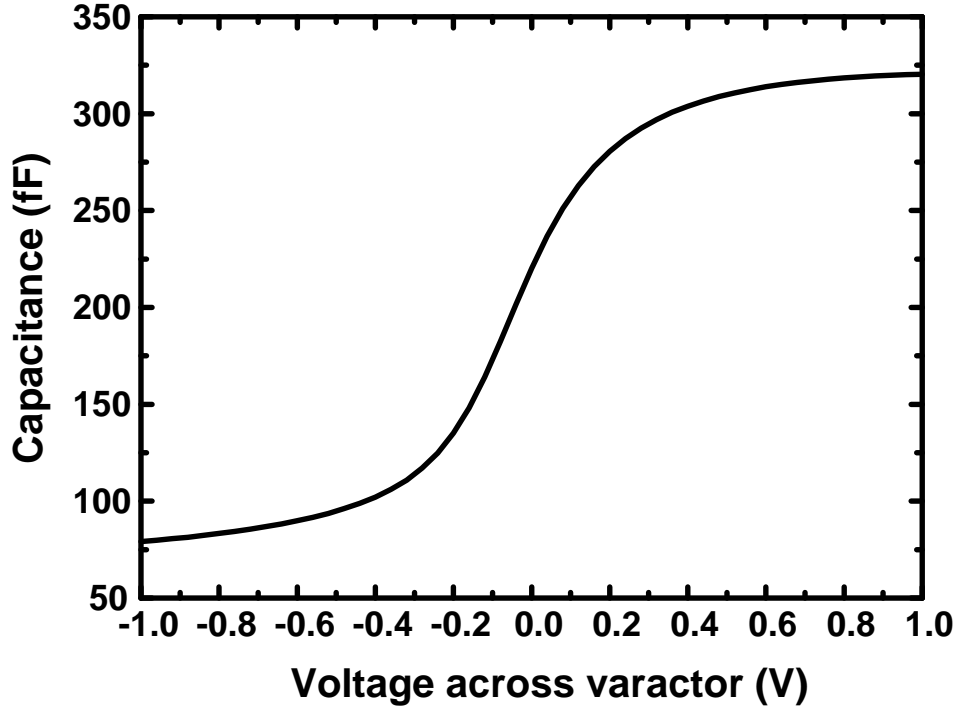
Figure 2.6: Simulated varactor capacitance versus bias voltage in a 0.13 μm process.

be written as a partial differential equation (2.6) by approximating the node voltage as a continuous variable over distance: $V_k = V(kh) \simeq V(x)$. Here, h is the spacing between two adjacent nodes and k is the section number. We also introduce a unit length inductance, $L = l/h$, and a unit length capacitance, $C = c/h$. For simplicity, we assume that the dispersion effect caused by discreetness is negligible, due to a small h compared to the signal wavelength.

$$
\begin{aligned}
\frac{V_{k+1} - 2V_k + V_{k-1}}{h^2} &= \left[\frac{(V_{k+1} - V_k)}{h} - \frac{(V_k - V_{k-1})}{h} \right] \frac{1}{h} \\
&\simeq \frac{\partial^2 V}{\partial x^2} = L \frac{\partial}{\partial t} \left[C(V) \frac{\partial V}{\partial t} \right]
\end{aligned}
\tag{2.6}
$$

Next, pump and signal are applied to the left end of the transmission line,

21

and the pump frequency ($\omega_p = 2\omega$) is set to be twice the signal frequency (ω).

By inserting $V = V_s + V_p$ and (2.5) into (2.6), equation (2.6) becomes:

$$\frac{\partial^2(V_s + V_p)}{\partial x^2} = LC_0\frac{\partial^2(V_s + V_p)}{\partial t^2} + LC_0b\frac{\partial^2(V_s \cdot V_p)}{\partial t^2} + \frac{LC_0b}{2}\left[\frac{\partial^2(V_s \cdot V_s)}{\partial t^2} + \frac{\partial^2(V_p \cdot V_p)}{\partial t^2}\right] \tag{2.7}$$

where V_s and V_p are signal and pump voltages, respectively. The first term on the right corresponds to the linear wave propagation, and the second term represents the nonlinear coupling between pump and signal, which results in the parametric amplification. The third term on the right corresponds to the second-order harmonic generation (SHG) for signal and pump. We assume the signal amplitude is so small that the SHG for the signal is negligible, and that the SHG for the pump is sufficiently suppressed since the cut-off frequency of the transmission line is set to be lower than the second harmonic of the pump frequency. Under these assumptions, we simplify equation (2.7) as:

$$\frac{\partial^2(V_s + V_p)}{\partial x^2} = LC_0\frac{\partial^2(V_s + V_p)}{\partial t^2} + LC_0b\frac{\partial^2(V_s \cdot V_p)}{\partial t^2}. \tag{2.8}$$

After equation (2.8) is rearranged at a signal frequency and transmission line loss α_s is included, we can obtain

$$\frac{\partial^2 V_s}{\partial x^2} = LC_0\frac{\partial^2 V_s}{\partial t^2} + LC_0b\frac{\partial^2(V_s \cdot V_p)}{\partial t^2} + 2\sqrt{LC_0}\alpha_s\frac{\partial V_s}{\partial t} \tag{2.9}$$

where

$$\alpha_s = \frac{1}{2}\left(GZ_0 + \frac{R}{Z_0}\right) \tag{2.10}$$

and L, C, G, and R are unit length inductance, capacitance, parasitic conductance, and parasitic resistance, respectively. Z_0 is the characteristic impedance defined by $\sqrt{L/C_0}$. α_s is the transmission line loss for the signal frequency.

From coupled-mode theory [3, 12, 13], the signal can be written as:

$$V_s(x, t) = V_s(x)e^{j\omega t} + V_s^*(x)e^{-j\omega t} \tag{2.11}$$

$$V_s(0, t) = A_s \cos(\omega t + \phi) \tag{2.12}$$

where $V_s(x) = A(x)e^{-j\beta x}$, $V_s^*(x) = A^*(x)e^{j\beta x}$, β is the signal propagation constant, and ϕ is the initial phase difference between signal and pump at $x=0$. Here, "*" denotes the complex conjugate. $A(x)$ and $A^*(x)$ are slowly varying functions over x which means $\partial A/\partial x \ll \beta A$.

Assume that the pump is a sinusoidal function at a frequency of $\omega_p = 2\omega$. Then, the pump can be written as:

$$V_p(x, t) = A_p(x) \cos(\omega_p t - \beta_p x) \tag{2.13}$$

$$= \frac{1}{2}A_p(x)\left[e^{j(\omega_p t - \beta_p x)} + e^{-j(\omega_p t - \beta_p x)}\right] \tag{2.14}$$

where $A_p(x)$ is the amplitude of the pump, which is a slowly varying function over x, and β_p is the pump propagation constant.

By substituting (2.11) and (2.14) into (2.9) and by approximating β as $\beta \simeq \omega \sqrt{LC_0}$ (small dispersion assumption) and β_p as $\beta_p = 2\beta - \Delta\beta$ (the dispersion might not be negligible for the pump, which is at twice the input frequency), we derive the active coupled-mode equations for $A(x)$ and $A^*(x)$ as:

$$\frac{\partial A}{\partial x} = -\frac{j\beta b A_p}{4}A^* e^{j\Delta\beta x} - \alpha_s A \tag{2.15}$$

$$\frac{\partial A^*}{\partial x} = \frac{j\beta b A_p^*}{4}A e^{-j\Delta\beta x} - \alpha_s A^* \tag{2.16}$$

For now, A_p is assumed to be constant over x to obtain an analytic solution of (2.15) and (2.16). This assumption means that we neglect the pump loss in the transmission line and the transferred pump energy to the signal frequency.

23

Under this assumption, the general solution for (2.15) and (2.16) is:

$$A = e^{(-\alpha_s + j\Delta\beta/2)x}(A_1 e^{sx} + A_2 e^{-sx}) \tag{2.17}$$

where

$$s = \sqrt{\left(\frac{\beta b A_p}{4}\right)^2 - \left(\frac{\Delta\beta}{2}\right)^2} \tag{2.18}$$

and A_1 and A_2 are constants over x.

By applying the boundary condition of (2.12) to (2.15), the complete solution is obtained as:

$$V_s(x, t) = A_s e^{-\alpha_s x} \left[C_1 \cos(\omega t - \beta x) + S_1 \sin(\omega t - \beta x) \right] \tag{2.19}$$

where

$$C_1(x, \phi) = \cosh(s_0 x) \cos\phi - \sinh(s_0 x) \sin\phi \tag{2.20}$$

$$S_1(x, \phi) = \sinh(s_0 x) \cos\phi - \cosh(s_0 x) \sin\phi \tag{2.21}$$

and $s_0 = \beta b A_p / 4$ is the first term on the right side of (2.18). It is noteworthy that in (2.19) we have assumed no dispersion for the pump ($\Delta\beta = 0$). At the end of this section, we will introduce a method to compensate the dispersion for the pump, validating this assumption.

From (2.19), the parametric gain is:

$$G(x) = \frac{|V_s(x)|}{A_s} = e^{-\alpha_s x} \sqrt{\cosh(2s_0 x) - \sinh(2s_0 x) \sin 2\phi} \tag{2.22}$$

For the maximum and minimum gains, the signal is exponentially growing or decaying over x:

$$G(x) = \begin{cases} e^{(s_0 - \alpha_s)x} & \text{for } \phi = -\frac{\pi}{4} \text{ (max.)} \\ e^{-(s_0 + \alpha_s)x} & \text{for } \phi = \frac{\pi}{4} \text{ (min.)} \end{cases} \tag{2.23}$$

24

Eq. (2.22) can be converted into the gain equation for the section number, k, of the discrete transmission line by inserting $L = l/h$, $C_0 = c_0/h$, $G = g/h$, $R = r/h$, and $x = kh$ where h is the spacing between two adjacent LC sections. l, c_0, g, and r are inductance, average varactor capacitance, conductance, and resistance for one LC section, respectively. Using

$$s_0 x = \frac{bA_p}{4} \cdot \omega \sqrt{(\frac{l}{h})(\frac{c_0}{h})} \cdot kh = \frac{bA_p \omega \sqrt{lc_0}}{4} \cdot k \qquad (2.24)$$

$$\alpha_s x = \frac{1}{2}\left(gZ_0 + \frac{r}{Z_0}\right) \cdot k, \qquad (2.25)$$

the parametric gain for the $k-$section nonlinear transmission line is presented by

$$G_k = G(kh) = e^{-\widetilde{\alpha}_s k} \sqrt{\cosh(2\widetilde{s}_0 k) - \sinh(2\widetilde{s}_0 k) \sin 2\phi}, \qquad (2.26)$$

where

$$\widetilde{s}_0 = \frac{bA_p \omega \sqrt{lc_0}}{4} \qquad (2.27)$$

$$\widetilde{\alpha}_s = \frac{1}{2}\left(gZ_0 + \frac{r}{Z_0}\right) \qquad (2.28)$$

Fig. 2.7 is the plot of calculated parametric gain for 20 LC sections based on (2.26) to show the effect of initial phase differences between pump and signal for different nonlinear factors, defined by bA_p. The input and pump frequencies are 10 GHz and 20 GHz, respectively. The cut-off frequency, defined by $\omega_c = 2/\sqrt{lc_0}$, is set to be 25 GHz and the characteristic impedance is 50 Ω. We assume that the quality factor of the transmission line for a signal frequency is 10, which corresponds to $\widetilde{\alpha}_s = 0.04/section$. As the nonlinear factor increases, the gain plot shows a higher amplification and attenuation depending on the phase difference. The phase difference between the maximum and minimum is $\pi/2$, which clearly shows the phase-sensitive gain for quadrature signals.

25
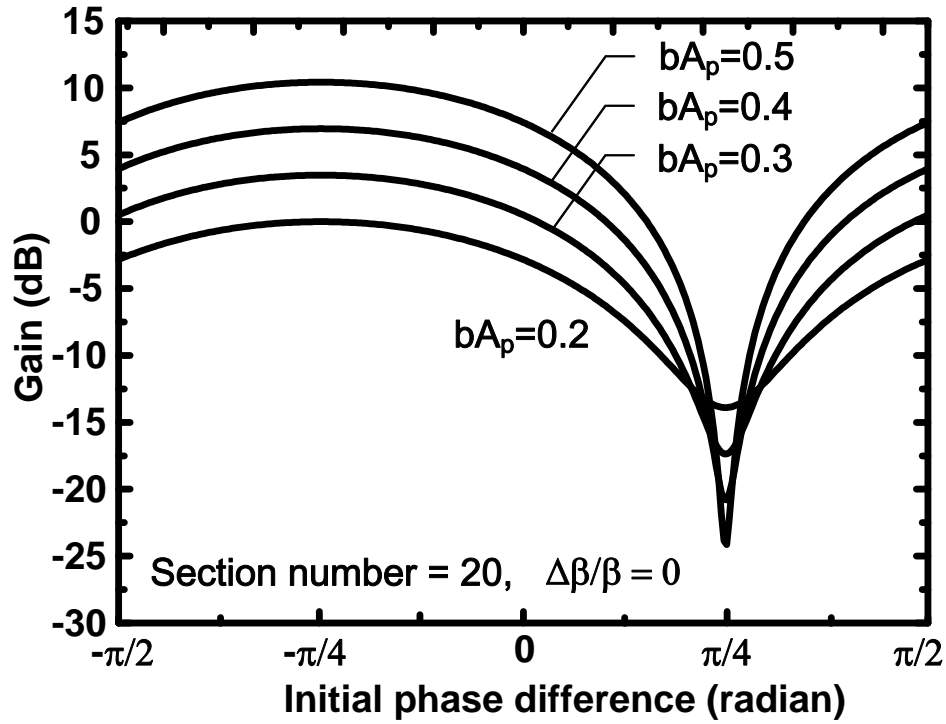
Figure 2.7: Calculated gain versus the initial phase difference between pump and signal for different nonlinearity factors. (l=630 pH, c_0=250 fF, ω=10 GHz)

Note that the exponent, s_0, in (2.23) is proportional to the propagation constant, β, as well as the varactor C/V slope and the pump amplitude. This is because the increase in the propagation constant is equivalent to the increase in the effective transmission line length. However, the increase in the propagation constant also lowers the cut-off frequency and decreases the pump amplitude. Therefore, the propagation constant should be carefully selected.

The parametric amplification on the transmission line can be intuitively explained using the distributed mixing principle illustrated in Fig. 2.8. As shown in this figure, the input signal at ω interacts with the pump at 2ω through the varactor nonlinearity, generating harmonics at 3ω ($= \omega + 2\omega$) and ω ($= 2\omega - \omega$).

(a)

(b)
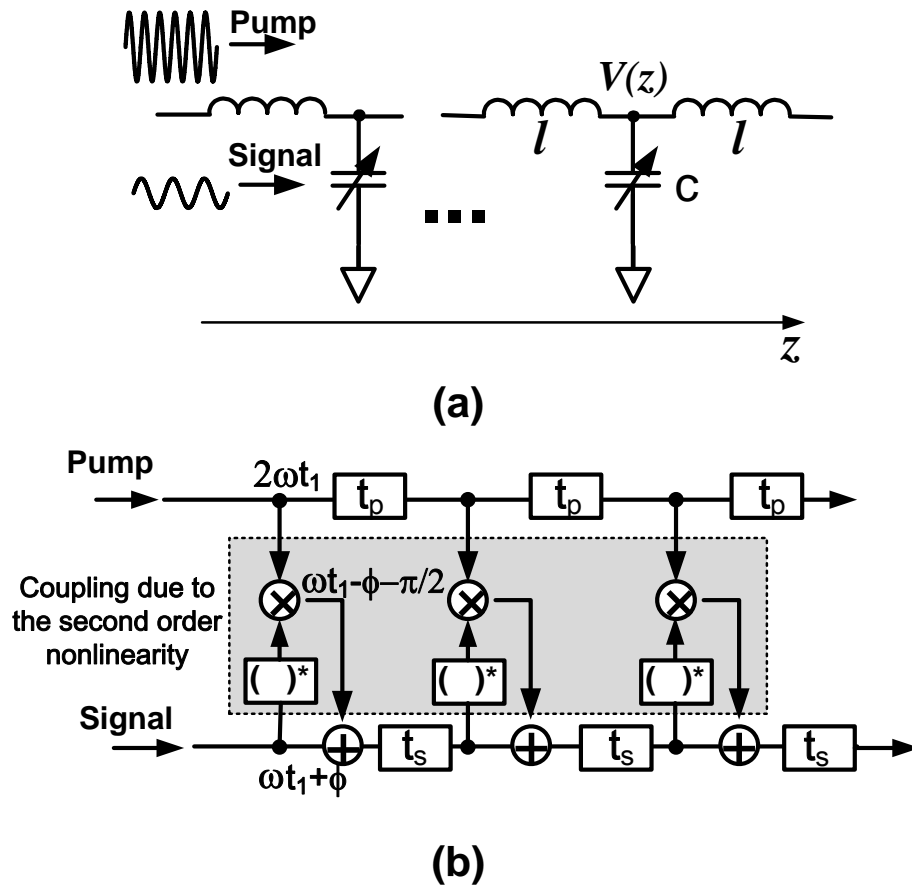
Figure 2.8: An intuitive model to explain the degenerate parametric amplification over a nonlinear transmission line.

The cut-off frequency of the line is selected between 2ω and 3ω so that 3ω and higher-order harmonics are suppressed. The harmonic component at ω has the same frequency as the input, which can be added constructively or destructively to the signal depending on the phase. This means that the energy can be transferred from pump to signal or vice versa. Since this process occurs at every LC section of the line, we get an exponential gain or attenuation as a function of section number in a long transmission line.

2.2.2 Phase Matching Technique

When the pump and the signal propagate along the nonlinear transmission line, they should exhibit the same propagation delay ($t_p = t_s$ in Fig. 2.8) to maintain their initial phase condition. To satisfy this condition, the pump and the signal should be phase-matched:

$$\begin{cases} \omega_p = 2\omega_s \\ \beta_p = 2\beta_s, \end{cases} \tag{2.29}$$

where ω_p and ω_s are the pump and signal frequencies, respectively, and β_p and β_s are the pump and signal propagation constants, respectively.

However, it is impossible to meet these conditions in a homogeneous discrete transmission line due to dispersion. This is especially the case since the cut-off frequency is close to the pump frequency. For a discrete, homogeneous transmission line, the dispersion relation is given by [14]:

$$\omega = \omega_c \sin(\frac{\beta}{2}), \tag{2.30}$$

where ω_c is the cut-off frequency of the transmission line defined by $\omega_c = 2/\sqrt{LC}$.

As shown in Fig. 2.9, for frequencies closer to the cut-off frequency, the slope of the dispersion plot (i.e., phase velocity) decreases. This results in a phase mismatch of $\Delta\beta$ between the signal and the pump. Unfortunately, we cannot increase the cut-off frequency to alleviate the dispersion, since a higher cut-off frequency corresponds to lower β, which translates to lower gain according to (2.23). Fig. 2.10 shows how the propagation constant mismatch degrades the parametric gain. In addition to the drop in the exponential constant in (2.18), an even more serious effect comes from accumulating the phase mismatch due

28
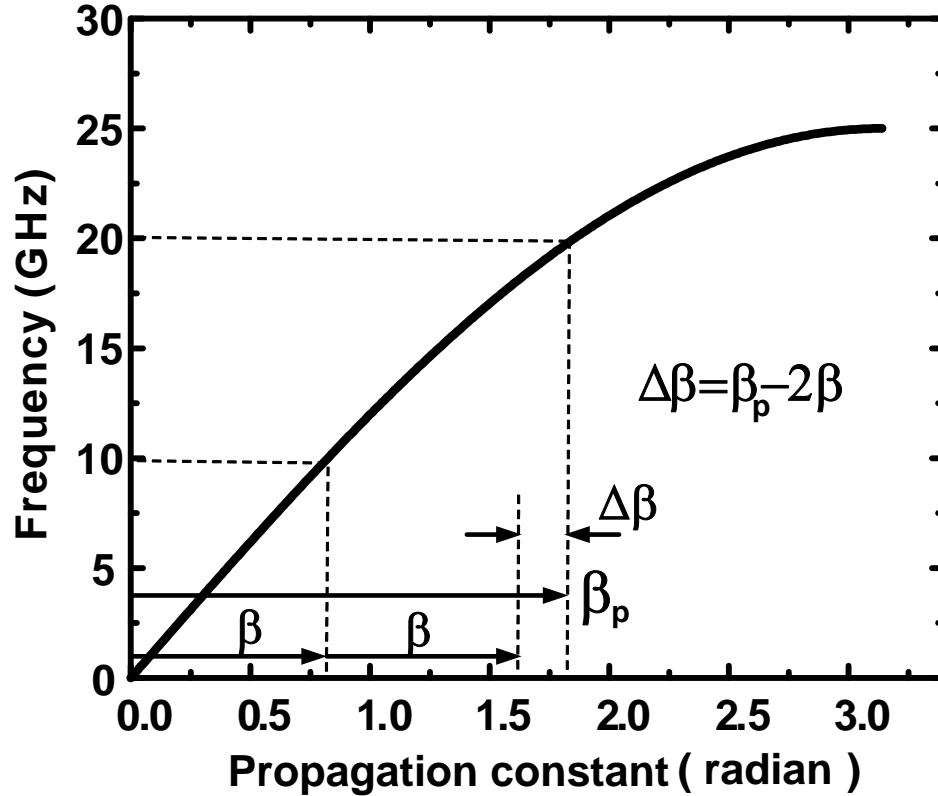
Figure 2.9: Dispersion relation of an artificial transmission line when pump frequency (20 GHz) is comparable to the cut-off frequency (25 GHz).

to differences in the propagation constant. A small phase mismatch is accumulated over multiple sections to reach a certain amount of phase difference between pump and signal, causing attenuation instead of amplification and leading to the curve of the gain plot having a limited maximum gain over the section number. This phase-mismatch effect can be also shown in eqs. (2.15) and (2.16) as $\exp(j\Delta\beta x)$ term in the left-hand side continuously changes the phase relation between pump (A_p) and signal (A).

In optics, birefringence property of propagation medium, which provides different refractive index for different polarization, is used to resolve this prob-
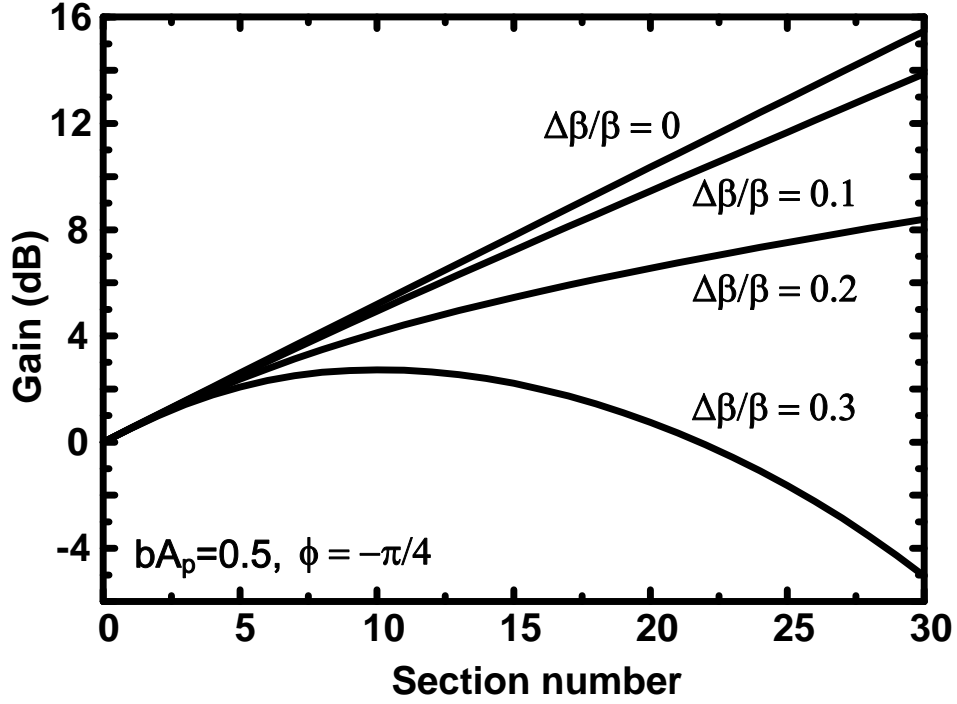
Figure 2.10: Calculated gain versus the section number for different propagation constant mismatches between pump and signal. (l=630 pH, c_0=250 fF, ω=10 GHz)

lem [15]. On the other hand, for isotropic materials, quasi-phase matching technique was proposed by changing polarity of the nonlinearity periodically over the propagation distance [16]. This technique can be easily explained using eqs. (2.15) and (2.16). When a nonlinear coefficient b has a sinusoidal spatial variation over x with a period of $2\pi/\Delta\beta$, b can be written as $b = b_0 \frac{e^{j\Delta\beta x} + e^{-j\Delta\beta x}}{2}$. Inserting this into eqs. (2.15) and (2.16) results in

$$\frac{\partial A}{\partial x} = -\frac{j\beta b_0 A_p}{8}A^* - \frac{j\beta b_0 A_p}{8}A^* e^{j2\Delta\beta x} - \alpha_s A \qquad (2.31)$$

$$\frac{\partial A^*}{\partial x} = \frac{j\beta b_0 A_p^*}{8}A + \frac{j\beta b_0 A_p^*}{8}A e^{-j2\Delta\beta x} - \alpha_s A^*. \qquad (2.32)$$

Then, the left-hand side of eqns. (2.31) and (2.32) has a phase-matched pump-signal interaction in the first term, which can keep contributing to signal gain

30
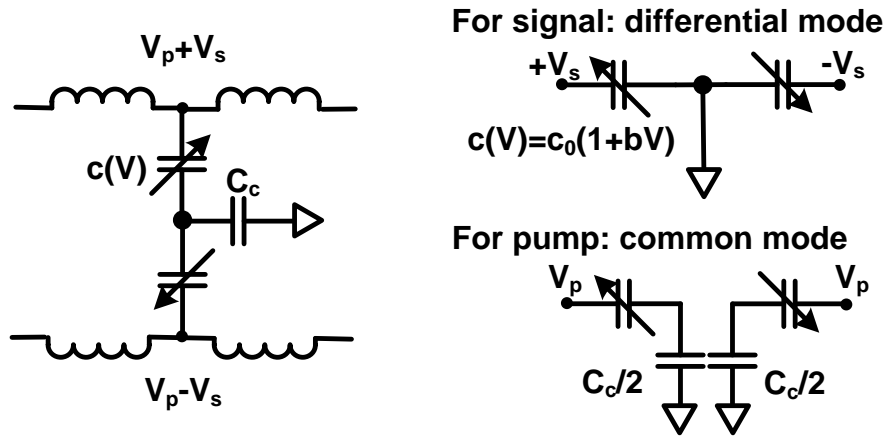
Figure 2.11: Proposed phase matched line: C_c compensates the decrease in the pump propagation velocity due to the dispersion

regardless of phase-mismatched part in the second term. However, it is challenging to apply this method to an electrical nonlinear medium since the spatial variation of the nonlinearity reduces the effective nonlinearity, which significantly degrades the performance in a highly lossy environment.

Here, we propose a simpler but effective solution based on two parallel nonlinear transmission lines with *dispersion compensation capacitors* as shown in Fig. 2.11. In this scheme, the signal is applied differentially to two parallel lines while the pump is a common-mode signal. For differential signals, the net average capacitance is C_0 due to the virtual ground. However, the net average capacitance for the pump drops to C_0 in series with $(C_c/2)$ due to the dispersion compensation capacitor. This decreases the pump propagation delay without changing the signal propagation, canceling the dispersion of the nonlinear transmission line. Fig. 2.12 shows the effect of proposed phase matching on parametric amplification using Spectre in Cadence.
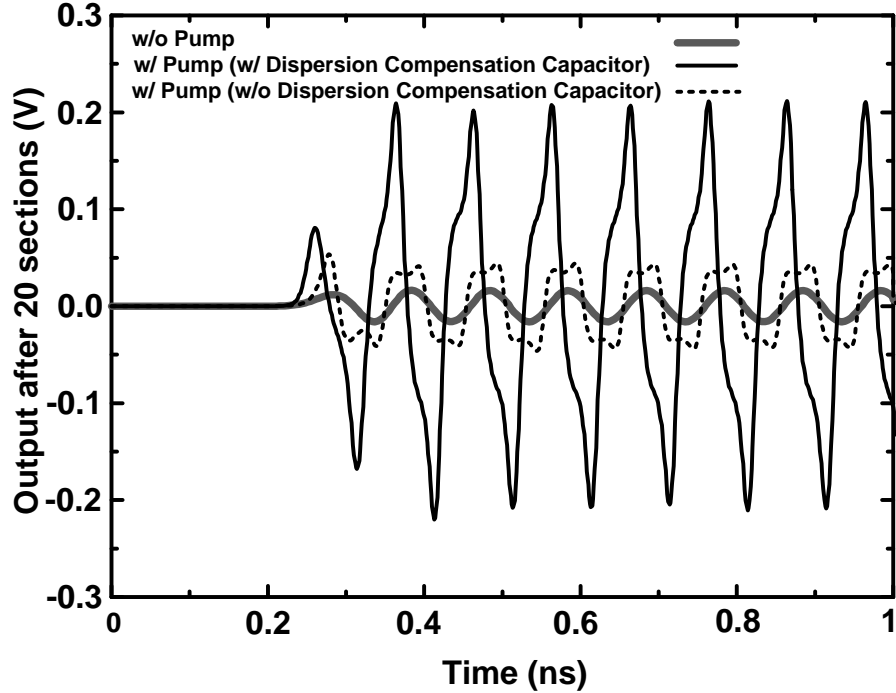
Figure 2.12: The effect of the dispersion compensation capacitor, C_c, for phase matching (ω = 10 GHz, n = 20, l = 630 pH, c_0 = 250 fF, C_C = 1.2 pF)

2.2.3 Pump Loss Effect

The previous sections examined the signal gain in the absence of pump attenuation for an analytical solution. However, pump loss is critical since the signal gain is an exponential function of the pump amplitude. We simulate the gain of the traveling-wave parametric amplifier depending on the presence of dispersion compensation capacitor C_c as shown in Fig. 2.13. For this simulation, we use real models of varactors and inductors in a 0.13-μm CMOS process. The signal and pump frequencies are 10 GHz and 20 GHz, respectively. The cut-off frequency of the transmission line is 25 GHz, and the common-mode pump amplitude is 500 mV. The quality factors of the transmission line are 11.3 and 10 at the signal and pump frequencies, respectively. Although the proposed disper-

32
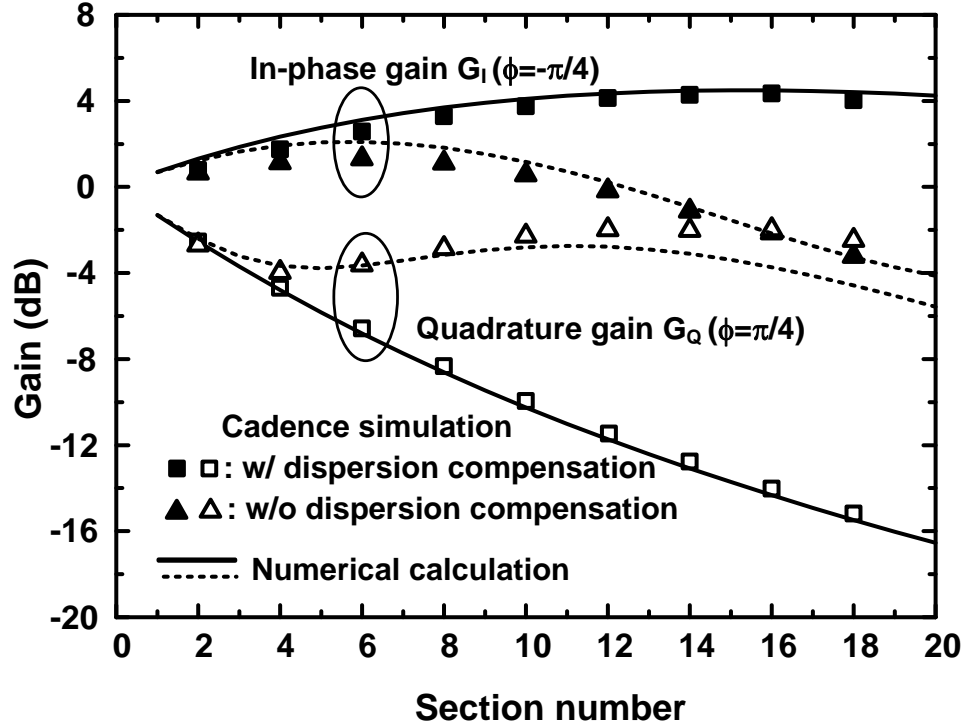
Figure 2.13: Simulated in-phase and quadrature gain of traveling-wave parametric amplifier with and without the dispersion compensation capacitor, C_c.

sion compensation improves the parametric gain, the maximum in-phase gain is only 4.3 dB after 16 sections. This shows that a simple traveling-wave design is not efficient for parametric amplification in terms of gain and chip area, especially in CMOS, where low quality factor of inductors and capacitors results in high attenuation for both signal and pump. For instance, if the pump power falls below a certain level and the loss per unit length is higher than the gain exponent (parameter S in (2.23)), overall the structure shows attenuation instead of amplification.

BIBLIOGRAPHY

[1] R.A. Baugartner and R.L. Byer, "Optical Parametric Amplification," *IEEE J. of Quantum Electronics*, vol. QE-15, no. 6, pp. 432-444, Jun. 1979.

[2] L.T. Carneiro and C.C. Rapozo, "Parametric Amplification in a Low-Density Plasma Sheath," *Physical Review A*, vol. 43, no. 8, pp. 4473-4479, Apr. 1991.

[3] W.H. Louisell, *Coupled mode and Parametric electronics*, Wiley, New York, NY, 1960.

[4] R. Landauer, "Parametric Amplification Along Nonlinear Transmission Lines," *Journal of Applied Physics*, vol. 31, pp. 479-484, 1960.

[5] J.M. Manley and H.E. Rowe, "Some General Properities of Nonlinear Elements –Part I. General Energy Relations," *Proc. IRE*, pp. 904-913, July 1956.

[6] S. Ranganathan and Y. Tsividis, "A MOS Capacitor-Based Discrete-Time Parametric Amplifier with 1.2 V Output Swing and 3 μW Power Dissipation," in *IEEE Int. Sold State Circuits Conf. (ISSCC) Dig. Tech. Papers*, Feb. 2003, pp. 406-407.

[7] S. Ranganathan and Y. Tsividis, "Discrete-Time Parametric Amplification Based on a Three-Terminal MOS Varactor: Analysis and Experimental Results," *IEEE J. Solid-Stat Circuits*, vol. 38, no. 12, pp. 2087-2093, Dec. 2003.

[8] P.M. Figueiredo and J. C. Vital, "The MOS Capacitor Amplifier,"*IEEE Trans. Circuits Syst. II, Exp. Briefs*, vol. 51, no. 3, pp. 111-115, Mar. 2004.

[9] S. Magierowski, H. Chan, and T. Zourntos,"Subharmonically Pumped RF CMOS Paramps,"*IEEE Trnas. Electron. Devices*, vol. 55, no. 2, pp. 601-608, Feb. 2008.

[10] S. Magierowski, T. Zourntos, J. Bousquet, and Z. Zhao,"Compact Parametric Downconversion Using MOS Varactors," in *Proc. IEEE Int. Microwave Symposium*, pp. 1377-1380, June 2009.

[11] W. Lee and E. Afshari, "Parametric Distributed Resonator: A Passive Frequency Divider," to appear in *IEEE J. Solid-Stat Circuits*, 2010.

[12] P.K. Tien and H. Suhl, "A Traveling-wave Ferromagnetic Amplifier," *Proc. IRE*, vol. 46, pp. 700-706, April 1958.

[13] P.K. Tien, "Parametric Amplification and Frequency Mixing in Propagating circuits," *Journal of Applied Physics*, vol. 29, no. 9, pp. 1347-1357, Sep. 1958.

[14] L. Brillouin, *Wave Propagation in Periodic Structures*, Dover, New York, 1946.

[15] R.W. Boyd, *Nonlinear Optics*, Elsevier, Burlington, MA, 2008.

[16] L.E. Myers, R.C. Eckardt, M.M. Fejer, and R.L. Byer, "Quasi-Phase-Matched Optical Parametric Oscillators in Bulk Periodically Poled *LiNbO$_3$*," *J. Opt. Soc. Am. B*, vol. 12, no. 11, pp. 2102-2116, Nov. 1995.

CHAPTER 3

DISTRIBUTED PARAMETRIC RESONATOR: A PASSIVE CMOS
FREQUENCY DIVIDER

3.1 Introduction

The frequency divider is an essential block in phase-locked loops (PLLs) and frequency synthesizers. The design of the frequency divider block in any system is critical, since it consumes a large portion of the overall system power and it is one of the key contributors to the phase noise. The design of the frequency divider becomes even more challenging at high frequencies due to the limited speed of digital gates in a conventional digital frequency divider [1]. At these frequencies an injection-locked frequency divider has been a good candidate due to its high speed and low power consumption [2–4]. Although there have been several works to further minimize the power consumption of the injection-locked frequency divider, the use of transistors for sustaining oscillation limits these efforts. Moreover, the channel noise caused by transistors degrades the output phase noise at a large offset frequency or near the edge of the locking range [5–8].

To overcome these limits, we propose to use *parametric oscillator*, which is a harmonic oscillator sustained by the parametric amplification. The oscillation frequency in the parametric oscillator is synchronized to one of the subharmonics of the pump signal. This phenomenon can be exploited to make a frequency divider. There have recently been a few works on parametric frequency dividers on printed circuit boards (PCB). However, the operation frequency is limited up to 2 GHz and it is non-integrable in a CMOS process [11–13].

In this chapter, we use the concept of parametric oscillation to design the first passive 20 GHz CMOS frequency divider. It consists of two parallel non-linear transmission lines using MOS-varactors, forming a reflective distributed resonator. Its operation principle is the electronic analogue to that of the optical parametric oscillator [14], [15]. This distributed structure enables a stable start-up condition and a broad range of frequency tunability. Moreover, the reflective resonator minimizes the number of components and forms a standing wave, which suppresses the pump signal at the output while maintaining a large output signal amplitude. In addition to zero static power consumption, the proposed frequency divider shows better phase noise performance even at high offset frequencies since it does not have the channel noise from the transistors.

The rest of the chapter is organized as follows. Section 3.2.1 discusses the theoretical analysis of parametric oscillation, the standing wave formation of the reflective resonator, and a unique input matching characteristic. Section 3.3 discusses the phase noise performance and compares it with the injection-locked frequency divider. Section 3.4 summarizes the design procedure and the measurement results. Finally, section 3.5 compares the proposed divider with other dividers with no static power consumption and its applications.
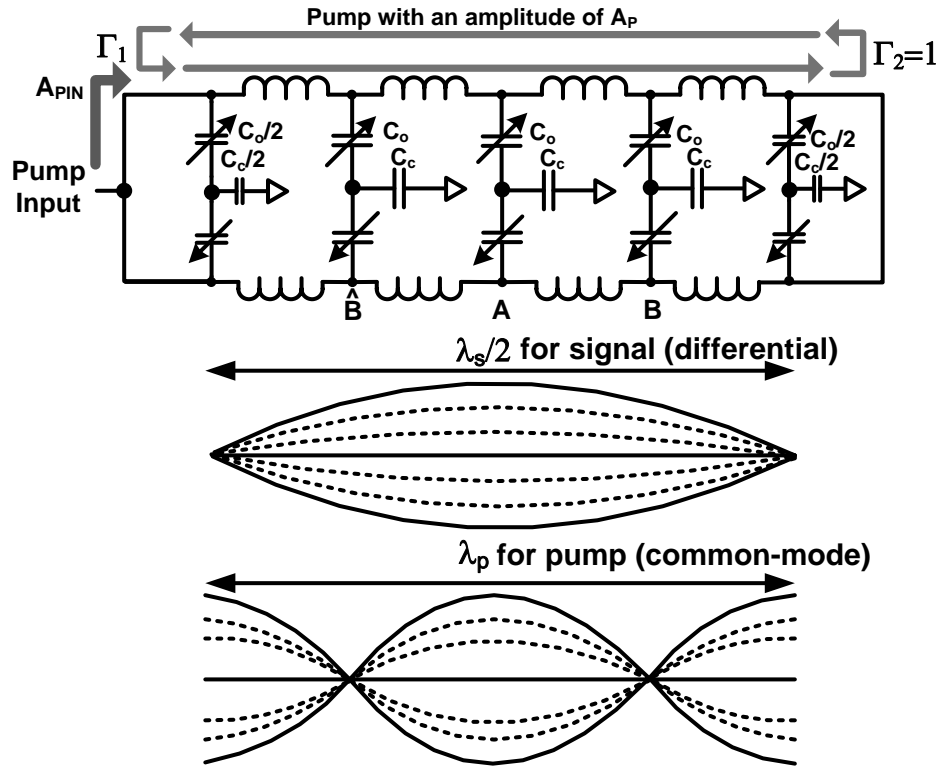
Figure 3.1: Distributed resonator with two reflective ends and different standing wave formation for pump and signal

3.2 Parametric Oscillator for Frequency Division

3.2.1 Theoretical Analysis

Parametric oscillation occurs when the parametric amplification compensates the loss of a resonator at the resonance frequency. Here, we use this concept to demonstrate a frequency divider by considering the pump as the input signal. Fig. 3.1 shows the structure of the proposed parametric oscillator. It consists of two transmission lines with four phase-matched LC sections that are tied at both ends. Oscillation starts from the ambient thermal noise of the resonator

when the pump is strong enough to compensate the loss. Any arbitrary thermal noise pair on the differential transmission lines can be represented as the sum of common-mode and differential components. However, only differential component grows by traveling back and forth between two reflective ends through the degenerate parametric amplification since the phase match is achieved as shown in Fig. 2.11. On the other hand, the common-mode component is suppressed due to the resonator loss. The amplitude of the differential component will increase up to the point where the gain and the loss are equal due to the gain saturation. The gain saturation occurs through *pump depletion* which means that the pump level is depleted due to the large energy flow from the pump to the signal frequency.

In order to calculate the steady-state output amplitude, we start with the coupled-mode equations (2.15) and (2.16) in section 2.2 for $\phi = \pi/2$. After adding the transmission line loss and the pump depletion in these equations, the coupled-mode equations can be modified to:

$$\frac{\partial A}{\partial x} = -\alpha_s A + \frac{\beta b A_p}{4} A^* \tag{3.1}$$

$$\frac{\partial A^*}{\partial x} = -\alpha_s A^* + \frac{\beta b A_p^*}{4} A \tag{3.2}$$

$$\frac{\partial A_p}{\partial x} = -\alpha_p A_p - \beta b |A|^2 + \kappa A_{pin} \tag{3.3}$$

where α_s and α_p are the attenuation constants of the transmission line at signal and pump frequencies, respectively. A_{pin} is the input amplitude into each transmission line of the resonator. κA_{pin} represents the increase in the pump amplitude inside the resonator due to the input signal. The significance of this term will be seen for the standing wave resonator when reflections are taken into account, which will be presented in (3.10). In equation (3.3), the second term on the right corresponds to the pump depletion. This term can be easily obtained

by adding the second harmonic generation of the signal in (2.7) to (2.8).

For the steady state solution where gain and loss are equal, so that the signal amplitude is constant over the propagation, $\partial A/\partial x$, $\partial A^*/\partial x$, $\partial A_p/\partial x$ are set to be zero. In this case, combining (3.1) and (3.2) results in:

$$|A|_{steady} = 0 \text{ or } A_p|_{steady} = \frac{4\alpha_s}{\beta b}. \tag{3.4}$$

Non-zero output condition leads us to choose $A_p|_{steady} = 4\alpha_s/\beta b$ in (3.4) and to insert this into (3.3), which can be rearranged as[1]:

$$|A|^2_{steady} = \frac{1}{\beta b}\left(\kappa A_{pin} - \alpha_p A_p|_{steady}\right) \tag{3.5}$$

$$= \frac{\kappa^2}{4\alpha_s\alpha_p}A_{pin}|^2_{th}\left(\frac{A_{pin}}{A_{pin}|_{th}} - 1\right) \text{for } A_{pin} > A_{pin}|_{th}, \tag{3.6}$$

where a threshold input pump amplitude is given by:

$$A_{pin}|_{th} = \frac{\alpha_p}{\kappa}A_p|_{steady}. \tag{3.7}$$

At the resonator end where the pump is injected, the relation between m^{th} and $(m + 1)^{th}$ round-tripped pump amplitudes, A_{p_m} and $A_{p_{m+1}}$, is:

$$A_{p_{m+1}} = A_{p_m}\exp(-2\alpha_p d) + A_{pin} \tag{3.8}$$

where $2d$ is the round-trip length of the resonator. In the steady state, $A_{p_{m+1}}=A_{p_m}=A_p|_{steady}$, $A_p|_{steady}$ linearly increases with A_{pin} for $A_{pin} \leq A_{pin}|_{th}$ by inserting $|A|_{steady} = 0$ into (3.3). However, $A_p|_{steady}$ becomes constant with A_{pin} once a parametric oscillation starts for $A_{pin} > A_{pin}|_{th}$. Hence, beyond an oscillation threshold, equation (4.23) becomes:

$$A_{pin}|_{th} = A_p|_{steady}(1 - \exp(-2\alpha_p d)). \tag{3.9}$$

---

[1]The steady state solution turns out to be unconditionally stable from nonlinear stability theory.

Combining (3.7) and (3.9), κ is reduced to:

$$\kappa = \frac{\alpha_p}{(1 - \exp(-2\alpha_p d))}. \tag{3.10}$$

From (3.6) and (3.10), the steady state amplitude of the output signal becomes:

$$|A|_{steady} = \frac{A_{pin}|_{th}}{2(1 - \exp(-2\alpha_p d))} \sqrt{\frac{\alpha_p}{\alpha_s}} \sqrt{\frac{A_{pin}}{A_{pin}|_{th}} - 1} \tag{3.11}$$

where

$$A_{pin}|_{th} = \frac{4\alpha_s(1 - \exp(-2\alpha_p d))}{\beta b} = \frac{2(1 - \exp(-2\alpha_p d))}{Q_s b}. \tag{3.12}$$

Note that $|A|_{steady}$ is a steady-state amplitude of a traveling wave in one direction, and that the measured voltage at output node is the superposition of forward and backward waves, forming a standing wave. Therefore, the output voltage measured at x_{out} is $\gamma |A|_{steady}$ where $\gamma \simeq 2|\sin(\beta x_{out})|$ for a resonator length of $d = \lambda_s/2$.

So far, we assumed that pump is perfectly reflected back at both ends of the resonator. However, we connect the external signal source with a finite output impedance, Z_{out}, at one end of the resonator to supply a pump. This finite output impedance makes the input-side reflection coefficient, Γ_1, smaller than 1, thereby resulting in additional loss of pump. As a result we need to introduce an effective pump loss, α_{pe}, to replace α_p which solely comes from the transmission line loss. The pump round-trip loss including the additional loss due to imperfect reflection can be expressed by:

$$\exp(-2\alpha_{pe} d) = \Gamma_1 \exp(-2\alpha_p d) \tag{3.13}$$

$$\alpha_{pe} = \alpha_p - \frac{\ln \Gamma_1}{2d}, \tag{3.14}$$

41
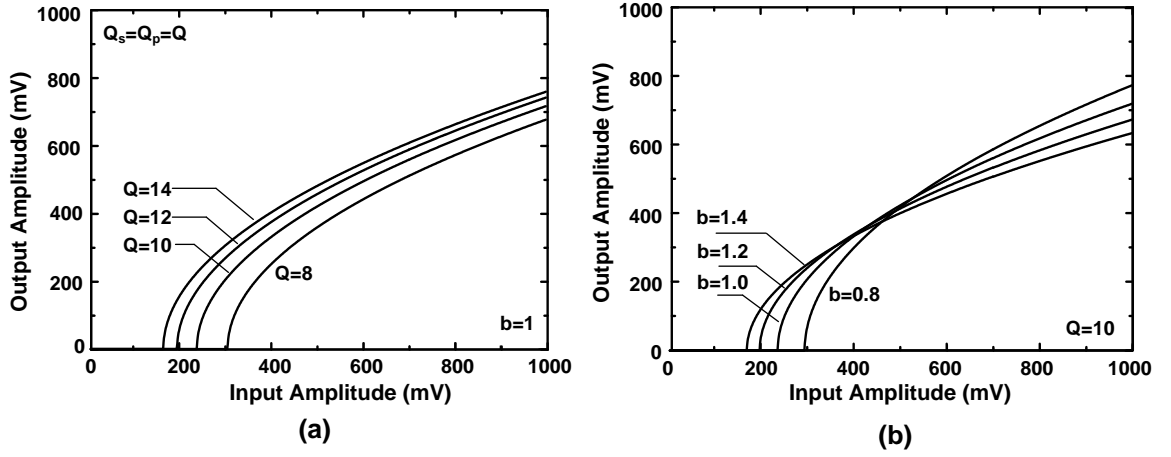
Figure 3.2: Calculated output amplitude versus input amplitude: (a) the effect of loss represented by different quality factors at 10 GHz (b) the effect of nonlinearity represented by C/V slope, b. (f_c=25 GHz, f_{in}=20 GHz, Z_o=50 Ω, Z_{out}=50 Ω, n=4)

where Γ_1 is the input-side reflection coefficient given by:

$$\Gamma_1 = \frac{2Z_{out} - Z_0}{2Z_{out} + Z_0} \tag{3.15}$$

and Z_0 is the characteristic impedance of each transmission line. It is noted that the differential oscillation signal does not see the signal source impedance due to the virtual ground.

Fig. 3.2 shows the calculated output amplitude versus the input amplitude based on (3.11) after replacing α_p with α_{pe}. To investigate the effect of the loss and the nonlinearity, we change the quality factor of the transmission line and varactor C/V slope, b. As expected from (3.12), the oscillation threshold decreases as the resonator loss decreases and the nonlinearity of the varactor increases. However, the slope of the output amplitude versus input amplitude varies in a different way: while lower loss still gives higher slope, the high nonlinearity results in lower slope due to the higher pump depletion. In a real system, additional losses from vias and interconnects decrease the effective qual-

ity factor of the line, and the parasitic capacitance around transmission lines decreases the nonlinearity. These non-ideal effects require careful attention to layout.

The lower part of Fig. 3.1 shows different standing wave formations inside the resonator for pump and signal. The differential signal sees the resonator ends as shorts due to the virtual ground, while the common-mode pump sees the ends as open nodes. With the reflection at both ends, the signal forms a $\lambda_s/2$ standing wave with minimum amplitudes at both ends. On the other hand, the pump forms a λ_p standing wave with maximum amplitudes at both ends. The higher modes for pump and signal are suppressed by the cut-off frequency of the resonator.

The oscillation frequency is determined by the standing wave formula:

$$d = nh = \frac{\lambda_s}{2} = \frac{\pi}{\beta} = \frac{1}{2 f_{osc} \sqrt{(l/h)(c_0/h)}} \tag{3.16}$$

where d is the physical length of the transmission line, h is the spacing between two adjacent nodes, and n is the number of sections of the resonator. The varactor capacitance per unit section is approximated by its average value, c_0. Equation (3.16) can be rearranged to:

$$f_{osc} = \frac{1}{2n \sqrt{l c_0}}. \tag{3.17}$$

The loop gain at a given oscillation frequency in a resonator with n sections is roughly:

$$G_{loop} = \exp(\frac{b A_p \omega_{osc} \sqrt{l c_0}}{4} \cdot 2n) = \exp(\frac{\pi b A_p}{2}). \tag{3.18}$$

This equation shows that the loop gain at a fixed oscillation frequency does not depend on the number of sections. In our design, we set n to be four for

small footprint and reasonable attenuation especially for the pump signal. Another reason for having four sections is that we can exploit the different standing wave formations for pump and signal to suppress the pump frequency at the output.

There are three possible nodes for taking the signal out of the resonator as shown in Fig. 3.1. "A" provides the maximum amplitude for both pump and signal, and the pump signal will be filtered out only if the output signal is taken differentially from the two transmission lines. However, we need an extra low-pass filter for a single-ended output at "A." On the other hand, "B" or "$\hat{B}$" can suppress the pump even for the single-ended output thanks to the standing-wave formation. The down side is a lower signal amplitude compared to "A." "B" is more appropriate for the suppression of the pump than "$\hat{B}$," because the amplitude imbalance between forward and backward waves due to the loss is smaller in this node. In addition, the external connection for the output adds a parasitic conductance to the resonator, resulting in extra loss. The power dissipation caused by the additional conductance is $P_{diss} = 1/2GV_p^2$, which is proportional to the square of the pump amplitude. Therefore, connecting the output port at "A" leads to the maximum loss in the pump amplitude, and it raises the threshold voltage and decreases the amplitude of the signal.

The remaining challenge is to inject pump power into the resonator effectively. For pump, the resonator is simply two parallel open-ended transmission lines with a length of λ_p. The input impedance looking into one end of the res-

onator is [27]:

$$Z_{in} \;=\; \frac{Z_0}{2}\,\frac{1}{\tanh(\alpha_p + j\beta_p)\lambda_p} \tag{3.19}$$

$$\simeq \frac{Z_0}{2}\left[\frac{\alpha_p\lambda_p - j\cos(\beta_p\lambda_p)\sin(\beta_p\lambda_p)}{(\alpha_p\lambda_p\cos(\beta_p\lambda_p))^2 + \sin^2(\beta_p\lambda_p)}\right]_{\omega=\omega_p} \tag{3.20}$$

$$= \frac{Z_0}{2\alpha_p\lambda_p} = \frac{Q_p Z_0}{2\pi} \tag{3.21}$$

where Z_0 is the characteristic impedance of each transmission line and Q_p is the resonator quality factor at the pump frequency. The input impedance becomes purely real at the resonance frequency and its harmonics. By selecting the right value for the characteristic impedance for a given quality factor, one can achieve the input matching without an additional matching network. Considering that Q_p in our design is around 7 in 0.13 μm CMOS process, Z_0 of 50 Ω provides a good input match to 50 Ω source according to (3.21).

3.2.2 Stability Test

In the previous section, it was assumed that eqs.(3.1)–(3.3) have a stable steady-state solution of eq.(3.11). This section will validate this stability assumption [24]. First, we introduce new variables P and Q to obtain fixed points in eqs.(3.1)–(3.3), where $A = P + jQ$. We also set $S = \beta b A_p/4$ and $E = \beta\kappa b A_{pin}/4$ for simplification. Then, equations (3.1)–(3.3) can be rewritten as

$$\frac{\partial P}{\partial x} \;=\; -\alpha_s P + SP \tag{3.22}$$

$$\frac{\partial Q}{\partial x} \;=\; -\alpha_s Q - SQ \tag{3.23}$$

$$\frac{\partial S}{\partial x} \;=\; -\alpha_p S - \left(\frac{\beta b}{2}\right)^2(P^2 + Q^2) + E. \tag{3.24}$$

By putting $\partial P/\partial x = \partial Q/\partial x = \partial S/\partial x = 0$, we can obtain two fixed points given by $(P, Q, S)_1 = (0, 0, E/\alpha_p)$ for $E < \alpha_s \alpha_p$

$(P, Q, S)_2 = (\frac{2}{\beta b} \sqrt{E - \alpha_s \alpha_p}, 0, \alpha_s)$ for $E > \alpha_s \alpha_p$.

Next, when a small perturbation $(\delta_1, \delta_2, \delta_3)$ is applied around $(P, Q, S)_1$, eqs.(3.22)–(3.24) can be rewritten and approximated to the first order of δ as

$$\frac{\partial \delta_1}{\partial x} \cong \left(\frac{E - \alpha_p \alpha_s}{\alpha_p}\right) \delta_1 \tag{3.25}$$

$$\frac{\partial \delta_2}{\partial x} \cong -\left(\frac{E}{\alpha_p} + \alpha_s\right) \delta_2 \tag{3.26}$$

$$\frac{\partial \delta_3}{\partial x} \cong -\alpha_p \delta_3 \tag{3.27}$$

The left-hand side of eqs. (3.25)–(3.27) shows $\partial \delta_1 / \partial x < 0$, $\partial \delta_2 / \partial x < 0$, and $\partial \delta_3 / \partial x < 0$ for $E < \alpha_s \alpha_p$, which proves that $(P, Q, S)_1$ is stable. For the other fixed point $(P, Q, S)_2$, we can take the same step as we did for $(P, Q, S)_1$, which gives

$$\frac{\partial \delta_1}{\partial x} \cong \frac{2}{\beta b} \sqrt{E - \alpha_p \alpha_s} \delta_3 \tag{3.28}$$

$$\frac{\partial \delta_2}{\partial x} \cong -2\alpha_s \delta_2 < 0 \tag{3.29}$$

$$\frac{\partial \delta_3}{\partial x} \cong -\alpha_p \delta_3 - \beta b \sqrt{E - \alpha_p \alpha_s} \delta_1. \tag{3.30}$$

Combining eqs. (3.28) and (3.30) results in

$$\frac{\partial^2 \delta_3}{\partial x^2} + \alpha_p \frac{\partial \delta_3}{\partial x} + 2(E - \alpha_s \alpha_p) \delta_3 = 0. \tag{3.31}$$

Equation (3.31) exhibits a damped oscillation for $\alpha_p > 0$ and $E > \alpha_s \alpha_p$, which is stable. we can also obtain a damped oscillation equation for δ_1.

Therefore, when $E < \alpha_s \alpha_p$, the fixed points at $(P, Q, S)_1 = (0, 0, E/\alpha_p)$ is stable. This means that there is no output at half of an input frequency. As E increases

higher than $\alpha_p \alpha_s$, $(P, Q, S)_1$ loses stability and a new stable fixed point appears at $(P, Q, S)_2 = (\frac{2}{\beta b} \sqrt{E - \alpha_s \alpha_p}, 0, \alpha_s)$, corresponding to parametric oscillation.

3.3   Comments on Phase Noise Performance

One of the main advantages of our design is a better phase noise performance than the conventional injection-locked frequency dividers. In an LC oscillator where transistors are used for sustaining oscillation, the channel noise makes the main contribution to the phase noise [22]. Although the phase noise of the injection-locked frequency divider tracks that of the injected signal at low offset frequencies, the excess noise from the divider degrades the phase noise back to the level of a free-running LC oscillator at higher offset frequencies [6]. Our design does not have any transistors, thus guaranteeing that it has a low phase noise floor [23].

The other interesting point is that our frequency divider has high spectral purity because of its phase selection property as shown in equation (2.23). Start-up noise such as a thermal noise grows by the degenerate parametric amplification for a pump power over the threshold. The degenerate parametric amplification picks a limited noise component to be amplified in terms of phase and frequency. This is because the degenerate parametric amplification works only for $\omega = \omega_p/2$ and a specific initial phase difference between signal and pump as we discussed in the section 2.2.

Fig. 3.3 shows the simulated phase noise performance using Spectre in a 0.13 μm CMOS process. The phase noise difference between input and output is 6 dB over simulation frequencies, which agrees with an ideal value, $20 log_{10} N$ dB,
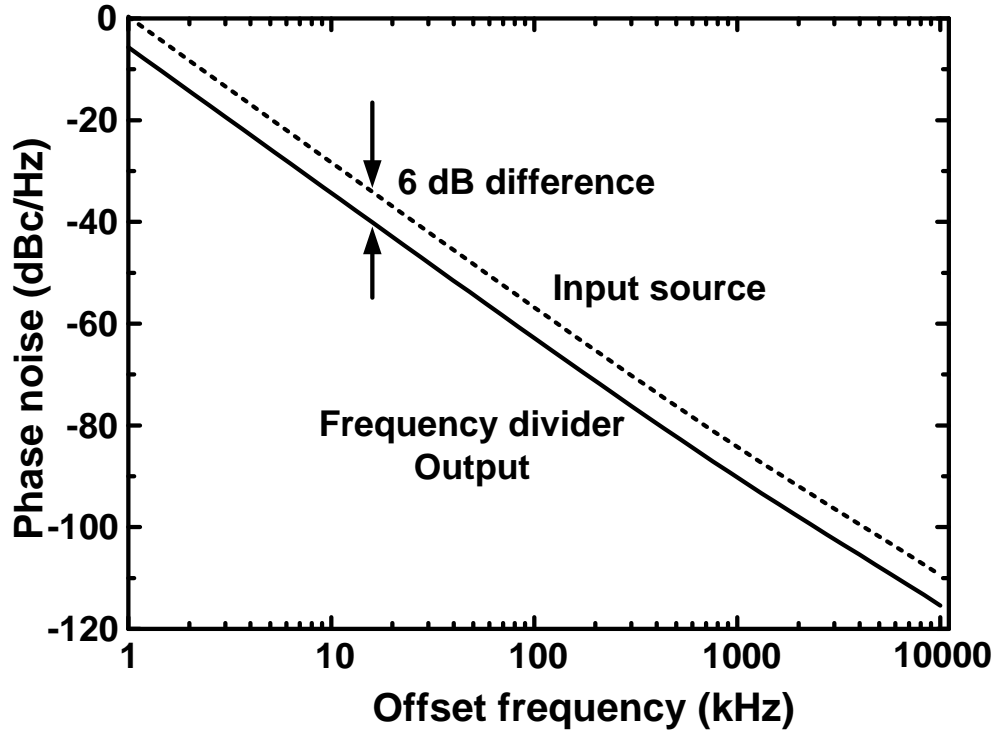
Figure 3.3: Simulated phase noise for a input frequency of 20 GHz using Spectre

for a divide-by-N frequency divider [25].

3.4 Design and Measurement

We design a 20 GHz frequency divider based on the parametric oscillator in a 0.13 μm CMOS process. First, we set the cut-off frequency of the resonator for maximum gain as discussed in Section 2.2. In our design, this optimum value is 25 GHz that determines the product of the inductance and capacitance. The number of sections is set to four as discussed before. These values for the section number and the cut-off frequency guarantee a resonant frequency of 10 GHz. Then, the dispersion compensation capacitor is determined by phase-matching
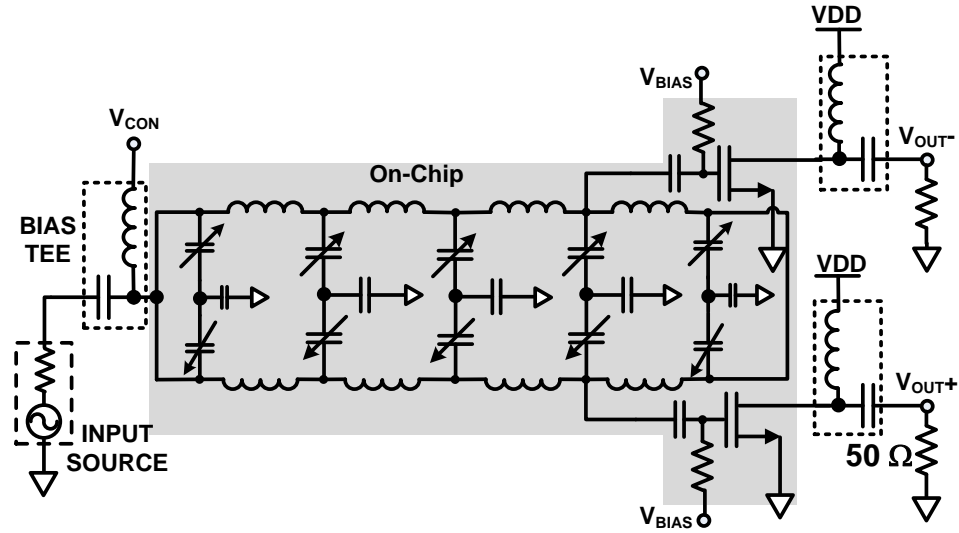
Figure 3.4: Schematic of the frequency divider with buffer and control voltage for frequency tuning.

condition between the pump and the signal. The phase matching can be verified by making sure that the resonance frequency of S_{11} is exactly at 20 GHz. Without the dispersion compensation, S_{11} has a resonance frequency lower than 20 GHz. Finally, depending on the magnitude of the input matching, the characteristic impedance can be selected which gives the ratio of inductance and capacitance. A buffer is added to the output node as shown in Fig. 3.4. Note that the buffer is only needed for testing purposes using a 50 Ω load. The C_{gs} of the buffer transistor adds parasitic capacitance to the nonlinear transmission line, thereby decreasing the nonlinearity of an LC section where the output node is placed. However, the use of multiple LC sections alleviates this effect. Moreover, the buffer capacitance does not affect the operation frequency since it is absorbed into the transmission line. There are two output ports, which give us the option to have single-ended or differential outputs. The oscillation frequency can be tuned by controlling V_{con} through the bias tee at the input port.
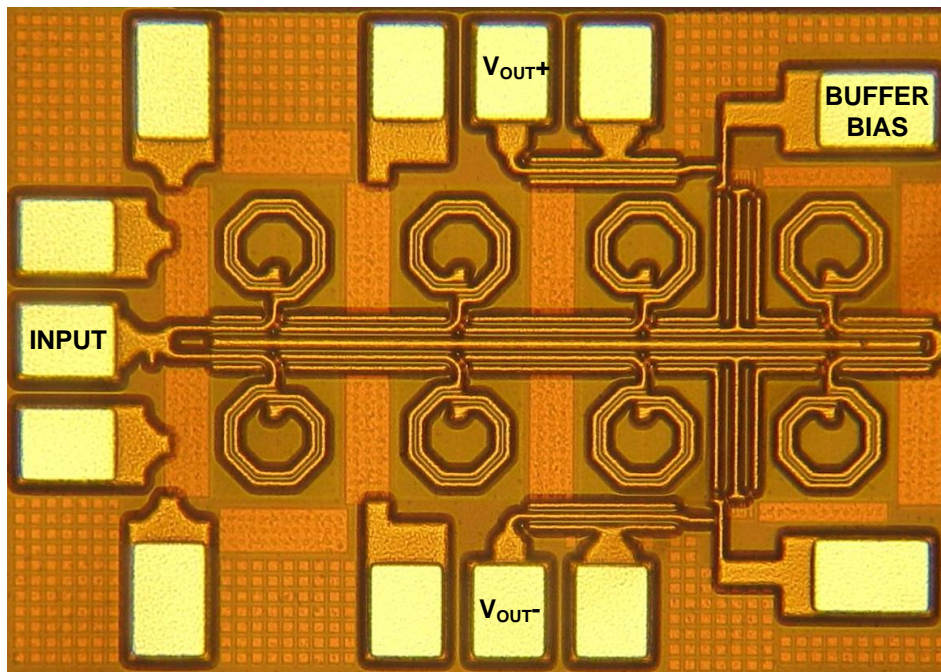
Figure 3.5: Die photograph of the chip

We use ground-shielded spiral inductors with quality factors of around 20 at 20 GHz. In this design, the inductors are around 510pH and occupy $100\mu m \times 100\mu m$. Accumulation-mode NMOS varactors are used as voltage-dependent capacitors. The ratio of minimum-to-maximum capacitances is around 3.5, which represents the nonlinearity of the system. The varactors use the multi-finger gate structure to optimize the nonlinearity and the quality factor simultaneously [28]. For dispersion compensation capacitors, vertical natural capacitors(VNCAP) are used due to their high quality factor [29].

Fig. 3.5 shows the chip photograph implemented in a 0.13 μm CMOS process. The core area of the die is 0.75×0.32 mm^2, not including pads. As the design frequency increases, the sizes of the inductors are scaled down and the whole structure can be made of two parallel transmission lines without spiral
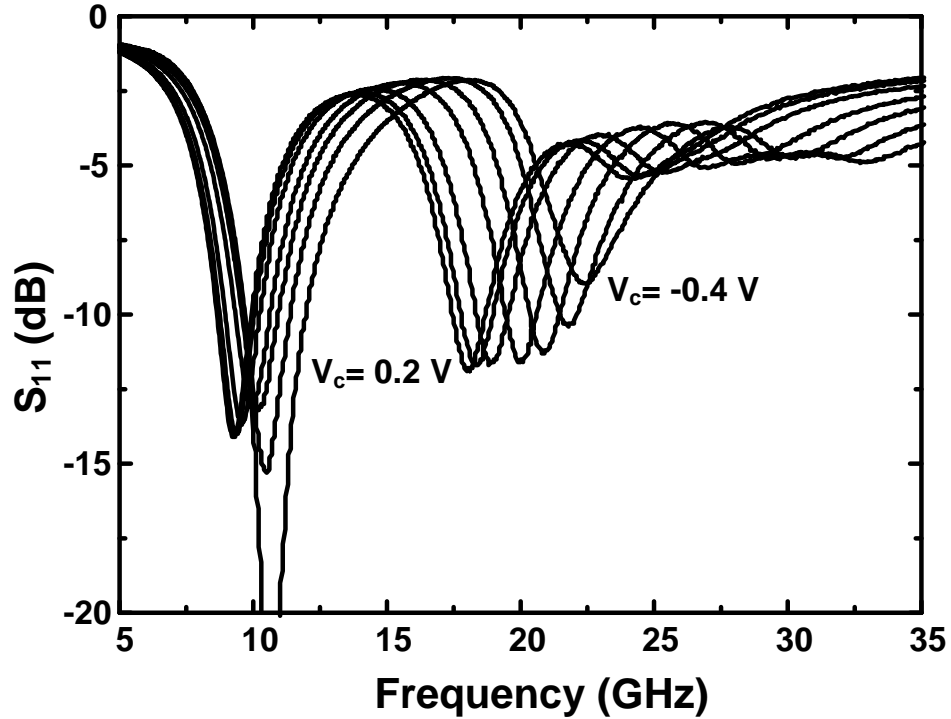
Figure 3.6: Measured input matching for different control voltages from -0.4 V to 0.2 V

inductors. In other words, this frequency divider can easily fit in the entire system layout with great flexibility.

The frequency divider is measured using an Agilent E8257D signal generator for the pump signal and an Agilent 8564EC spectrum analyzer. To measure the input matching, an Agilent E8364B network analyzer is used. We de-embed the loss of all cables, adapters, bias tees, and probes for a more accurate measurement. The bias current for the buffer is set to be 8 mA from a 1.2 V power supply.

S_{11} is measured to investigate the input matching while changing the control voltage. As shown in Fig. 3.6, our frequency divider has a reasonable matching performance of $S_{11} < -10\text{dB}$ over 18 GHz to 22 GHz.
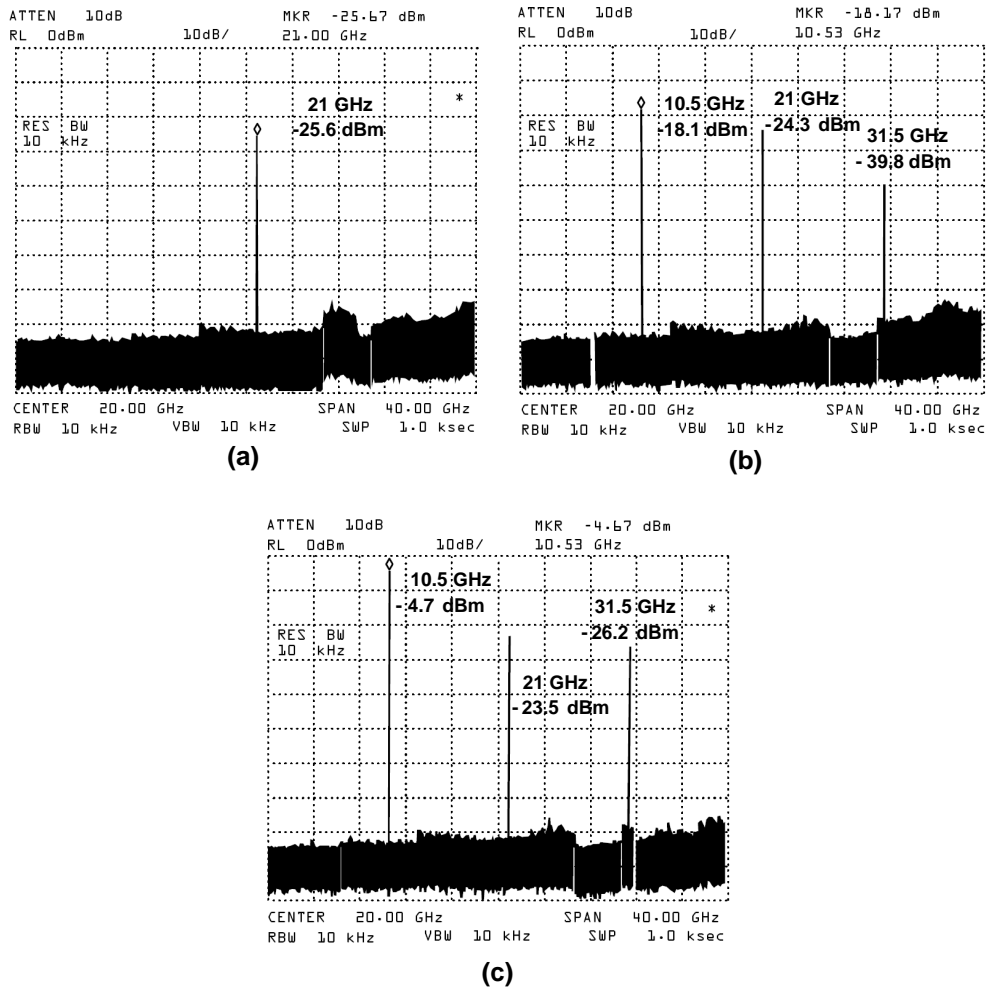
Figure 3.7: Measured single-ended output spectrum for the input amplitude of (a) V_{in} = 300 mV ($< V_{th}$) (b) V_{in} = 440 mV ($\cong V_{th}$) (c) V_{in} = 600 mV ($> V_{th}$)

Next, the single-ended output spectrum is measured against the input (pump) amplitude as shown in Fig. 3.7. For an input amplitude below the threshold, the output spectrum only shows the input frequency, f_{in}. However, as the input amplitude increases beyond the threshold, the $f_{in}/2$ component appears and grows with the input amplitude. Note that the output spectrum at the input frequency stays almost constant as the input amplitude increases, which means that most of the input energy over the threshold is transferred to the $f_{in}/2$
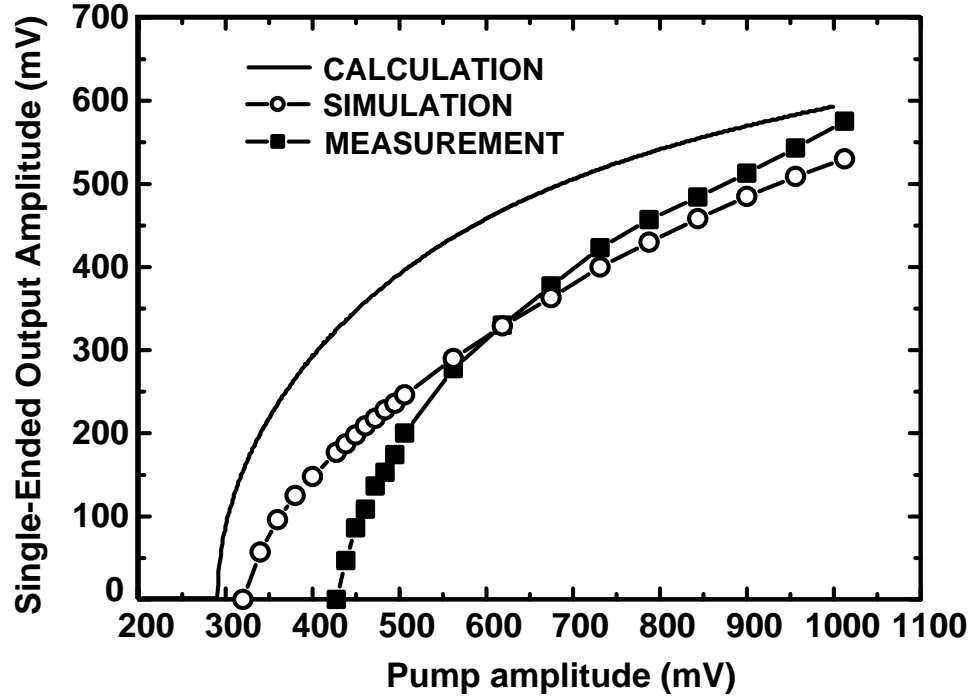
Figure 3.8: Output amplitude at $f_{in}/2$ versus input amplitude at f_{in}

component. This can be also predicted by equation (3.4). In addition, the proposed standing wave formation leads to the suppression of the input frequency at the single-ended output. A $3f_{in}/2$ component is also generated by nonlinear coupling between $f_{in}/2$ and f_{in} components. The harmonics higher than $3f_{in}/2$ are negligible due to the resonator cut-off frequency.

The output amplitude versus the input amplitude is simulated and measured in Fig. 3.8. The measured input threshold is around 400 mV, while the simulated value is 300 mV. The slope of the output amplitude versus input amplitude in the measurement is higher than that of the simulation. This difference can be explained by Fig. 3.2(b). The drop in the nonlinearity caused by the parasitic capacitances (which are linear) increases both the threshold and the slope simultaneously, while some additional loss also contributes to the increase in
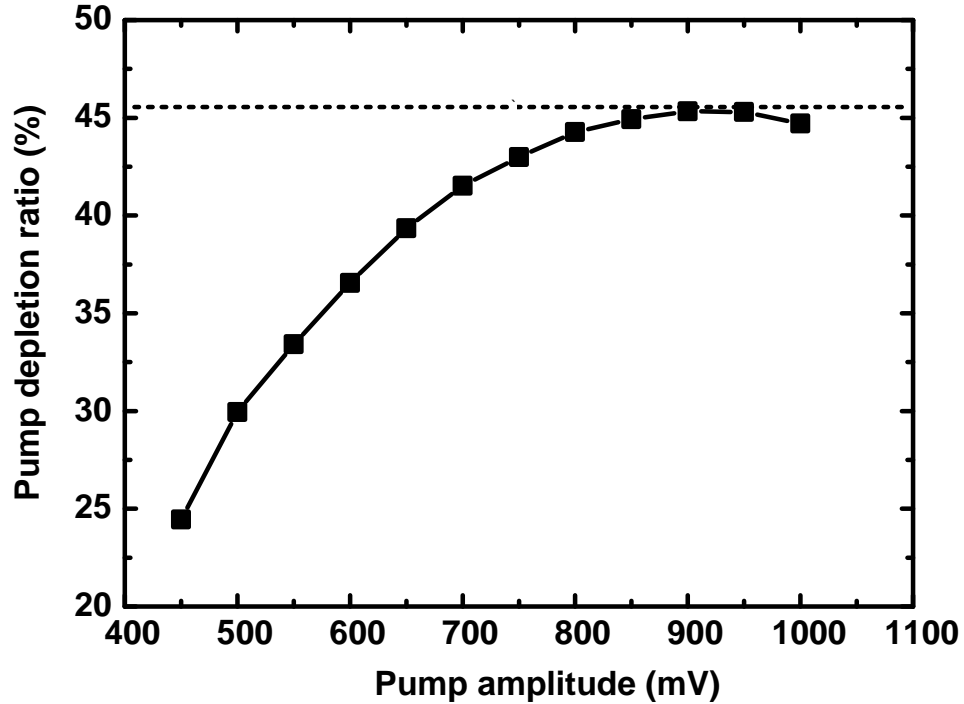
Figure 3.9: Simulated pump depletion ratio for investigation of the frequency conversion efficiency

the threshold. The output amplitude increases with the input amplitude over the threshold following a square-root relation as explained in (3.11). The 600 mV input amplitude results in a 300 mV single-ended output amplitude (600 mV differential output) due to its high frequency conversion efficiency as well as the standing wave formation. The calculation result is also plotted in Fig. 3.8 to verify the analysis in section III. All the parameters for calculation, including quality factors and varactor nonlinearity, are extracted from the Cadence simulation and the simulated transfer function of the output buffer is included for accurate comparison.

The efficiency of the frequency conversion is simulated in terms of pump depletion ratio, which is defined as the ratio of the drop in the pump power to
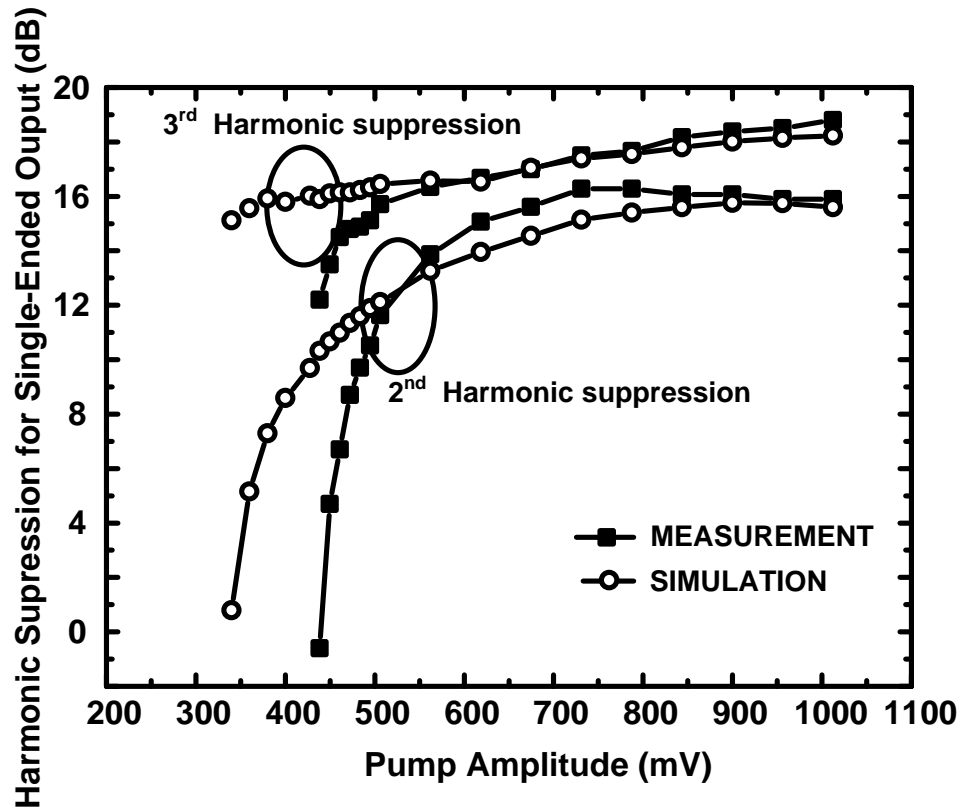
Figure 3.10: Measured second and third harmonic suppression ratio at the single-ended output

the injected pump power after parametric oscillation. Pump depletion occurs because parametric oscillation results in power transfer from the pump to the signal. As the power is transferred, the level of the pump amplitude on the resonator decreases. Therefore, the higher pump depletion means more efficient frequency conversion. However, there are some backconversion processes which drop the efficiency. The sufficiently grown signal at $f_{in}/2$ generates the second harmonic at f_{in}, which returns the power back to the pump. Besides the backconversion by the second harmonic generation, the interaction between signal and pump generates $3f_{in}/2$ component. Then, the interaction between $3f_{in}/2$ and $f_{in}/2$ components increases the f_{in} component through nondegenerate para-
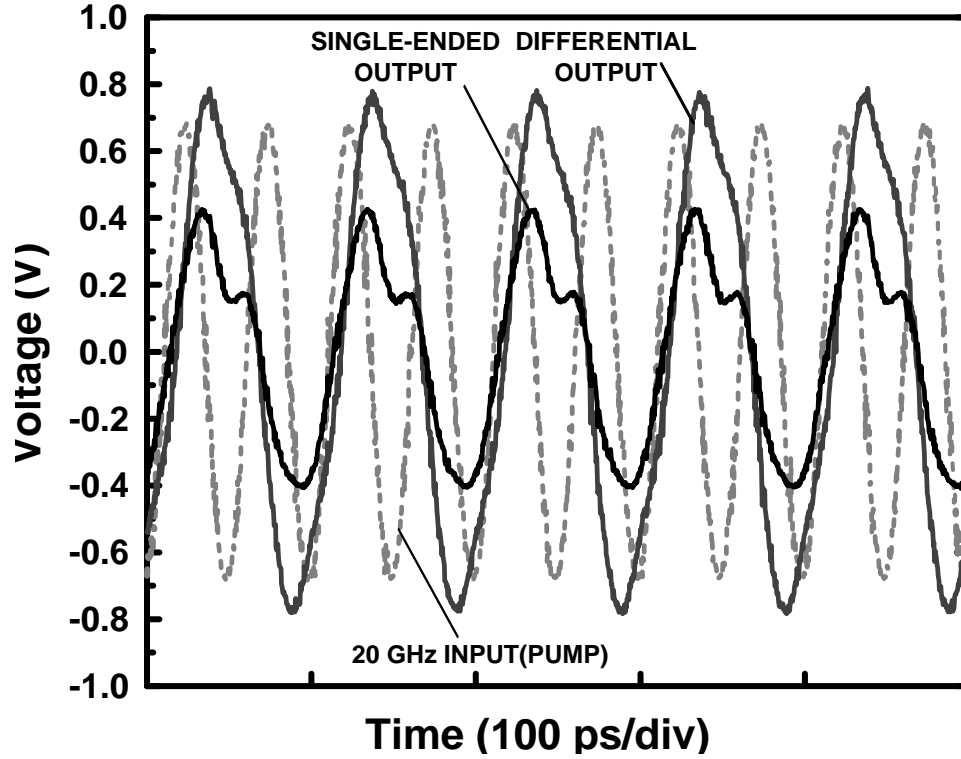
Figure 3.11: Measured output waveform for a 20-GHz input

metric amplification [31]. In Cadence simulation, the pump depletion is found to be 45 % as shown in Fig. 3.9. To exclude the nonlinearity of the buffer, the pump amplitude is simulated before the buffer. The harmonic suppression ratio at the single-ended output is also measured as shown in Fig. 3.10. The suppression ratio for the second (f_{in}) and third ($3f_{in}/2$) harmonics are more than 16 dB due to the standing wave formation and the resonator cut-off frequency that is lower than $3f_{in}/2$. Transient signals are also measured for single-ended and differential outputs using an Agilent 86100C digital communication analyzer with 80-GHz bandwidth as shown in Fig. 3.11.

We measure the threshold voltages over input frequencies for different control voltages to find the tunability as shown in Fig. 3.12. This result demon-
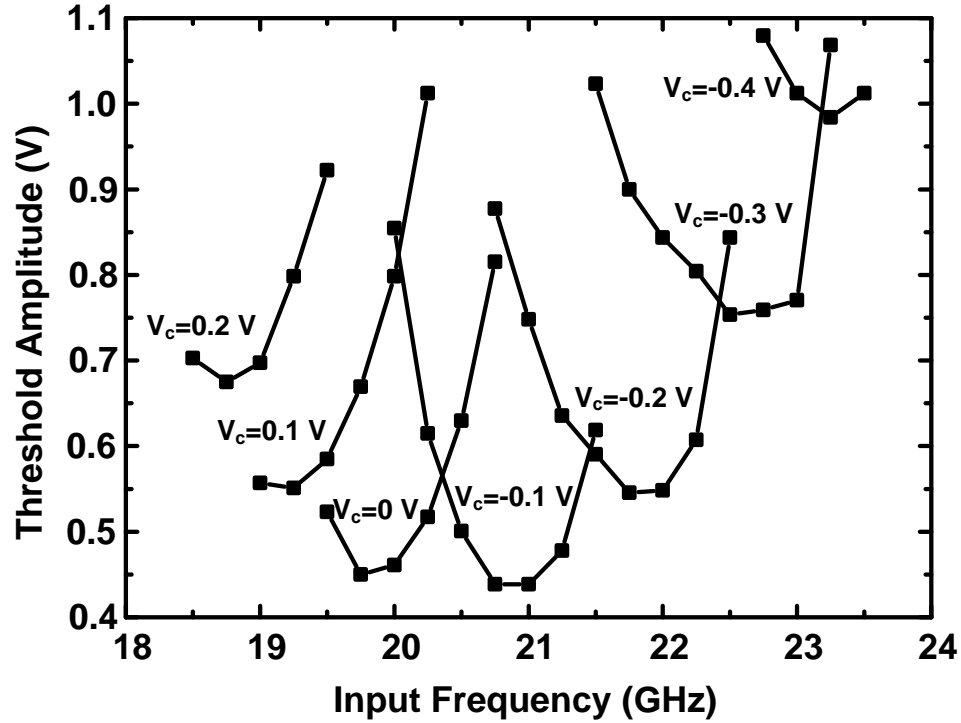
Figure 3.12: Measured threshold versus input frequency for different control voltages

strates a wide tuning range from 18.5 GHz to 23.5 GHz (24%). As the control voltage departs from zero, the C/V slope of the varactor reduces due to the change of the varactor operation regime as shown in Fig. 2.6. As a result, the effective nonlinearity decreases, thereby increasing the threshold voltage. In addition, the dispersion compensation capacitor is still fixed with the change of the varactor, resulting in some phase mismatch. This is another reason for the increased threshold voltage. The increased threshold voltage might limit the use of the proposed frequency divider for low power applications. However, this can be addressed by optimizing the resonator structure and/or increasing the nonlinearity of the varactor: A standing wave formation can be exploited to maximize the quality factor of the resonator by spatially manipulating the characteristic impedance [27]. In addition, we can increase the varactor nonlinearity

by increasing C_{ox} since the varactor capacitance is the series combination of the C_{ox} and voltage-dependent channel capacitance [28]. The CMOS process scaling can result in this desired increase.

For a fixed varactor bias, the operation bandwidth is relatively small, which is another limiting factor of the proposed frequency divider. Basically, the proposed structure is a wave-based oscillator and the round-trip phase is equal to 2π at the oscillation frequency which is half of the pump frequency. When this frequency is the resonant frequency of the structure, the oscillation signal and its nonlinear interaction term with the pump should have the same phase to maintain the round-trip phase of 2π. This leads to $\phi = \pi/2$ in (2.23), which gives the maximum parametric gain. However, when the divide-by-two frequency is deviated from the resonant frequency, the pump selects a signal phase for oscillation that is different from the nonlinear interaction term. The vector sum of the signal and the nonlinear interaction term results in a certain phase shift to satisfy the round-trip phase condition. The deviation from $\phi = \pi/2$ leads to lower parametric gain, thereby increasing the threshold.

Fig. 3.13 shows the measured phase noise. The phase noise difference between input and output is around 6 dB over a wide range of the offset frequency, which agrees with the simulation result shown in Fig. 3.3. Above 1-MHz offset frequency, the noise floor of the spectrum analyzer becomes dominant and the measured phase noise difference decreases. Table 3.1 shows the comparison with state of the art of CMOS frequency dividers at an input frequency of around 20 GHz. As depicted in Table 3.1, our proposed frequency divider shows the comparable performance while it consumes the zero static power consumption.
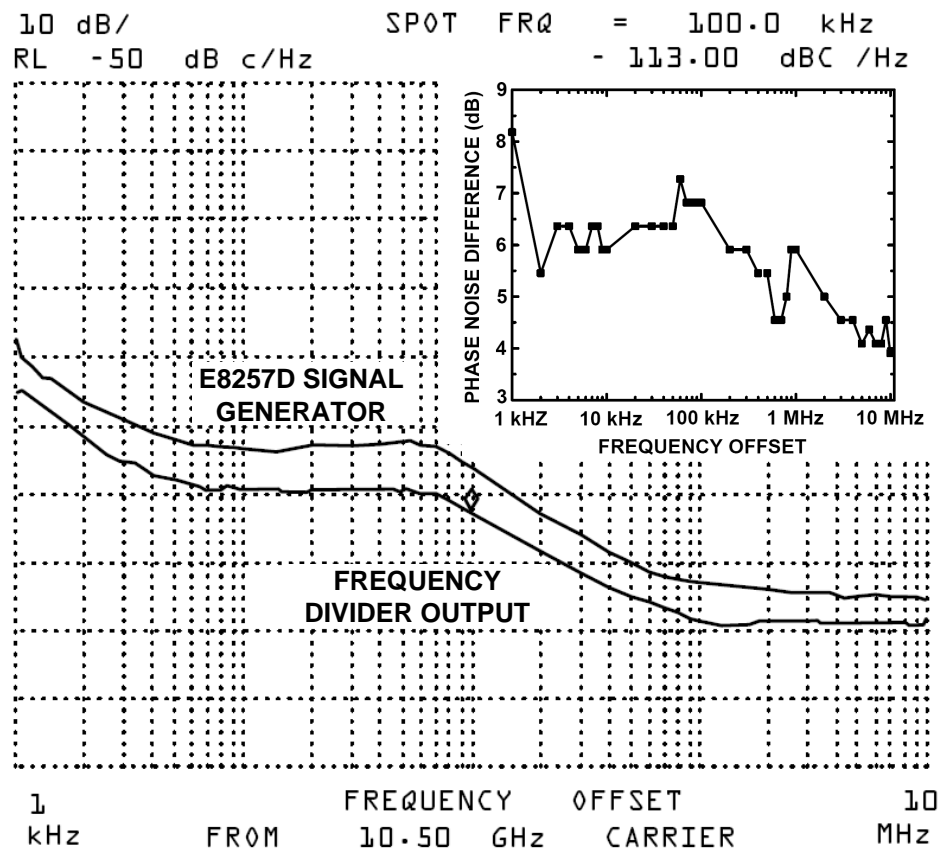
Figure 3.13: Measured phase noise for signal generator and frequency divider output

3.5 Discussion

In this section, we provide comparisons between the proposed frequency divider and a digital frequency divider with no static power consumption in terms of the operation speed. Additionally, we discuss the application of the proposed frequency divider in a phase locked loop (PLL) and its advantages over other types of the frequency dividers. We also discuss the possibility of extending the proposed concept to design a divide-by-4 frequency divider.

Table 3.1: Comparison with prior art

	Frequency (GHz)	P_{DC} (mW)	Operation Range (%)	P_{inj} (dBm)	Chip Area(mm^2)	Technology (CMOS)
[34]	20.8-22.6	0.39	8.3	3	0.27	0.18-μm CMOS
[35]	19.5-22	6.4*	18.1	4	0.03	90-nm CMOS
[36]	19.3-23.4	1.5	19.5	10	0.23	0.13-μm CMOS
[37]	20.5-26	1.5	23.6	0	0.22	0.18-μm CMOS
This work	**20-21.5**	**0**	**7.2**	**8.6**	**0.26**	**0.13-μm CMOS**

P_{DC} only includes the core power consumption. * includes the power for quadrature generation.

3.5.1 Comparison with Digital Frequency Dividers

Digital frequency dividers can be also implemented using dynamic latches to achieve no static power consumption. However, the dynamic latch has a long time constant due to the switching resistance, $1/g_{ds}$, and parasitic capacitance of the MOSFET, requiring a rail-to-rail input to minimize the resistance [30]. This is why "current-mode logic" (CML) latches are commonly used for high-frequency frequency division above 10 GHz despite their high power consumption [31]. Therefore, the proposed frequency divider can operate at higher frequencies than a dynamic latch frequency divider although both of them have no static power consumption. In addition, the fan-out capacitance, which comes from the buffer or the next stage, can slow down the digital frequency divider [30]. On the other hand, the proposed structure can absorb the fan-out capacitances to the transmission line structure to increase the operation frequency. However, the digital frequency divider, which does not use the resonator struc-

ture, provides broader operation bandwidth than the proposed structure.

3.5.2 Application in a Phase-Locked Loop

Comparing to Miller frequency dividers and injection-locked frequency dividers, which support a high frequency division, the proposed frequency divider has simpler structure with no static power consumption. This is critical since the overall power consumption of a PLL is dominated by the first few dividers above 10 GHz [1]. Moreover, the absence of active devices alleviates the phase noise contribution in a PLL, caused by the flicker noise and white noise floor [32].

The distributed structure of the proposed frequency divider is also advantageous for its use in a PLL to cover a large area of clock distribution network. Wiring differential transmission lines in a clock distribution network can be turned into the proposed frequency divider simply by placing the varactors with appropriate spacing and by connecting both ends. However, the narrow input bandwidth for a fixed varactor bias should be improved for reliable operation while the proposed frequency divider can be still useful as one of the first few frequency dividers in a PLL [33].

3.5.3 Extension to Divide-by-4 Frequency Divider

A divide-by-4 frequency division can be achieved simply by opening one end of the resonator as shown in Fig. 3.14. The open end does not change the pump standing wave formation. However, it only allows $\lambda_s/4$ and $3\lambda_s/4$ modes for the
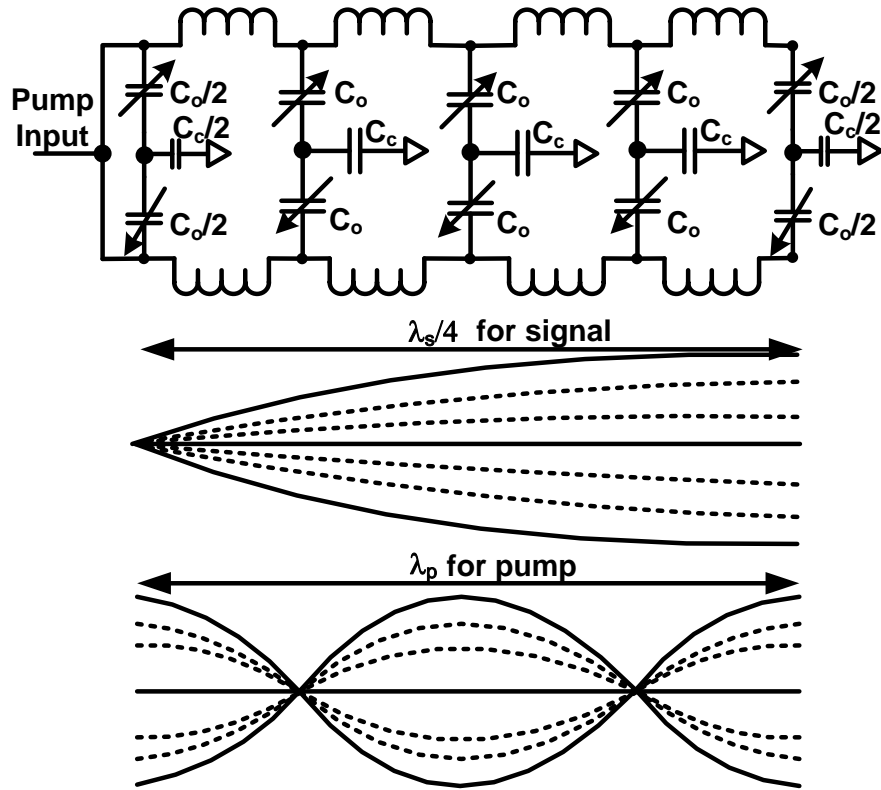
Figure 3.14: Extension to a divide-by-4 frequency divider

signal, not $\lambda_s/2$ (higher modes than $3\lambda_s/4$ are suppressed by cut-off frequency of the resonator). Therefore, $1/4\omega_p$ and $3/4\omega_p$ are generated by the parametric oscillation. Since the input frequency is not twice of the generated frequencies, parametric amplification process is no longer degenerate. The non-degenerate parametric gain is smaller than the degenerate case especially for small number of sections, resulting in a higher threshold than a divide-by-2 frequency divider.

3.6   Conclusion

We propose the first passive CMOS frequency divider based on the parametric amplification process using a reflective distributed resonator. The input signal injected into the resonator transfers the energy into a divide-by-2 frequency component through degenerate parametric amplification. By traveling back and forth in the resonator, the signal grows and finally achieves the steady state oscillation at a divide-by-2 frequency. Not having any active devices to sustain oscillation has two important advantages: no static power consumption and low phase noise. Furthermore, the reflective distributed resonator forms different standing waves for signal and pump, which is exploited to suppress the pump at the output as well as to increase the signal amplitude. Finally, the proposed divider occupies more chip area compared to the conventional designs unless it is implemented as part of the clock distribution network.

BIBLIOGRAPHY

[1] A.M. Niknejad and H. Hashemi, *mm-Wave Silicon Technology: 60 GHz and Beyond*, Springer, 2008.

[2] S. Rong, A.W. Ng, and H.C. Luong, "0.9mW 7GHz and 1.6mW 60GHz Frequency Dividers with Locking-Range Enhancement in 0.13um CMOS," in *IEEE ISSCC Dig. Tech. Papers*, Feb. 2009, pp. 96-97.

[3] K.H. Tsai, L.C. Cho, J.H. Wu, and S.I. Lu, "3.5mW W-Band Frequency Divider with Wide Locking Range in 90nm CMOS Technology," in *IEEE ISSCC Dig. Tech. Papers*, Feb. 2008, pp. 466-467.

[4] Q. Gu, Z. Xu, D. Huang,et al., "A Low Power V-Band CMOS Frequency Divider With Wide Locking Range and Accurate Quadrature Output Phases," *IEEE J. Solid-Stat Circuits*, vol. 43, no. 4, pp. 991-998, Apr. 2008.

[5] H.R. Rategh and T.H. Lee, "Superharmonic Injection-Locked Frequency Dividers," *IEEE J. Solid-Stat Circuits*, vol. 34, no. 6, pp. 813-821, Jun. 1999.

[6] S. Verma, H.R. Rategh ,and T.H. Lee, "A Unified Model for Injection-Locked Frequency Dividers," *IEEE J. Solid-Stat Circuits*, vol. 38, no. 6, pp. 1015-1027, June. 2003.

[7] B. Razavi, "A Study of Injection Locking and Pulling in Oscillators," *IEEE J. Solid-Stat Circuits*, vol. 39, no. 9, pp. 1415-1424, Sep. 2004.

[8] B. Razavi, "Heterodyne Phase Locking: A Technique for High-Speed Frequency Division," *IEEE J. Solid-Stat Circuits*, vol. 42, no. 12, pp. 2887-2892, Dec. 2007.

[9] W.H. Louisell, *Coupled mode and Parametric electronics*, Wiley, New York, NY, 1960.

[10] R. Landauer, "Parametric Amplification Along Nonlinear Transmission Lines," *Journal of Applied Physics*, vol. 31, pp. 479-484, 1960.

[11] G. R. Sloan, "The Modeling, Analysis, and Design of Filter-Based Parametric Frequency Dividers," *IEEE Trans. MTT*, vol. 55, no. 10, pp. 224-228, Feb. 1993.

[12] A. Suarez and R. Melville, "Simulation-Assisted Design and Analysis of Varactor-Based Frequency Multipliers and Dividers," *IEEE Trans. MTT*, vol. 54, no. 3, pp. 1166-1179, Mar. 2006.

[13] Z. Heshmati, I.C. Hunter, and R.D. Pollard, "Microwave Parametric Frequency Dividers With Conversion Gain," *IEEE Trans. MTT*, vol. 41, no. 2, pp. 2059-2064, Oct. 2007.

[14] A. Yariv, W.H. Louisell, "Theory of the Optical Parametric Oscillator," *IEEE J. of Quantum Electronics*, vol. QE-2, no. 9, pp. 418-424, Sep. 1966.

[15] S.E. Harris, "Tunable Optical Parametric Oscillators," *Proc. IEEE*, vol. 57, no. 12, Dec. 1969.

[16] P.K. Tien and H. Suhl, "A Traveling-wave Ferromagnetic Amplifier," *Proc. IRE*, vol. 46, pp. 700-706, April 1958.

[17] P.K. Tien, "Parametric Amplification and Frequency Mixing in Propagating circuits," *Journal of Applied Physics*, vol. 29, no. 9, pp. 1347-1357, Sep. 1958.

[18] *CMRF8SF Model Reference Guide*, IBM Microelectronics Division, Apr. 2007.

[19] L.E. Myers, R.C. Eckardt, M.M. Fejer, and R.L. Byer, "Quasi-Phase-Matched Optical Parametric Oscillators in Bulk Periodically Poled *LiNbO$_3$*," *J. Opt. Soc. Am. B*, vol. 12, no. 11, pp. 2102-2116, Nov. 1995.

[20] D.M. Pozar, *Microwave Engineering*, Wiley, New York, NY, 2005.

[21] G.M. Roe and M.R. Boyd, "Parametric Energy Conversion in Distributed Systems," *Proc. IRE*, vol. 47, pp. 1213-1218, July 1959.

[22] D. Ham and A. Hajimiri, "Concepts and Methods in Optimization of Integrated LC VCOs," *IEEE J. Solid-Stat Circuits*, vol. 36, no. 6, pp. 896-909, Jun. 2001.

[23] H. Brauns and W.Konrath, "Ultra Low Phase Noise Parametric Frequency Divider For Highest Performance Microwave-and Milimeter-wave Frequency Sources,"in *European Microwave Conference*, vol. 2, pp. 1155-1158, Oct. 1995.

[24] S.H. Strogatz, *Nonlinear Dynamics and Chaos*, Perseus Books, Massachusetts, 1994.

[25] U.L. Rohde, *Microwave and Wireless Synthesizers. Theory and Design*, Wiley, New York, NY, 1997.

[26] Chien-Chih Ho, et al, "0.13-um RF CMOS and Varactors Performance Optimization by Multiple Gate Layouts," *IEEE Tran. Electron Devices*, vol. 51, no. 12, 2004.

[27] W. F. Andress and D. Ham, "Standing Wave Oscillators Utilizing Wave-Adaptive Tapered Transmission Lines," *IEEE J. Solid-Stat Circuits*, vol. 40, no. 3, pp. 638-651, March. 2005.

[28] S. A. Wartenberg and J. R. Hauser, "Substrate Voltage and Accumulation-Mode MOS Varactor Capacitance," *IEEE Trans. Electron Devices*, vol. 52, no. 7, pp. 1563-1567, July. 2005.

[29] T. Luo, Y. E. Chen, "A 0.8-mW 55-GHz Dual-Injection-Locked CMOS Frequency Divider," *IEEE Trans. MTT*, vol. 56, no. 3, pp. 620-625, March. 2008.

[30] B. Razavi, *Design of Integrated Circuits for Optical Communications*, McGRAW-HILL, New York, NY, 2003.

[31] B. Kim and L. Kim, S. Byun, and H. Yu, "A 20 Gb/s 1:4 DEMUX Without Inductors and Low-Power Divide-by-2 Circuit in 0.13 μm CMOS Technology," *IEEE J. Solid-Stat Circuits*, vol. 43, no. 2, pp. 541-549, Jun. 2001.

[32] A. Hajimiri, "Noise in Phase-Locked Loops," *Proc. of IEEE Southwest Symposium on Mixed-Signal Circuits*, pp. 1-6, Feb. 2001.

[33] J. Lee and M. Liu, and H. Wang, "A 75-GHz Phase-Locked Loop in 90-nm CMOS Technology," *IEEE J. Solid-Stat Circuits*, vol. 43, no. 6, pp. 1414-1426, Jun. 2008.

[34] C. Chen and C. C. Tzuang, "A Sub-1V 22-GHz CMOS Injection-Locked Frequency Divider," in *European Microwave Integrated Circuits Conference*, pp. 68-70, Oct. 2008.

[35] T. Shibasaki, H. Tamura, K. Kanda, H. Yamaguchi, J. Ogawa, adn T. Kuroda, "20-GHz Quadrature Injection-Locked LC Dividers With Enhanced Locking Range," *IEEE J. Solid-Stat Circuits*, vol. 43, no. 3, pp. 610-618, March. 2008.

[36] Z. Huang, C. Wu, and B. Huang, "Design of 24-GHz 0.8-V 1.51-mW Coupling Current-Mode Injection-Locked Frequency Divider With Wide Locking Range," *IEEE Trans. MTT*, vol. 57, no. 8, pp. 1948-1958, Aug. 2009.

[37] Y. Kuo, J. Tsai, T. Huang, "A 1.5-mW, 23.6 % Frequency Locking Range, 24-GHz Injection-Locked Frequency Divider,"in *European Microwave Conference*, pp. 73-76, Sep. 2010.

LOW NOISE PARAMETRIC RESONANT AMPLIFIER WITH NOISE SQUEEZING

4.1 Introduction

In an RF receiver front end, a low noise amplifier (LNA) is a critical block since it mainly determines the noise figure (NF) of the entire system. There have been many previous efforts to minimize the NF of LNAs in a CMOS process. A source-degenerated CMOS LNA is one of the most prevalent structures, which achieves input matching without a real resistor and exploits an input resonant network for signal amplification [1, 2]. A g_m−boosted LNA and positive feedback LNA are also attractive modifications of a conventional common-gate CMOS LNA [3, 4]. A sub-0.2-dB NF CMOS LNA was implemented with a non-50 Ω signal-source impedance [5].

A more exotic approach is to use parametric amplification, in which the gain comes from nonlinear interaction between signal and pump without using transistors. Parametric amplification was actively studied in the 1960s before the transistor technology dominated the integrated circuit design [6]. However, the parametric amplification cannot provide enough gain for high frequency signals due to low quality factors of inductors and capacitors on a CMOS process.

In this chapter, we propose a parametric amplifier based on a distributed nonlinear resonator to overcome the limitation of low quality factor elements. The distributed nonlinear resonator operates as a regenerative amplifier by supplying the pump amplitude below the oscillation threshold. As a result, the am-

plifier achieves a high close-loop gain using a less-than-unity open-loop gain [7]. An important property of the proposed amplifier is its phase-sensitive gain, resulting in *noise squeezing*. One of the quadrature input noise components, e.g., out-of-phase, is suppressed when the input noise consists of two quadrature components: in-phase and out-of-phase relative to the pump signal. This noise squeezing reduces the amplifier output noise by almost 3 dB compared to the phase-insensitive amplifier with the same gain. In other words, while a conventional amplifier increases the input noise of both quadratures, the noise-squeezing amplifier increases the noise of one quadrature and, at the same time, decreases the other one.

The noise squeezing was originally studied in optics for precise measurements constrained by the *uncertainty principle*, which sets a fundamental limit to the simultaneous observation of two conjugate parameters, such as the photon number and its phase [8,9]. Since the uncertainty principle preserves the multiplication of the variances of two conjugate parameters, the degenerate parametric amplifier can suppress one of the quadrature noise components at the expense of amplifying the other quadrature component through phase-sensitive amplification. The noise squeezing was also demonstrated in the mechanical systems as classical analogues of optical systems to beat the thermal noise limitation [10,11]. Finally, Josephson's parametric amplifier using a superconducting quantum interference device (SQUID) was designed to implement noise squeezing in an electrical system [12–14]. However, this amplifier requires a very low operation temperature (around 0 K) and is not integrable. To the best of our knowledge, our work is the first demonstration of noise squeezing for a low-noise amplifier in a CMOS process.

The rest of the chapter is organized as follows. Section 4.2 discusses the noise squeezing effect to enhance the noise performance. Section 4.2.2 explains the pump loss effect, which poses fundamental limits for gain and noise squeezing in a traveling parametric amplifier. Section 4.3 proposes a resonant parametric amplifier to overcome the limits mentioned in section 4.2.2 and analyzes its phase-sensitive gain and noise squeezing performance. Section 4.4 summarizes the design procedure and the simulation results. Finally, section 4.5 discusses the measurement results.

4.2   Noise of a Degenerate Parametric Amplifier

4.2.1   Theoretical Analysis

Since degenerate parametric process uses only reactive components, potentially it can achieve a better noise figure (NF) than the conventional transistor-based amplifiers. In addition, its phase-sensitive gain shows an interesting property: *noise squeezing*. The equi-partition theorem suggests that the input noise, usually thermal noise, is circularly symmetric for two quadrature components in a thermal equilibrium and can be written as a narrow-band representation for carrier (signal) frequency, ω [19] [20]:

$$n(t) = n_I(t) \cos \omega t + n_Q(t) \sin \omega t \tag{4.1}$$

$$\overline{n_I^2(t)} = \overline{n_Q^2(t)} \cong \sigma^2 \tag{4.2}$$

where $n_I(t)$ and $n_Q(t)$ are slowly varying functions compared to a sinusoidal function at ω.

When $n(t)$ is injected into a degenerate parametric amplifier with k-section lossless nonlinear transmission line ($\widetilde{\alpha}_s = 0$) pumped at 2ω and the pump has the right phase so that $n_I(t)$ experiences the maximum gain, then $n_Q(t)$ has the maximum attenuation based on (2.23):

$$\overline{n_I^2(t)_{out}} = |G_{k,\phi=-\pi/4}|^2 \overline{n_I^2(t)} = F_k \sigma^2 \tag{4.3}$$

$$\overline{n_Q^2(t)_{out}} = |G_{k,\phi=\pi/4}|^2 \overline{n_Q^2(t)} = \frac{1}{F_k} \sigma^2 \tag{4.4}$$

where in-phase power gain for k-section lossless NLTL, F_k, is defined as:

$$F_k = e^{2\widetilde{s_0}k}. \tag{4.5}$$

The multiplication of the standard deviations of $n_I(t)_{out}$ and $n_Q(t)_{out}$ is given by:

$$\sqrt{\overline{n_I^2(t)}_{out}} \cdot \sqrt{\overline{n_Q^2(t)}_{out}} = \sqrt{F_k}\sigma \cdot \frac{1}{\sqrt{F_k}}\sigma = \sigma^2 \tag{4.6}$$

$$= \sqrt{\overline{n_I^2(t)}} \cdot \sqrt{\overline{n_Q^2(t)}}. \tag{4.7}$$

Eq. (4.7) shows that the multiplication of two quadrature noise components is preserved since one quadrature noise component (out-of-phase) is suppressed at the expense of amplifying the other quadrature noise component (in-phase) through phase-sensitive amplification.

Here we introduce a noise squeezing factor, S_F, which is equal to NF when the information is placed only in the single quadrature phase. This needs to be differentiated with the general NF, which usually considers information in two quadrature phases. Assuming that thermal noise caused by power dissipation on the transmission line is negligible and that the signal information is only in

the in-phase direction, the noise squeezing factor of the parametric amplifier is defined as:

$$S_F = \frac{SNR_{IN}}{SNR_{OUT}} = \frac{\frac{v_s^2}{n_I^2+n_Q^2}}{\frac{F_k v_s^2}{F_k n_I^2 + 1/F_k n_Q^2}} = \frac{1}{2}\left(1 + \frac{1}{F_k^2}\right) \tag{4.8}$$

where $n_I^2 = n_Q^2 \cong \sigma^2$ and v_s is a signal amplitude.

Eq. (4.8) shows that the squeezing factor approaches -3 dB as F_k increases. In other words, the noise is redistributed from a circular to an oval shape through parametric amplification to have a higher SNR in one quadrature direction. Fig. 4.1 shows the time-domain effect of the noise squeezing and the noise distribution over the phase. The output of the parametric amplifier can be written as:

$$v_{out}(t) = \sqrt{F_k}v_s(t)\cos(\omega t - \theta) + n_{out}(t) \tag{4.9}$$

$$= \sqrt{F_k}[v_s(t) + n_I(t)]\cos(\omega t - \theta - \zeta) \tag{4.10}$$

where

$$\zeta = \tan^{-1}\left(\frac{n_Q(t)}{F_k v_s}\right) \cong \frac{n_Q(t)}{F_k v_s} \tag{4.11}$$

and θ is the phase shift due to propagation delay over the transmission line. Eq. (4.10) shows that $n_I(t)$ contributes to the amplitude fluctuation whereas $n_Q(t)$ contributes to the phase fluctuation. Eqs. (4.10) and (4.11) explain how the squeezing suppresses the phase (timing) fluctuation at the output by increasing the amplitude fluctuation with the same ratio as shown in Fig. 4.1(c). This is fundamentally different from a linear amplifier (phase insensitive amplifier) that provides the same amount of amplification for two quadrature components, resulting in a circularly symmetric output noise distribution as shown in Fig. 4.1(b).
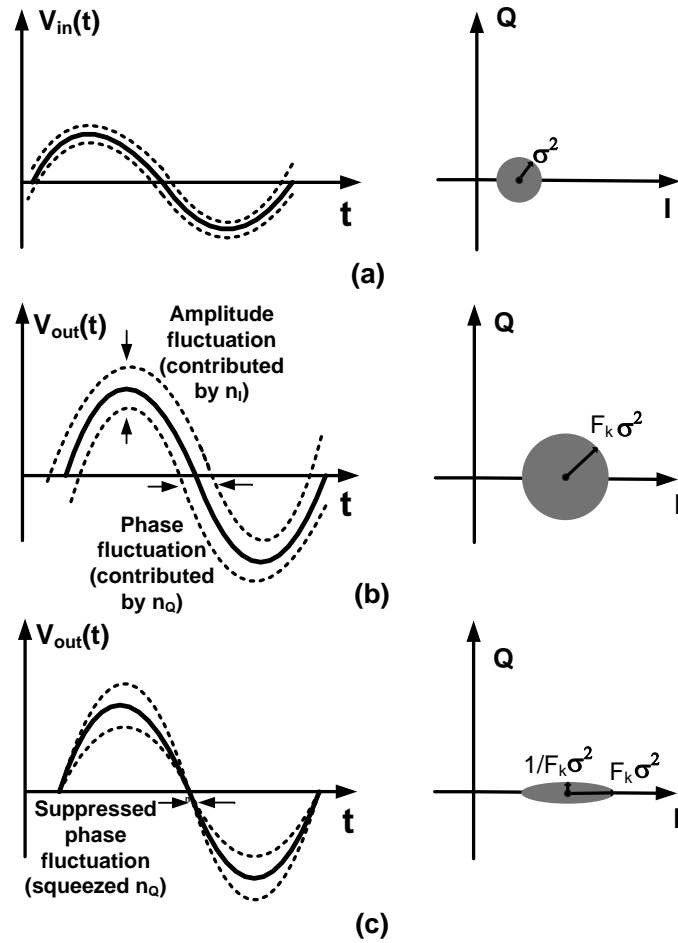
Figure 4.1: Observation of squeezed output noise by phase-sensitive amplification in a time and phase domain compared to linear amplification: (a) input signal, (b) output signal through linear amplification, and (c) output signal through phase-sensitive amplification. To simplify the notations, the phase of the pump is shifted by $\pi/2$. In (2.23) the signal has its maximum and minimum at $\phi = 0$ and $\phi = \pi/2$, respectively.
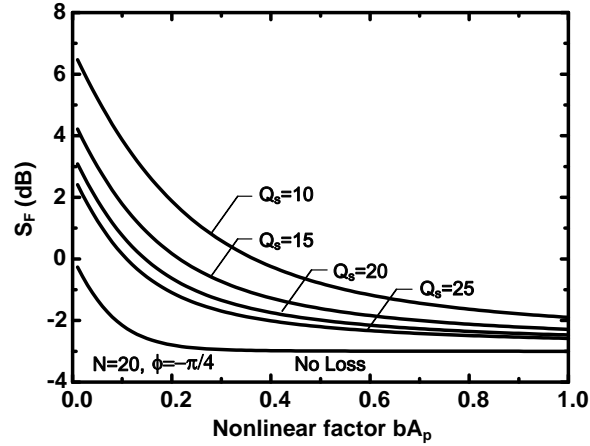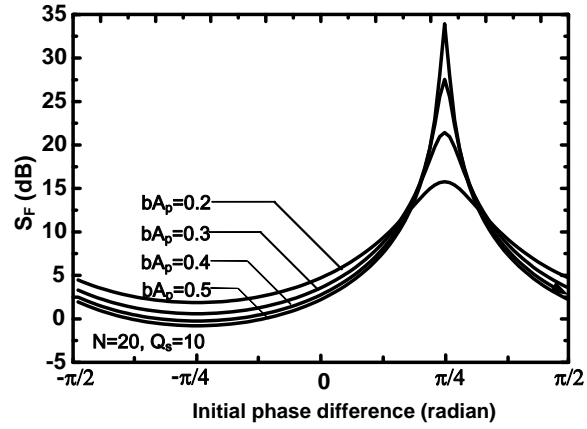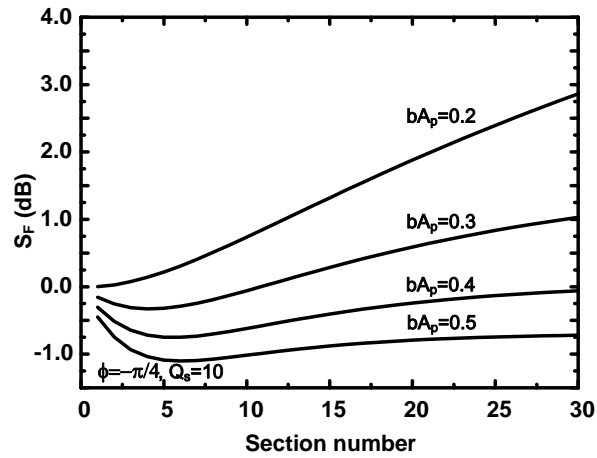
Figure 4.2: Calculated squeezing factor versus (a) nonlinear factor for different transmission line loss, (b) initial phase difference between pump and signal for different nonlinear factors, and (c) section number for different nonlinear factors (l=630 pH, c_0=250 fF, ω=10 GHz).

Next, we take into account the effect of transmission line loss in the parametric amplifier squeezing factor, S_F. The parametric amplifier consists of two transmission lines that generate two independent noises, v_{n1i} and v_{n2i}, at the ith node. Because only the differential signal is amplified, the output noise contributed by the power dissipation at the ith node is:

$$\overline{v_{nout}^2}|_i = \frac{e^{-2\widetilde{\alpha}_s(k-i)}}{2}\left(F_{k-i} + \frac{1}{F_{k-i}}\right)(\overline{v_{n1i}^2} + \overline{v_{n2i}^2}) \tag{4.12}$$

$$= 2e^{-2\widetilde{\alpha}_s(k-i)}\cosh[2\widetilde{s}_0(k-i)]\overline{v_{n1i}^2} \tag{4.13}$$

The thermal noise power generated at the ith node that travels toward output is:

$$\overline{v_{n1i}^2} = kTBr + kTBgZ_0^2 \tag{4.14}$$

$$= 2kTBZ_0\left(\frac{r}{2Z_0} + \frac{gZ_0}{2}\right) = 2kTBZ_0\widetilde{\alpha}_s \tag{4.15}$$

where B is the bandwidth over which the noise is measured. r and g are parasitic series resistance and parallel conductance which represent inductor and varactor loss, respectively. Combining (4.13) and (4.15), the total output noise associated with transmission line loss is given by:

$$\overline{v_{nout}^2} = 4kTBZ_0\widetilde{\alpha}_s \sum_{i=1}^{k} e^{-2\widetilde{\alpha}_s i}\cosh(2\widetilde{s}_0 i). \tag{4.16}$$

From (4.8) and (4.16), the noise squeezing factor becomes:

$$S_F = \frac{1}{2}\left(1 + \frac{1}{F_k^2}\right) + \frac{2\widetilde{\alpha}_s}{F_k}\sum_{i=1}^{k} e^{2\widetilde{\alpha}_s(k-i)}\cosh(2\widetilde{s}_0 i) \tag{4.17}$$

where the input signal source impedance is matched with the characteristic impedance, Z_0. In the absence of the pump ($F_k = 1$), from (4.17) the noise figure, or the squeezing factor, is simply approximated with $e^{2\widetilde{\alpha}_s k}$, which is the reciprocal of transmission line loss and is expected from a conventional transmission line.

Fig. 4.2 shows the calculated squeezing factor based on (4.17). The signal and pump frequencies are 10 GHz and 20 GHz, respectively. The cut-off frequency is set to be 25 GHz. When the transmission line is lossless, the amplifier squeezing factor approaches -3 dB for large nonlinear factors as shown in Fig. 4.2(a). However, the transmission line loss significantly degrades the squeezing factor. The phase sensitivity of the squeezing factor is also investigated, as shown in Fig. 4.2(b). Since the input noise distribution is assumed to be circularly symmetric and independent of input signal, the variation of the squeezing factor is caused only by change in the signal gain. The squeezing factor is also calculated as a function of the section number, as shown in Fig. 4.2(c). As the section number increases, the squeezing effect exponentially increases, resulting in a better squeezing factor. However, in the presence of transmission loss, the number of noise sources also increases with section number. Therefore, for a given nonlinearity, an optimum number of sections will result in a minimum squeezing factor.

4.2.2 Pump Loss Effect

The previous sections examined the signal gain and noise performance in the absence of pump attenuation for an analytical solution. However, pump loss is critical since the signal gain is an exponential function of the pump amplitude, as shown in (2.23).

Fig. 4.3 shows the simulated pump loss effect on the gain and squeezing factor based on (2.15) and (2.16) when the phase difference between signal and pump is $-\pi/4$ for a maximum gain. When pump loss is negligible, the log-scale
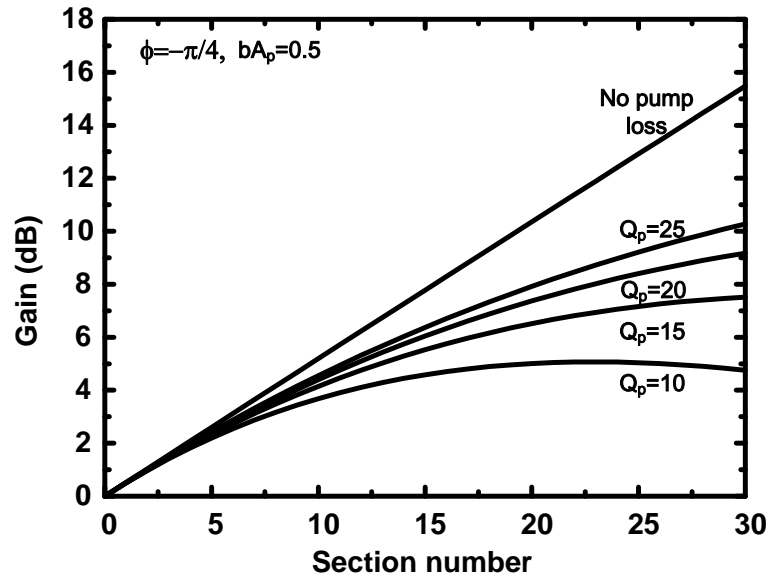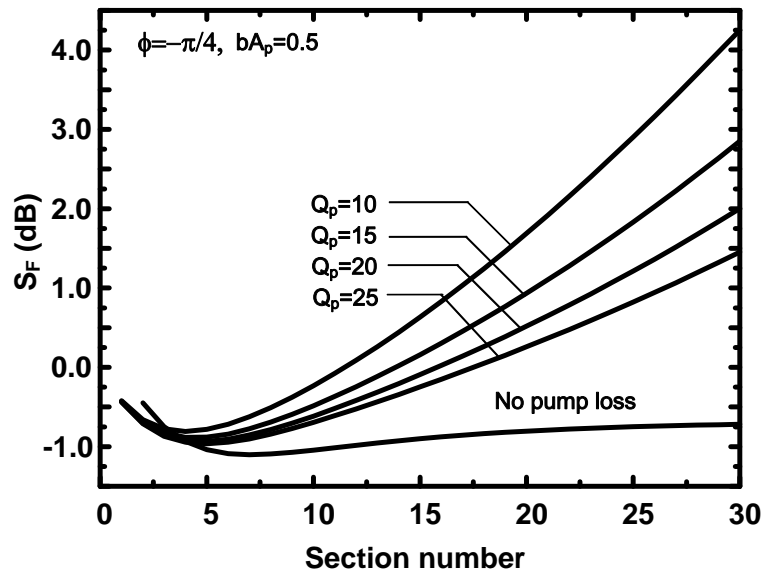
Figure 4.3: Simulated pump loss effect on (a) gain and (b) squeezing factor versus section number for different pump losses (l=630 pH, c_0=250 fF, Q_s=10, ω=10 GHz).

gain is linearly proportional to the section number following (2.23). However, as the pump loss increases, the amplifier gain reaches a peak for a certain number of sections. Before this point, since the pump amplitude is large, the gain increases as the signal propagates. After this point, the pump amplitude is too low to compensate the loss of the transmission line, resulting in a lower gain. For a higher pump loss, this optimal number of sections also decreases, thereby resulting in lower gain peak. Considering that the typical value of the quality factor of the transmission line is around 10 for a pump frequency of 20 GHz, the maximum gain is only 5 dB with 22 sections. One might consider injecting pump frequency at multiple points of the transmission line to compensate the loss. Unfortunately, this method would require higher pump power and also results in a more complex design and higher footprint.

Pump loss also degrades squeezing factor: loss results in pump attenuation which ,in turn, translates to a lower squeezing effect. This is shown in Fig.4.3(b) where the squeezing factor increases with the section number.

4.3   Resonant Parametric Amplifier

To overcome the challenges of traveling-wave structures associated with a large number of lumped LC elements and pump loss due to limited quality factor, we propose a resonant regenerative amplifier based on a parametric oscillator structure.
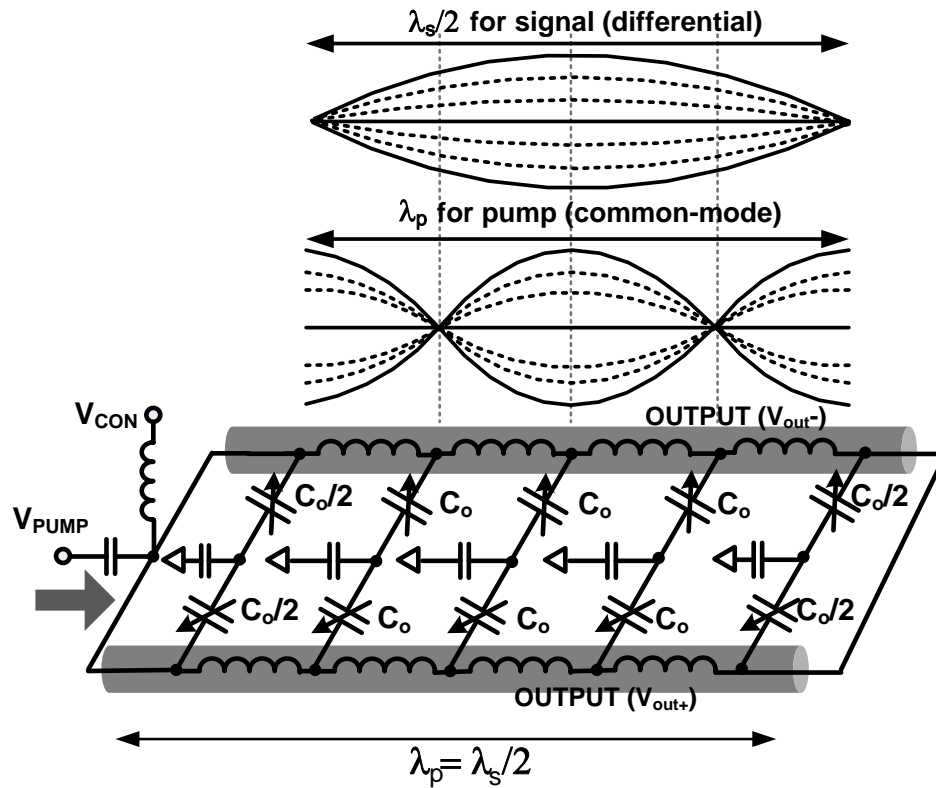
Figure 4.4: Reflective distributed parametric oscillator and its standing wave formation for signal and pump frequencies.

4.3.1 Review of Reflective Parametric Oscillator

Fig. 4.4 shows the reflective parametric oscillator and its standing wave formation for signal and pump frequencies. Parametric oscillation occurs when the parametric amplification compensates the loss of a resonator at the resonance frequency. The resonator consists of two transmission lines with four phase-matched LC sections that are connected at both ends. Oscillation starts from the ambient thermal noise of the resonator when the pump is strong enough to compensate for the loss. The noise component grows by traveling back and forth between two reflective ends through the degenerate parametric amplification, finally generating a stable oscillation signal at a half-pump frequency.
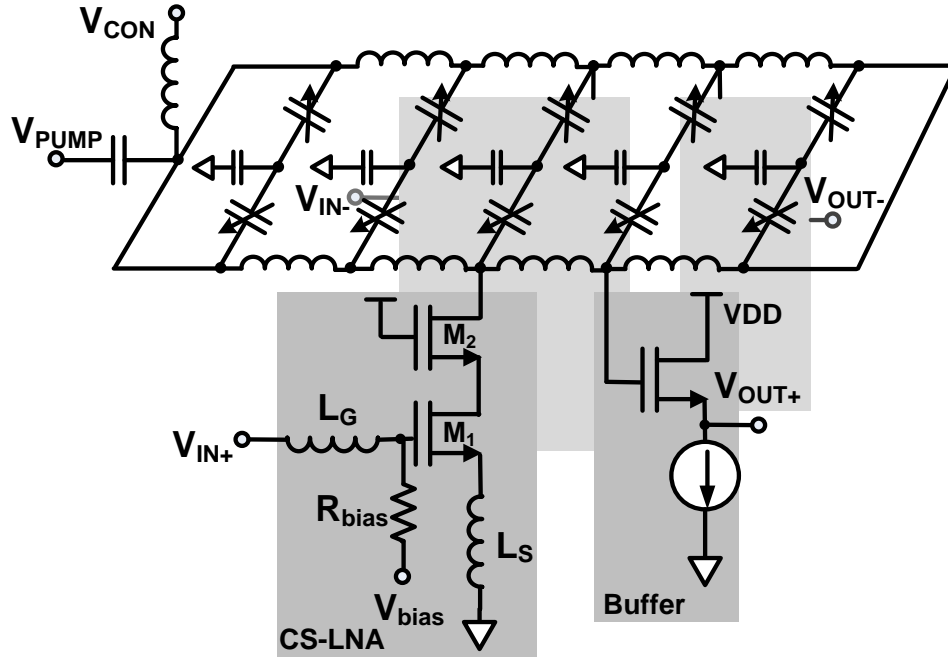
Figure 4.5: Differential parametric resonant amplifier with output buffer.

The upper part of Fig. 4.4 shows different standing wave formations inside the resonator for both pump and signal. The differential signal sees the resonator ends as shorts due to the virtual ground, while the common-mode pump sees the ends as open nodes. The effective length of the four-LC-section resonator is equal to a pump wavelength, λ_p, which is half of the signal wavelength, λ_s. With the reflection at both ends, the signal forms a $\lambda_s/2$ standing wave with minimum amplitudes at the two boundaries. On the other hand, the pump forms a λ_p standing wave with maximum amplitudes at both ends. The higher modes for pump and signal are suppressed by the resonator cutoff frequency. The output port is selected at "$3/4\lambda_p$" location to suppress the pump signal by exploiting the different standing wave formations for signal and pump.

4.3.2   Regenerative Amplifier with Parametric Resonator

By operating the parametric oscillator with a pump below the oscillation threshold, another form of degenerate parametric amplification can be achieved, as shown in Fig. 4.5. Based on the resonator structure in Fig. 4.4, the input signal is applied to the middle of the resonator through the drain of a common source low noise amplifier. The source followers are simply used as output buffers to drive a 50 Ω output load. The control voltage, V_{con}, enables to tune the resonant frequency.

For theoretical analysis, we consider the coupled-mode equations of (2.15) and (2.16). Adding terms that represent the injection of the input signal and pump into the resonator, these coupled-mode equations are modified to:

$$\frac{\partial A}{\partial x} = -\frac{j\beta b A_p}{4}A^* - \alpha_s A + \kappa_s \frac{A_s}{2}e^{j\phi} \tag{4.18}$$

$$\frac{\partial A^*}{\partial x} = \frac{j\beta b A_p}{4}A - \alpha_s A^* + \kappa_s \frac{A_s}{2}e^{-j\phi} \tag{4.19}$$

$$\frac{\partial A_p}{\partial x} = -\alpha_p A_p + \kappa_p A_{pin}, \tag{4.20}$$

where κ_s and κ_p represent the increase ratios in the signal and pump amplitude inside the resonator due to the injected signal and pump, respectively. The significance of this term will be seen when reflections are taken into account inside the resonator, which will be presented in (4.24) and (4.25). A_s and A_{pin} are the signal and pump amplitudes that enter the resonator, respectively.

By the structural symmetry of the resonator, we can only consider the left-half of the resonator for the following analysis. It is noteworthy that even though the pump is only applied to the left end of the resonator, for our analysis we can imagine a virtual pump injection from the right end. This is due to the fact that the resonator length is λ_p, which means the two ends are in phase for

the pump frequency.

For steady state response, $\partial A/\partial x, \partial A^*/\partial x, \partial A_p/\partial x = 0$. Combining (4.18) and (4.19) to eliminate A^*, the signal amplitude on the resonator, $|A|$, becomes:

$$|A| = \frac{\kappa_s A_s}{2(\alpha_s^2 - s_0^2)} \sqrt{s_0^2 + \alpha_s^2 - 2s_0\alpha_s \sin 2\phi}, \tag{4.21}$$

where

$$s_0 = \frac{\beta b A_p}{4} = \frac{\beta b \kappa_p}{4\alpha_p} A_{pin}. \tag{4.22}$$

At the resonator end where the pump is injected, the relation between m^{th} and $(m + 1)^{th}$ round-tripped pump amplitudes, A_{p_m} and $A_{p_{m+1}}$, is:

$$A_{p_{m+1}} = A_{p_m} \exp(-2\alpha_p d) + A_{pin} \tag{4.23}$$

where $2d$ is the round-trip length of the resonator. Inserting $A_{p_{m+1}}=A_{p_m}=A_p|_{steady}$ and $A_p|_{steady} = \kappa_p A_{pin}/\alpha_p$ into (4.23), κ_p is reduced to:

$$\kappa_p = \frac{\alpha_p}{(1 - \exp(-2\alpha_p d))}. \tag{4.24}$$

In a similar way, κ_s can be obtained as below,

$$\kappa_s = \frac{\alpha_s}{1 - \exp(-\alpha_s d)}. \tag{4.25}$$

By rearranging (4.21),

$$G_\phi = \frac{|A|}{A_s} = \frac{\kappa_s \sqrt{(\frac{A_{pin}}{A_{th}})^2 - 2(\frac{A_{pin}}{A_{th}}) \sin 2\phi + 1}}{2\alpha_s[1 - (A_{pin}/A_{th})^2]} \tag{4.26}$$

where

$$A_{th} = \frac{4\alpha_s\alpha_p}{\beta b \kappa_p} = \frac{2(1 - \exp(-2\alpha_p d))}{Q_p b}. \tag{4.27}$$

From (4.26), when the pump amplitude is below the oscillation threshold, $A_{pin} < A_{th}$, the maximum and minimum gain are:

$$G_\phi = \begin{cases} \frac{\kappa_s}{2\alpha_s}(1 - A_{pin}/A_{th})^{-1} & \text{for } \phi = -\frac{\pi}{4} \text{ (max.)} \\ \frac{\kappa_s}{2\alpha_s}(1 + A_{pin}/A_{th})^{-1} & \text{for } \phi = \frac{\pi}{4} \text{ (min.)} \end{cases} \tag{4.28}$$

Based on (4.28), when the pump power is just below the threshold, the amplifier has the lowest gain (i.e., maximum attenuation for $\phi = \pi/4$), which is half the gain in the absence of the pump. This sets a fundamental limit of a maximum squeezing ratio of 6 dB in the proposed system. Next, we are going to calculate the total gain of the parametric amplifier. The voltage gain of a source-degenerated amplifier that injects the signal into the resonator, shown in Fig. 4.5, is [1]:

$$G_0 = \frac{A_s}{V_{IN}} = \frac{\omega_T Z_0}{2\omega R_s} \tag{4.29}$$

where V_{IN} is the input amplitude, ω_T is the cut-off frequency of M_1, Z_0 is the characteristic impedance of the resonator, R_s is the signal source impedance, and ω is the signal frequency, assuming that the input matching is achieved using a source-degenerated inductor, L_s.

Combining (4.26) and (4.29), the total gain of the parametric resonant amplifier becomes:

$$G_T = \frac{A_s}{V_{IN}} \cdot \frac{|A|}{A_s} \cdot \gamma = G_0 G_\phi \gamma \tag{4.30}$$

$$= G_{T0} \frac{\sqrt{(\frac{A_{pin}}{A_{th}})^2 - 2(\frac{A_{pin}}{A_{th}}) \sin 2\phi + 1}}{[1 - (A_{pin}/A_{th})^2]} \tag{4.31}$$

where γ is the voltage increase ratio due to the standing wave formation, defined by $\gamma = 2|\sin(\beta x)|$ ($\gamma \cong 1.41$ for output taken out at $3/4\lambda_p$) [27]. G_{T0} is the gain without the pump injection defined by $G_{T0} = \kappa_s \gamma G_0 / 2\alpha_s$.

83
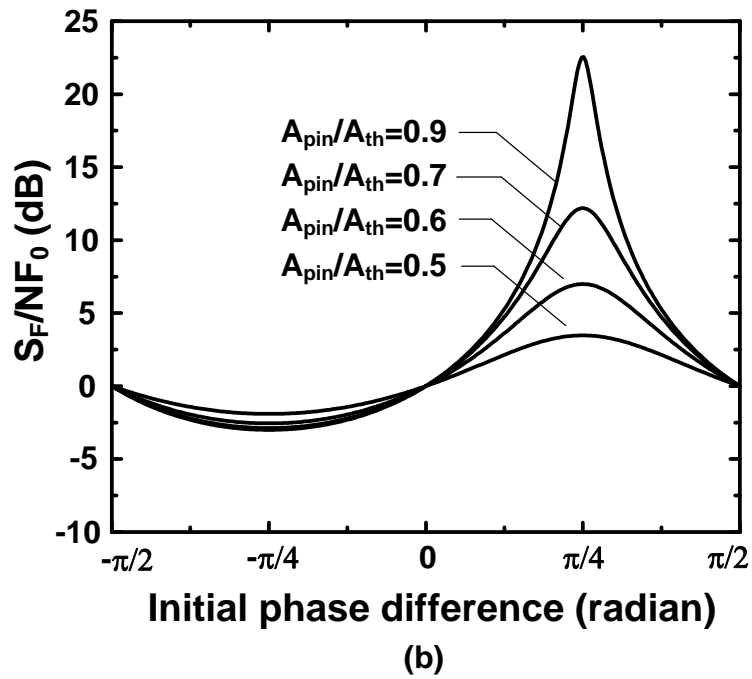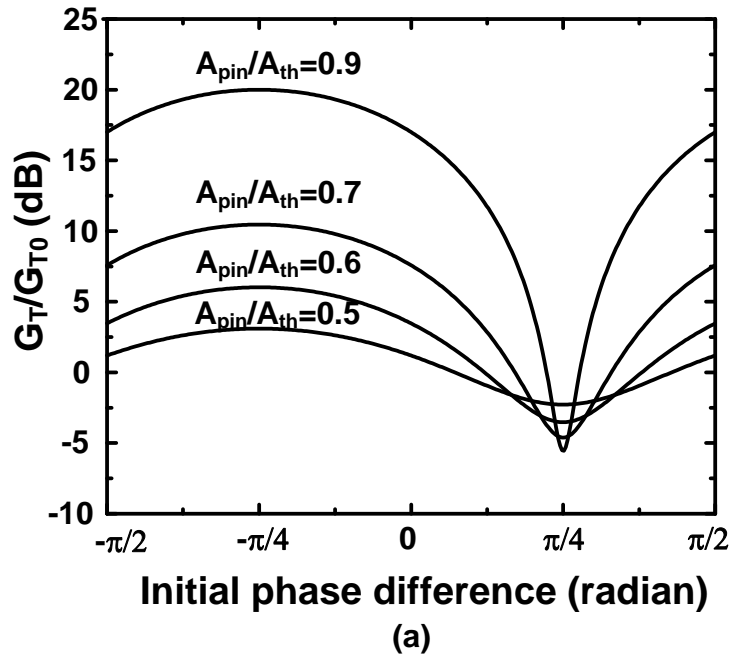
Figure 4.6: Calculated (a) gain enhancement ratio and (b) noise reduction ratio with respect to the phase difference for different pump amplitudes.

Fig. 4.6(a) shows the calculated gain enhancement ratio, G_T/G_{T0}, due to parametric amplification with respect to the phase difference between signal and pump for different pump amplitudes based on (4.31). As the pump amplitude approaches the oscillation threshold, the gain plot shows higher amplification and attenuation depending on the phase difference. The phase difference between the maximum and minimum is $\pi/2$, which clearly shows the phase-sensitive gain for quadrature signals. Fig. 4.6(a) is similar to Fig. 2.7, which is obtained from a traveling-wave type parametric amplifier. However, the resonant amplifier uses only four LC sections and provides much higher gain due to resonance, resulting from the robustness to the pump loss effect compared to Fig. 4.3.

4.3.3 Analogy with a Conventional Regenerative Amplifier

To intuitively understand the parametric amplification on the resonator, we use the analogy with a simplified LC resonant amplifier shown in Fig. 4.7. The inductance and the capacitance in Fig. 4.7(b) are $L_d = 4L_r/\pi$ and $C_d = 4C_{r0}/\pi$, to provide the same resonance frequency as that of the distributed resonator in Fig. 4.5. Here, L_r and C_{r0} are the inductance and average capacitance of each inductor and varactor used in the distributed resonator, respectively. The distributed resonator loss can be modeled as a series resistor r_{ind}, and the parametric amplification can be represented as a negative resistor, $-r(\phi)$, which is a function of the phase difference between the pump and the signal ϕ. The value of the series resistance r_{ind} can be obtained from the quality factor relation

$$Q = \frac{\omega L_d}{r_{ind}} = \frac{\beta}{2\alpha_s} = \frac{\omega \sqrt{L_r C_{r0}}}{2\alpha_s}, \tag{4.32}$$

85

(a)

$$\left|r(\phi_{max})\atop{min}\right| = \frac{bQA_{eff}}{2}\, r_{ind}$$

$$r_{ind} = 8\alpha_s Z_0/\pi$$

$$L_d = 4L_r/\pi$$

$$C_d = 4C_{r0}/\pi$$
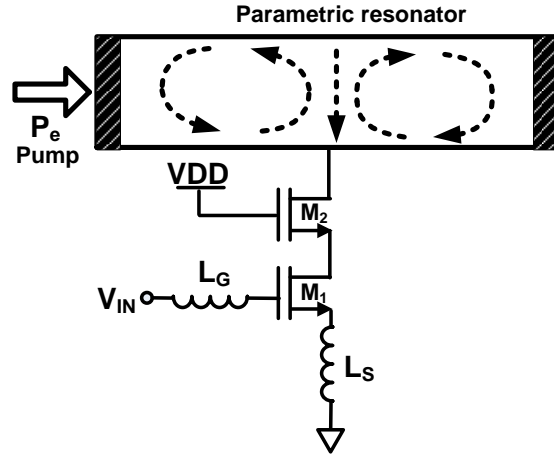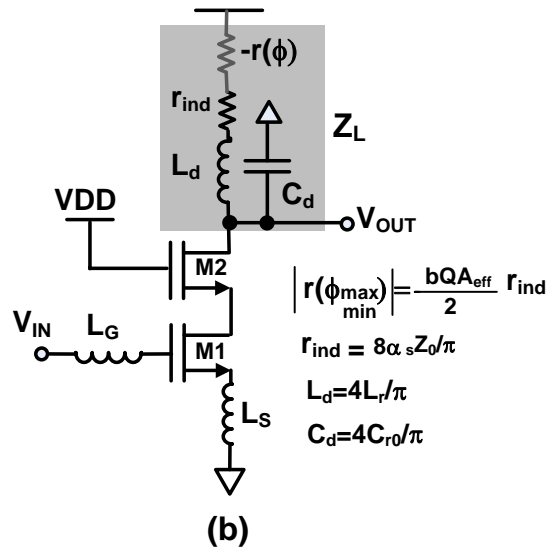
(b)

Figure 4.7: (a) Amplification using a parametric resonator with a pump level below the oscillation threshold (b) A conventional resonant amplifier with a negative resistor.

where α_s is the loss of transmission line per unit length. From (4.32) and $Z_0 = \sqrt{L_r/C_{r0}}$, we can obtain $r_{ind} = 8\alpha_s Z_0/\pi$.

In the absence of pump ($r(\phi) = 0$), the load impedance in Fig. 4.7(b) is $Z_L = Q^2 r_{ind}$. When the pump is applied to the resonator with the right phase with respect to the signal ($\phi = -\pi/4$ in (2.23)), the negative resistor increases the quality factor of the resonator. This provides a larger load impedance around the resonance frequency given by

$$Z'_L = Q'^2 r'_{ind} = \left(\frac{\omega_0 L_d}{r_{ind} - r(\phi)}\right)^2 (r_{ind} - r(\phi)) \tag{4.33}$$

$$= Z_L/(1 - r(\phi)/r_{ind}). \tag{4.34}$$

The increased load impedance results in a higher gain of

$$G = G_m Z'_L = \frac{G_0}{1 - r(\phi)/r_{ind}} \quad \text{for } r(\phi) < r_{ind}, \tag{4.35}$$

where $G_0 = G_m Z_L$ is the gain without the pump and G_m is the effective transconductance. On the other hand, when the phase difference between signal and pump is out of phase, $-r(\phi)$ becomes positive, causing additional signal attenuation due to the parametric process. In other words, the signal phase determines the polarity and magnitude of $r(\phi)$ and changes the amplifier gain.

Equation (4.28) has the same form as (4.35), which demonstrates that our simplified model in Fig. 4.7(b) explains the effect of the parametric process. By equating (4.35) and (4.28), $r(\phi)$ can be expressed into

$$|r(\phi = \pm\pi/4)| = \frac{bQA_{eff}}{2} r_{ind}, \tag{4.36}$$

where A_{eff} is the pump amplitude inside the resonator, given by $A_{eff} = A_{pin}/(1 - \exp(-2\alpha_p d))$. Equation (4.36) suggests that the phase-dependant resistance is proportional to the pump amplitude, the nonlinearity factor, and the resonator

quality factor. It is noteworthy that parametric amplification beyond the resonator loss ($r(\phi) > r_{ind}$ or $A_{pin} > A_{th}$) results in parametric oscillation, which can be exploited for low-noise frequency division discussed in Chapter 3.

However, the proposed amplifier does not use the extra transistor to compensate for the resonator loss since the gain comes from the parametric amplification. More importantly, the proposed amplifier provides the phase sensitive gain for the noise squeezing at the cost of its complicated structure.

4.3.4 Squeezing Factor

Finally, the minimum squeezing factor can be simply calculated based on the squeezing effect, assuming that the noise of the resonator itself is negligible. This is similar to calculating the NF of a conventional LNA where we assume that the effect of resonator loss is negligible and the NF is dominated by the channel noise[1]. Under this assumption the squeezing factor is:

$$S_F = K_s \cdot NF_0, \tag{4.37}$$

where K_s is the noise reduction ratio and NF_0 is the NF of the source-degenerated common-source amplifier. The noise reduction ratio, K_s, can be calculated using (4.8) and (4.28):

$$K_s = \frac{1}{2}\left[1 + \left(\frac{G_T|_{min}}{G_T|_{max}}\right)^2\right] = \frac{(A_{pin}/A_{th})^2 + 1}{(A_{pin}/A_{th} + 1)^2} \tag{4.38}$$

When A_{pin} approaches A_{th}, the reduction ratio, K_s, approaches $1/2$.

---

[1]For typical losses of on-chip passive components, this assumption is valid. Interested readers can use a similar approach shown in (4.17) to calculate NF when the resonator loss cannot be neglected.
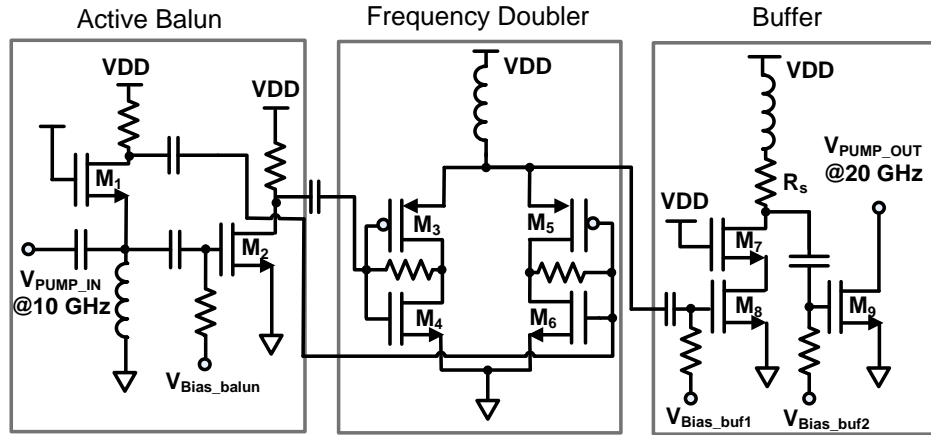
Figure 4.8: Schematic of the pump generation block consisting of active balun, frequency doubler, and buffer.

Fig. 4.6(b) shows the calculated squeezing factor with respect to the phase difference between signal and pump for different pump amplitudes based on (4.37). As expected in the gain plot, higher pump amplitude provides higher noise squeezing ratio for in-phase component, whereas it degrades the noise performance of out-of-phase component.

4.4 Design and Simulation

We designed and simulated the proposed amplifier at around 10 GHz in a 65 nm CMOS technology. The chip consumes 30 mW from a 1.2-V supply. This power includes the pump generation circuit, which consumes 14.5 mW. The estimated area of the entire chip is 1.5 mm×0.9 mm.

4.4.1 Design

The design of the proposed amplifier consists of three parts: a nonlinear resonator for phase-sensitive gain, a low noise amplifier for input stage, and a frequency doubler to generate a pump frequency that has exactly twice the input frequency. To design the resonator, we use the fact that its resonant frequency, which should be around 10 GHz, is closely related to the propagation constant, β, defined by $\beta = \omega \sqrt{lc_0} = 2(\omega/\omega_c)$. Also, as explained in Section 2.2, the cut-off frequency of the LC-ladder sets the maximum gain of the amplifier. The optimum cut-off frequency can be obtained from the trade-off between $\widetilde{s_0}$ in (2.26) and the pump loss due to the cut-off frequency which is comparable to the pump frequency. Using the optimum cut-off frequency of around 25 GHz for maximum gain, we need a fine adjustment to satisfy the resonant frequency of 10 GHz. The resonant frequency is determined from

$$d = nh = \frac{\lambda_s}{2} = \frac{\pi}{\beta} = \frac{1}{2 f_{osc} \sqrt{(l/h)(c_0/h)}}, \tag{4.39}$$

where d is the length of the resonator, h is the spacing between two adjacent nodes, and n is the number of resonator sections. The varactor capacitance per unit section is approximated by its average value, c_0. Equation (4.39) can be rearranged to:

$$f_{osc} = \frac{1}{2n \sqrt{lc_0}} = \frac{\pi f_c}{2n}. \tag{4.40}$$

Inserting the cut-off frequency into (4.40), the section number is around 3.9. Because we can only have positive integers, the section number is set to be four, which requires the minor adjustment of the cut-off frequency to keep the resonant frequency at 10 GHz (For accurate adjustment, the resonant frequency should be verified with Cadence simulation since eqs. (4.39) and (4.40) is based

on the small dispersion assumption.) Knowing the cut-off frequency of the line and the number of sections, we can determine the LC product. To pick the values of inductors and varactors, we need to select the characteristic impedance of the LC line. Since the resonator is driven with an LNA and the output is taken out using a buffer, the impedance does not have to be 50 Ω. As a result, we select the characteristic impedance to minimize the loss of the resonator, which is around 40 Ω. In this process, the optimized inductor and varactor value to achieve the maximum gain, i.e. optimum cut-off frequency, and minimum loss are 470 pH and 270 fF, respectively.

The inductor is implemented as a spiral whose inductance is 380 pH and dimension is 145 μm $\times$ 145 μm, including the guard ring. The quality factors of the spiral are 16 and 19 at 10 GHz and 20 GHz, respectively. The coplanar waveguide with a ground-shielded plane is employed to connect inductors. The inductance of these interconnects is around 90 pH. The transmission line structure is carefully simulated in an E/M simulator, SONNET.

We use an accumulation-mode MOS varactor as a voltage-dependent capacitor. Its capacitance versus voltage characteristic is shown in Fig. 4.9. The average capacitance is 270 fF and the linearized C/V slope, b, is approximated to be 1.4 around zero bias voltage. The quality factors of the varactor are 31 and 15 at 10 GHz and 20 GHz, respectively. The varactors use the multi-finger gate structure to optimize the nonlinearity and the quality factor simultaneously [28]. Metal-insulator-metal capacitors (MIMCAPs) are used for dispersion compensation capacitors.

The design of the low-noise amplifier for input stage follows a general source-degenerated amplifier for an input frequency of 10 GHz. The input

91
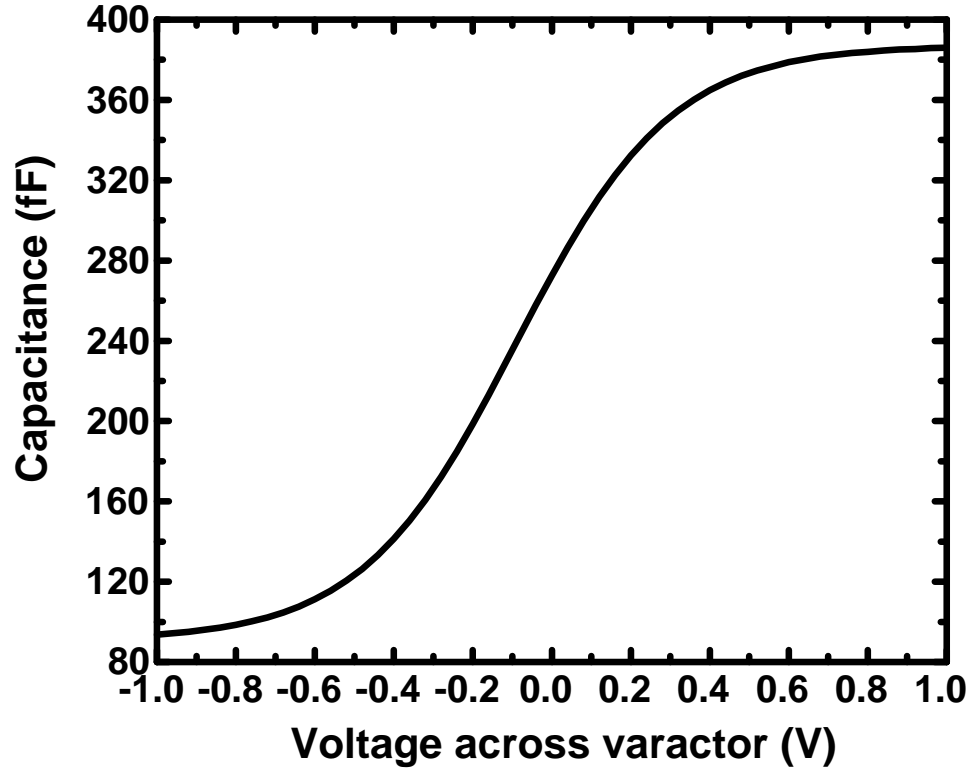
Figure 4.9: Accumulation-mode MOS varactor characteristic in a 65 nm process.

impedance is matched to 50 Ω. The main transistor (M_1 in Fig. 4.5) has a width of 96 μm for optimum NF and input matching with a bias current of 3 mA. The width of the cascode transistor (M_2) is selected considering the trade-off between the amount of parasitic capacitances and its noise contribution. In our design, the width of M_2 is 80 μm. Both M_1 and M_2 have the minimum channel length of 60 nm.

To generate the pump at twice the signal frequency, the frequency doubler is implemented as shown in Fig. 4.8. It consists of an active balun, a frequency doubler, and a buffer. Since the frequency doubler is designed for a differential input signal, an active balun is employed. The active balun (M_1-M_2 in Fig. 4.8) is
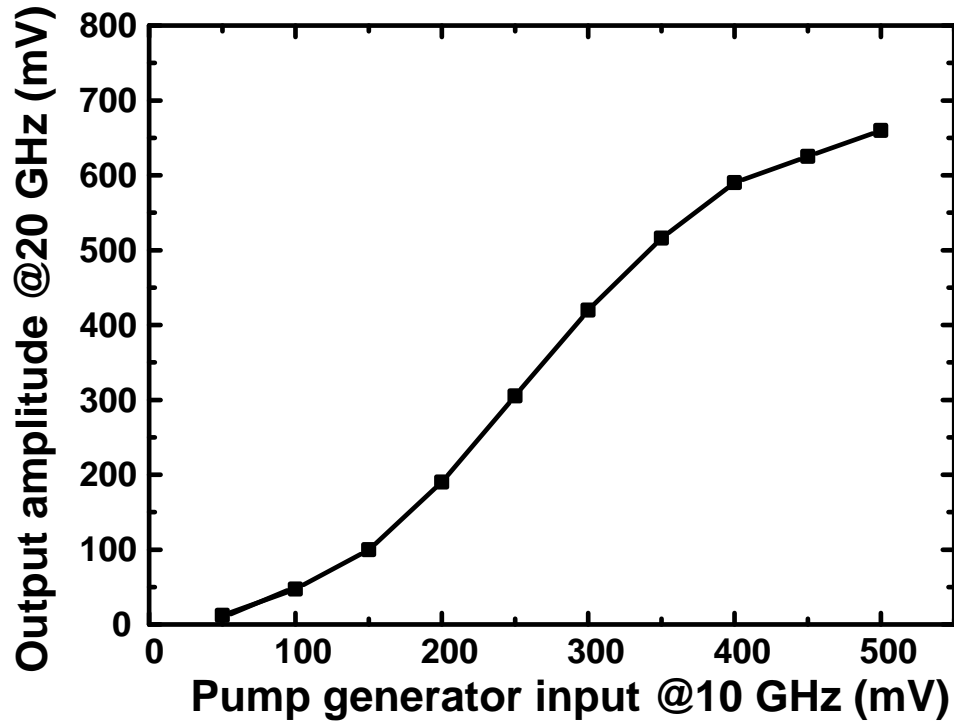
Figure 4.10: Simulated frequency-doubled output of the pump generation block versus input amplitude.

the combination of common-gate and common-source amplifiers to simultaneously generate a non-inverting and inverting output [28]. In addition, the common gate amplifier located in the input port provides a broadband input matching. The frequency doubler (M_3-M_6) uses the nonlinearity of the transistor. The even-order harmonics of the differential input signal, mainly the second-order harmonic, is picked at the common node through the resonant network. The last stage (M_7-M_9) is a two-stage amplifier as a buffer. The first stage amplifies the signal with a high gain, and the second stages drives the nonlinear resonator. Fig. 4.10 shows the simulated output amplitude of the pump generation block versus an input amplitude for different input frequencies in Cadence.
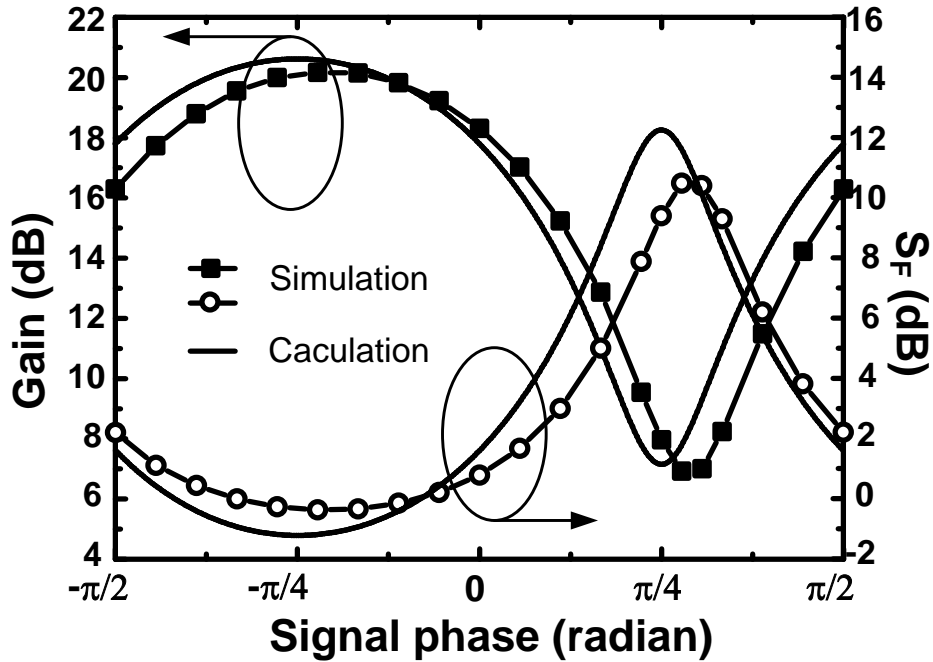
Figure 4.11: Calculated and simulated gain and squeezing factor versus signal phase in the proposed amplifier for a fixed pump amplitude (500 mV)

4.4.2 Simulation

Using Cadence, we simulated our designed amplifier, which consists of the input stage amplifier and the nonlinear resonator. The input of the amplifier is a 10 GHz signal (carrier) with bandwidth of 500 MHz (data). The pump frequency is fixed at 20 GHz, which is twice the carrier frequency. The outputs are connected to 50-Ω loads using source follower buffers. The simulation is carried out at a schematic level including an interconnects transmission line model verified by SONNET. We use Periodic Noise analysis (Pnoise) and Periodic S-parameter analysis (PSP) in Spectre to simulate the gain and squeezing factor of the proposed design.
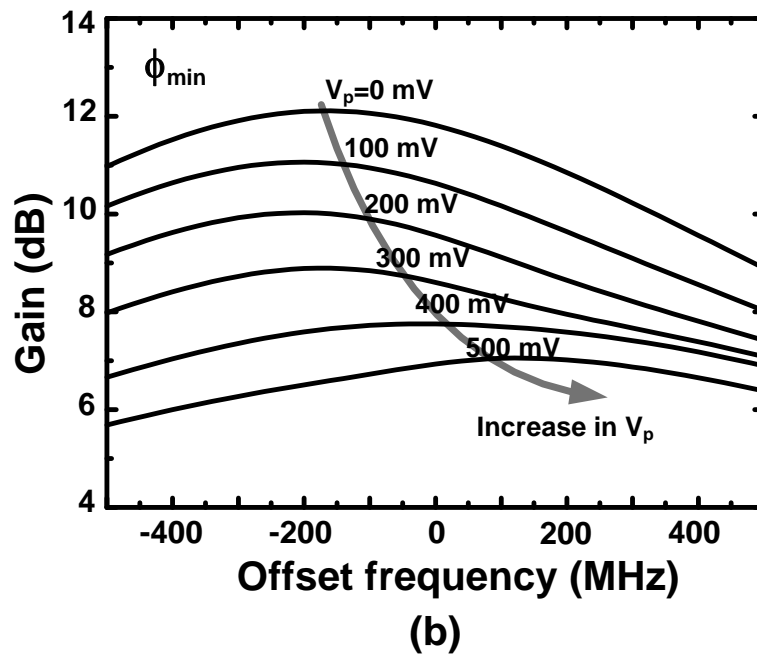
Figure 4.12: Cadence simulation of gain versus frequency for different pump amplitudes for (a) maximum gain and (b) minimum gain.

Figure 4.13: Cadence simulation of squeezing factor versus frequency for different pump amplitudes for (a) maximum gain and (b) minimum gain.

Figure 4.14: Cadence simulation of noise squeezing effect for (a) zero pump amplitude and (b) a pump amplitude of 500 mV.
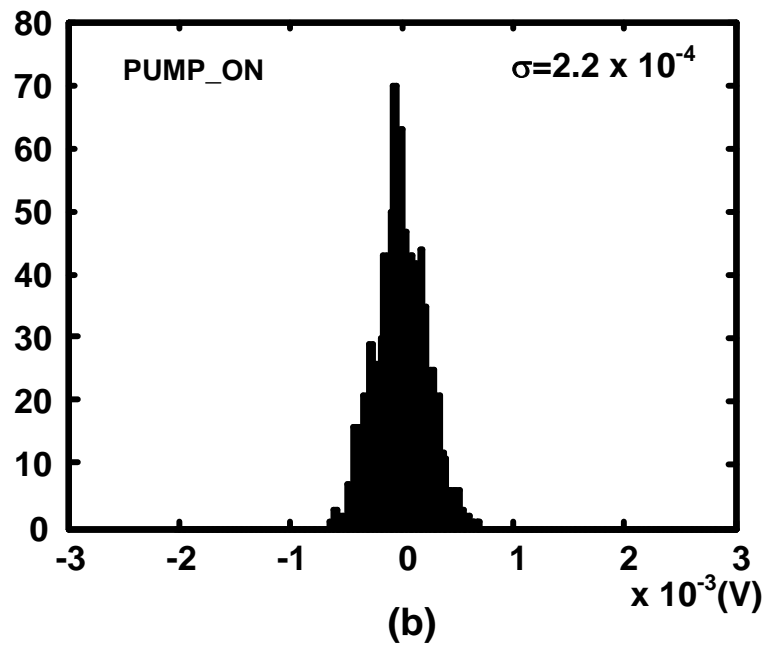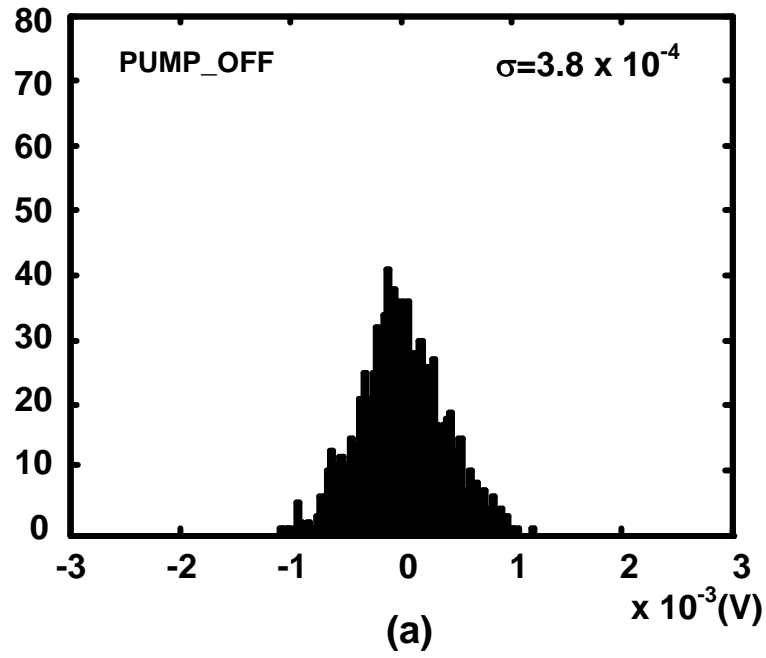
Figure 4.15: Simulated noise histogram for (a) zero pump amplitude and (b) a pump amplitude of 500 mV using Cadence.
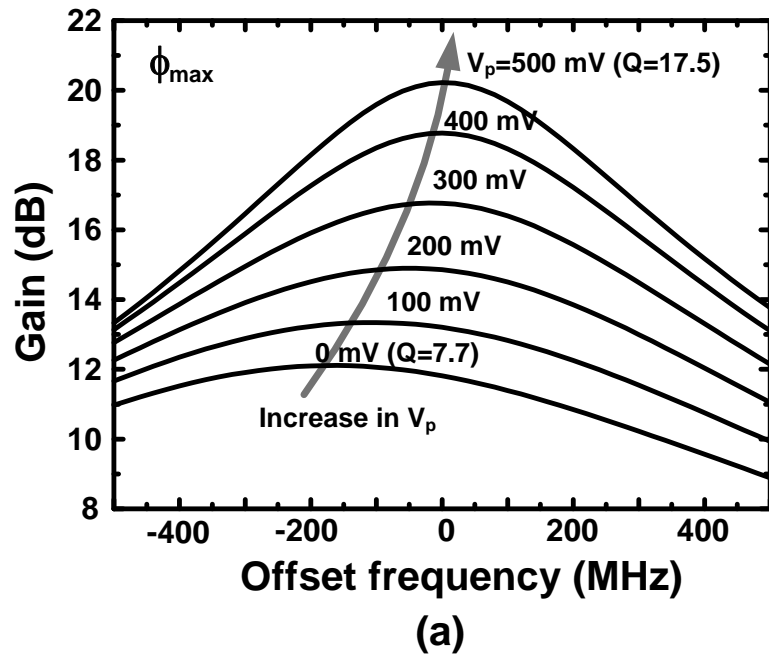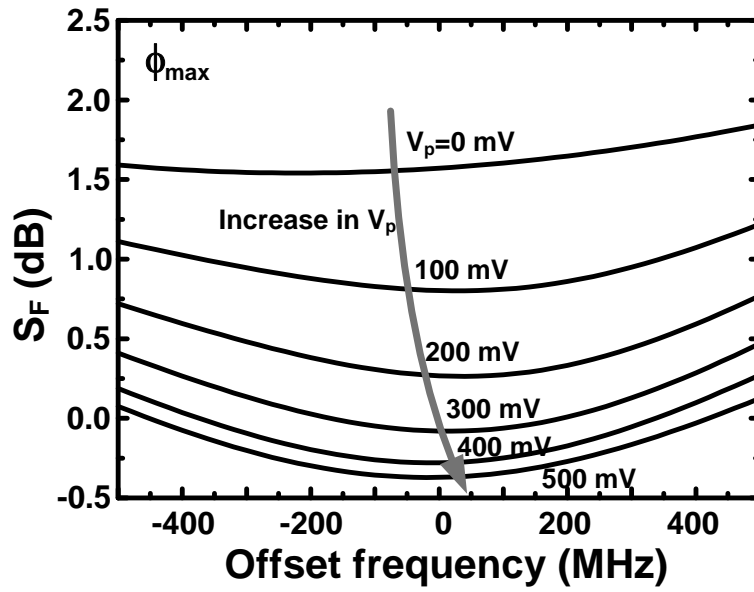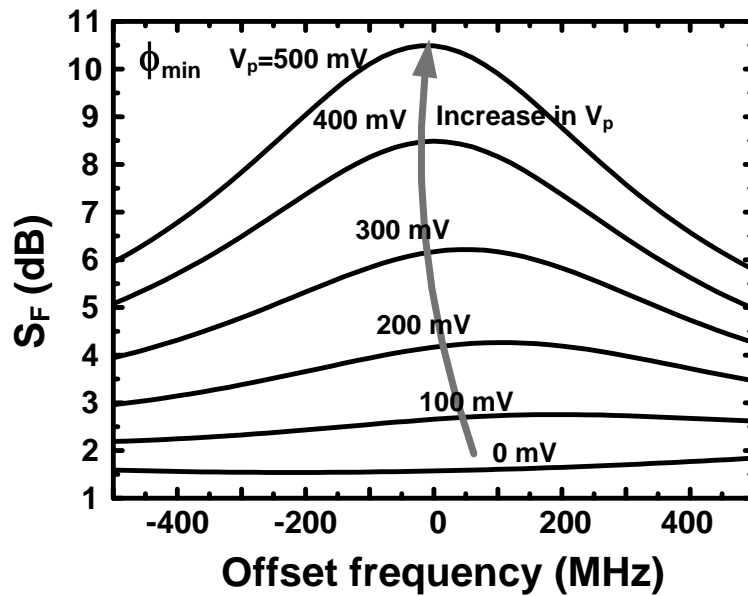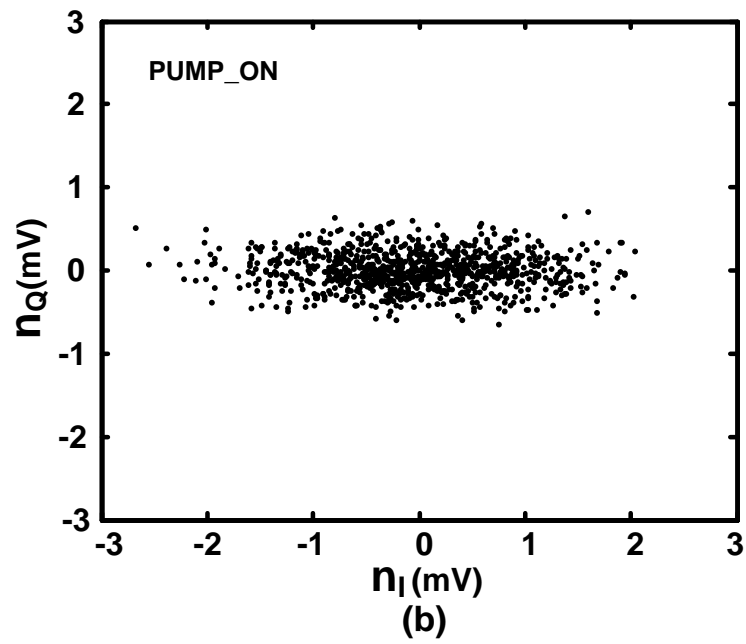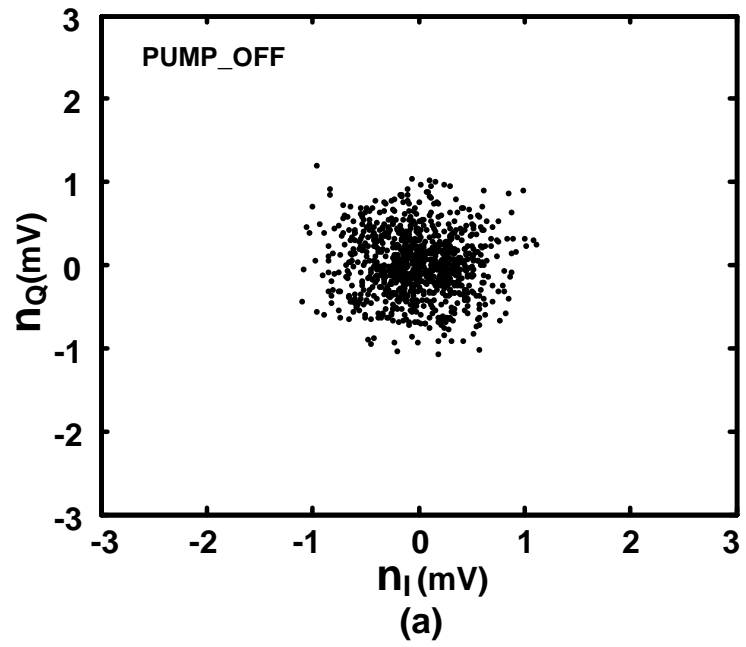
Fig. 4.11 shows both calculated and simulated gain and squeezing factor versus the signal phase for a fixed pump amplitude of 500 mV. For the calculation, we insert G_{T0}=11.5 dB and NF_0=1.6 dB into (4.31) and (4.37) based on the Cadence simulation. A_{pin}/A_{th} is set to be 0.65 for best fit with the simulation. Note that the accurate calculation of A_{th} is difficult due to the voltage-sensitive drain node impedance of the input amplifier. This is because the standing wave formation of the pump signal doubles the input pump voltage swing on the drain node, as shown in Fig. 4.5.

The gain ranges from 7 dB to 20 dB depending on the phase difference between signal and pump. The difference between maximum and minimum gains is around 13 dB, which determines the magnitude of the noise squeezing ratio in (4.37). As expected in (4.31), the plots are periodic with a period of π, and the signal phase difference between maximum and minimum gain is $\pi/2$, implying a quadrature squeezing. The simulated gain includes 6-dB loss due to the output buffer, which is not calibrated. (The maximum gain is 26 dB before the buffer whereas the graph in Fig. 4.11 shows 20 dB at its maximum.) The squeezing factor plot is the flip-down image of the gain plot, as we observed in Section III. Assuming that all the signal is in-phase component, the noise squeezing effect suppresses the squeezing factor even below 0 dB, resulting in the minimum squeezing factor of −0.37 dB when the gain is maximum. From (4.37) and (4.38), the theoretical squeezing factor is suppressed up to 3 dB below the NF of the input LNA as the pump input gets close to the oscillation threshold. However, the simulation result shows 2-dB suppression of the squeezing factor from 1.6 dB to −0.37 dB. This is because the additional loss from the drain node of the input amplifier increases the threshold voltage beyond the varactor saturation region, where the capacitance does not change with the voltage, as shown in

Fig. 4.9.

We also simulated the gain and squeezing factor for different pump amplitudes with a fixed signal phase, particularly for the maximum and minimum gain cases, as shown in Figs. 4.12 and 4.13. In the maximum gain case, the increase in pump amplitude boosts the gain by increasing the quality factor of the resonator. The increase in the quality factor can also be verified in Fig. 4.12(a), as well as by observing that the bandwidth becomes narrower with pump amplitude. Fig. 4.13(a) shows that the squeezing factor is more suppressed as the difference between maximum and minimum gain increases with pump amplitude due to the squeezing effect. On the other hand, Fig. 4.12(b) shows that the increase in pump amplitude decreases the signal gain for a phase at minimum gain. The destructive adding process causes more signal attenuation inside the resonator with the pump amplitude, degrading the quality factor. The squeezing factor also becomes worse due to signal loss, as shown in Fig. 4.13(b).

The noise squeezing effect is also clearly observed using the transient noise option in the transient analysis in Cadence, as shown in Fig. 4.14. In the simulation setup, two independent noise voltages, whose bandwidth is 500 MHz, are generated and combined though I/Q modulation at 10 GHz LO frequency. The combined noise signal is injected to the resonant parametric amplifier. After passing through the proposed amplifier, the output is demodulated to extract I/Q components and sampled for statistical analysis. In the transient simulation, it is noted that the intrinsic device noise is neglected due to a large-signal input noise source. Fig. 4.14 shows the simulated noise squeezing, depending on the presence of the pump. Before the pump injection, the output noise distribution is still circularly symmetric for in-phase and out-of-phase components

100
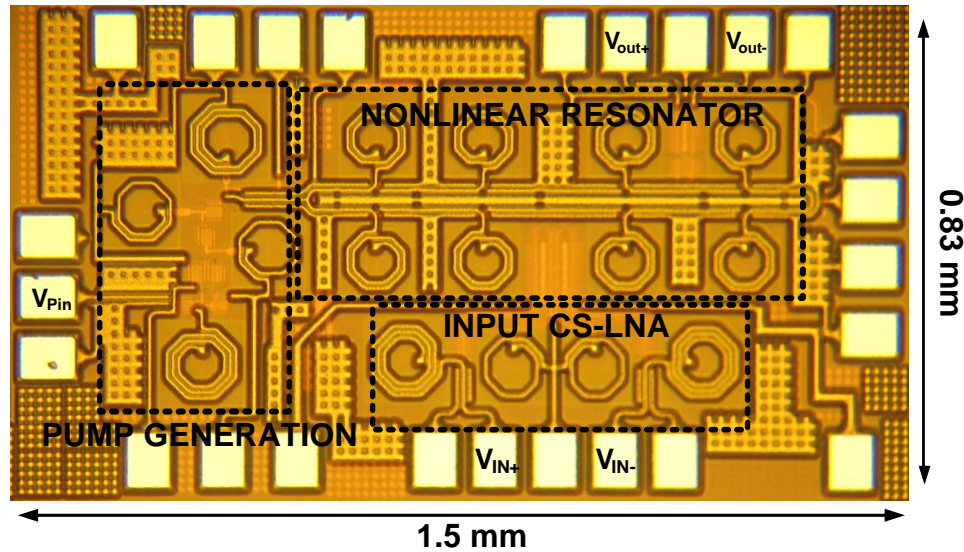
Figure 4.16: The fabricated amplifier in a 0.13-μm CMOS process.

(and hence phase-insensitive). However, the out-of-phase noise component is suppressed in the presence of the pump signal, whereas the in-phase noise component is amplified. Note that the input signal is also equally amplified with the in-phase noise component. To analyze the suppressed out-of-phase noise component quantitatively, the histogram is plotted for 960 samples, as shown in Fig. 4.15. We clearly observe that the standard deviation of the out-of-phase noise component is significantly suppressed with pump injection.

4.5   Measurement Results

The proposed amplifier is fabricated in a 0.13-μm CMOS process, as shown in Fig. 4.16. The chip occupies 1.5 mm × 0.83 mm including pads. The total power consumption is 44 mW from a 1.2-V power supply, where the differential LNA, the pump generation block, and the output buffer consume 16 mW, 20 mW, and
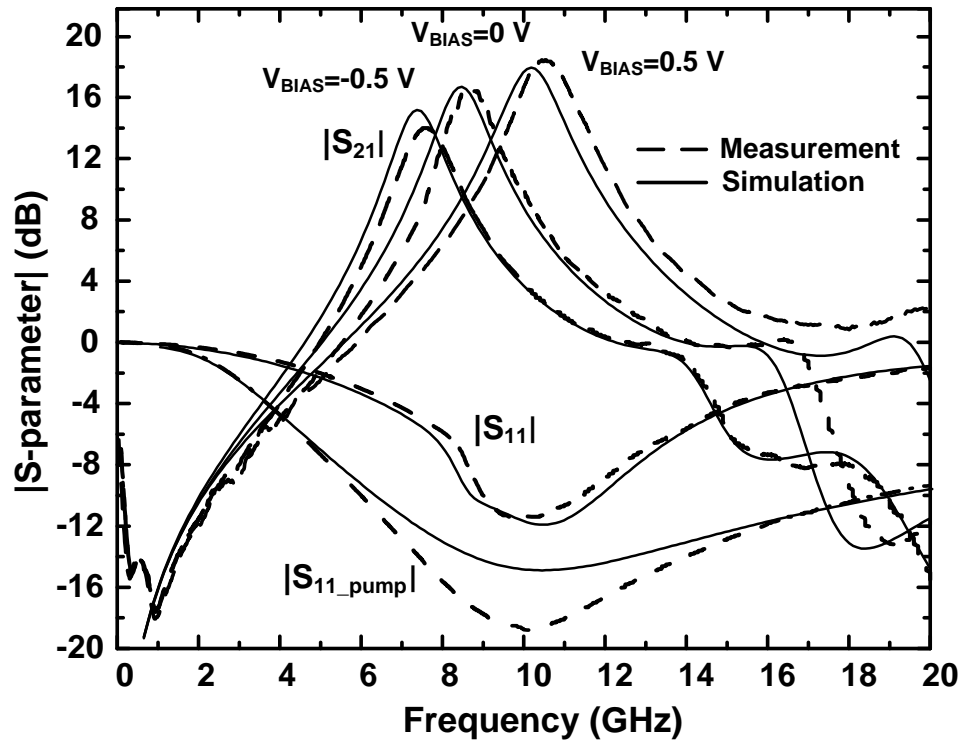
Figure 4.17: Measured and simulated S-parameters for different control voltages.
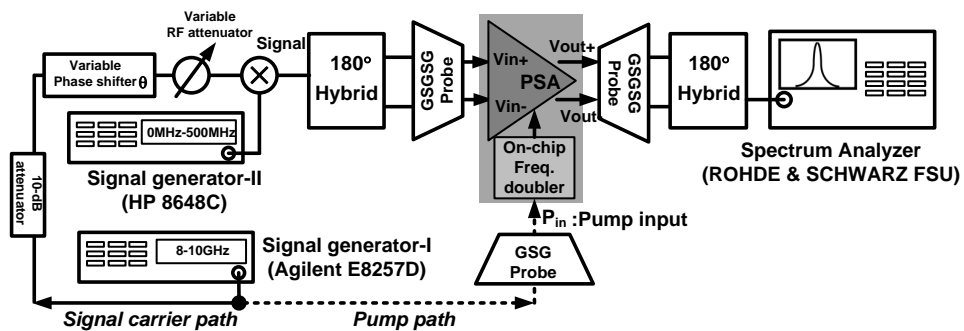
Figure 4.18: Phase-sensitive gain measurement setup.

8 mW, respectively. Figure 4.17 shows measured differential $|S_{21}|$ without the pump for different varactor bias voltages ($V_{BIAS} = V_{DD} - V_C$). The change in the bias voltage tunes the resonant frequency from 7.5 GHz to 10.5 GHz. The peak gain increases with the bias voltage since positive bias voltages force the varactors to operate in a depletion regime that provides higher quality factors. The measured quality factors of the resonator are 5.2, 6.3, and 8 for varactor bias voltages of −0.5 V, 0 V, and 0.5 V, respectively. Input matchings for the amplifier and the pump-generation block are also plotted in Fig. 4.17.

The phase-sensitive gain is measured using a fully differential setup, as depicted in Fig. 4.18. The input signal is generated using an external passive mixer and two sources: an Agilent E8257D for carrier generation at 8-to-10 GHz and an HP 8648C for data signal generation at 0-to-500 MHz. The input of the pump-generation block is also from the same source used for carrier generation. Power levels into the amplifier and pump-generation circuits can be independently controlled by adjusting the input power and a variable RF attenuator. The signal phase can be adjusted with a variable phase shifter, which provides 0-to-720° at the carrier frequency. The output spectrum is measured by the spectrum analyzer.

Figure 4.19 shows the simulated and measured phase-sensitive gain normalized to the gain in the absence of the pump (G_0). This measurement was performed with the input-carrier frequency of 8.75 GHz that gives the maximum squeezing factor. We also modulate the input carrier with a 1-MHz sinusoid to distinguish the signal from undesired harmonics at the output. Here, the injected power to the pump-generation block is kept constant at $P_{in} = 1$ dBm for the maximum squeezing factor. For simulation, this injected power is set at -2
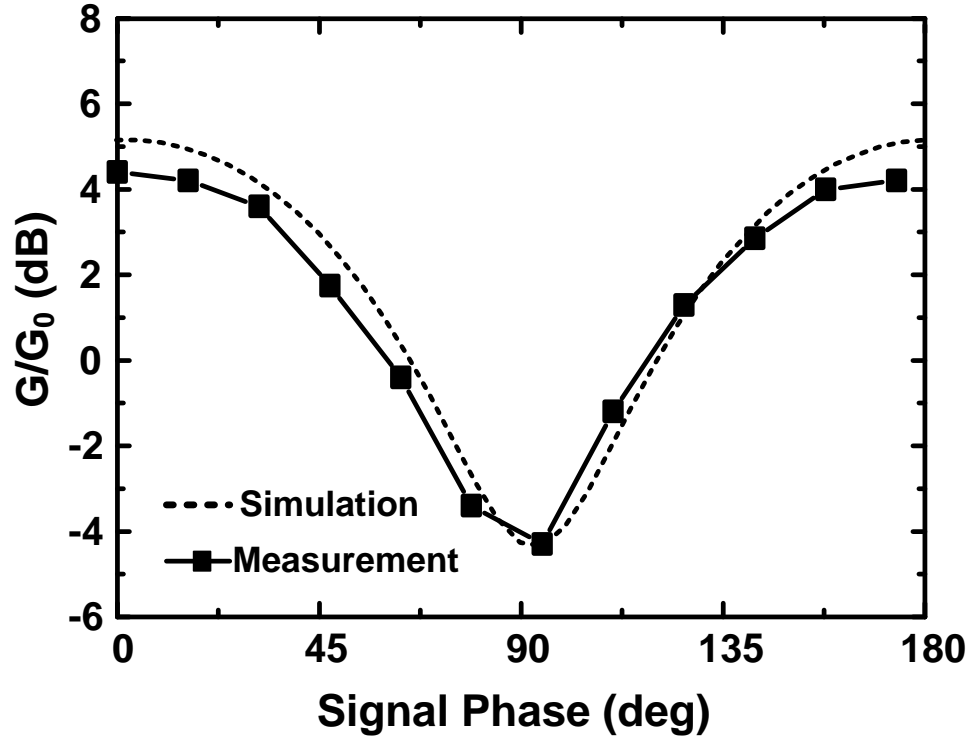
Figure 4.19: Measured and simulated phase-sensitive gain vs. signal phase.

dBm for the maximum squeezing factor. The measured maximum gain difference between in-phase and quadrature (G_I/G_Q) is around 9 dB, which results in the squeezing factor of 2.5 dB. For accurate simulation, parasitic inductance and capacitance, especially at the connection between the input amplifier and the resonator, are extracted using E/M simulator, Sonnet.

The in-phase and quadrature gains, G_I and G_Q, are also measured with respect to P_{in} as shown in Fig. 4.20. The increase in P_{in} boosts in-phase gain G_I and reduces quadrature gain G_Q according to (4.28) and (4.36). For P_{in} of 1 dBm, the in-phase gain G_I and gain difference G_I/G_Q have the maximum values of 21 dB and 9 dB, respectively. For P_{in}'s higher than 1 dBm, G_I drops since a large pump swing pushes the transistors of the input LNA into operating in the triode re-
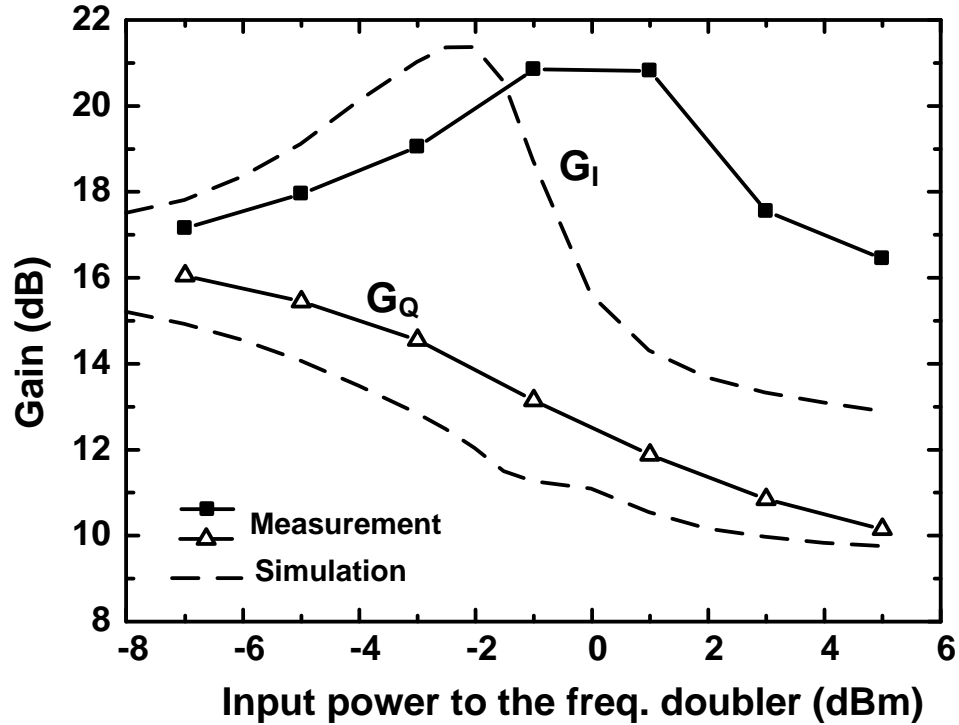
Figure 4.20: Measured and simulated in-phase and quadrature gain vs. pump power.

gion. Compared with the simulation, the measured optimum injection power is 3-dB higher due to the center frequency shift and the conversion gain difference between simulation and measurement in the pump generation block. For Fig. 4.20, the input carrier frequency and data frequency are again set at 8.75 GHz and 1 MHz, with a bias voltage of 0 V.

To investigate the operation frequency range, the quadrature gain difference G_I/G_Q is measured for different carrier frequencies and bias voltages, as shown in Fig. 4.21. When the bias voltage of varactors V_{BIAS} is 0 V, the quadrature gain difference is at the maximum. As the control voltage is deviated from 0 V, the nonlinearity of the varactor decreases, as shown in Fig. 2.6. This lowers the parametric gain of the amplifier. The phase-sensitive gain is also measured
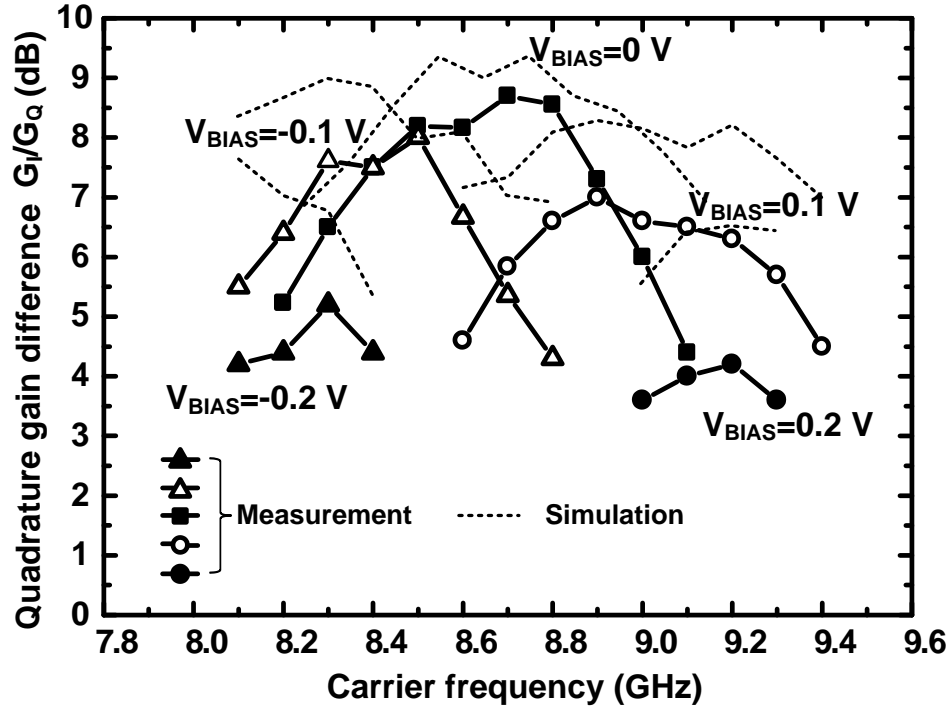
Figure 4.21: Measured and simulated quadrature gain difference G_I/G_Q for different control voltages.

vs. data frequency for the fixed carrier frequency of 8.75 GHz as shown in Fig. 4.22. As data frequency increases, the phase relation between the signal and the pump is not maintained, decreasing the quadrature gain difference.

To measure sensitivity, we first measure the noise figure in the absence of the pump, NF_0, using the Y-factor method [29], as shown in Fig. 4.23. Using this result, we can calculate the input-referred noise power in the absence of the pump as $N_{in0} = NF_0 \cdot N_i$. It is noteworthy that the pump-generation block is turned on (with no P_{in}) in order to include the noise from the pump-generation circuit in NF_0. Next, to see how the output noise power is changed after pump injection, we measure noise gain G_N using a high-power broadband noise source (Agilent 346C), as shown in Fig. 4.24. Since the power of the noise source is large
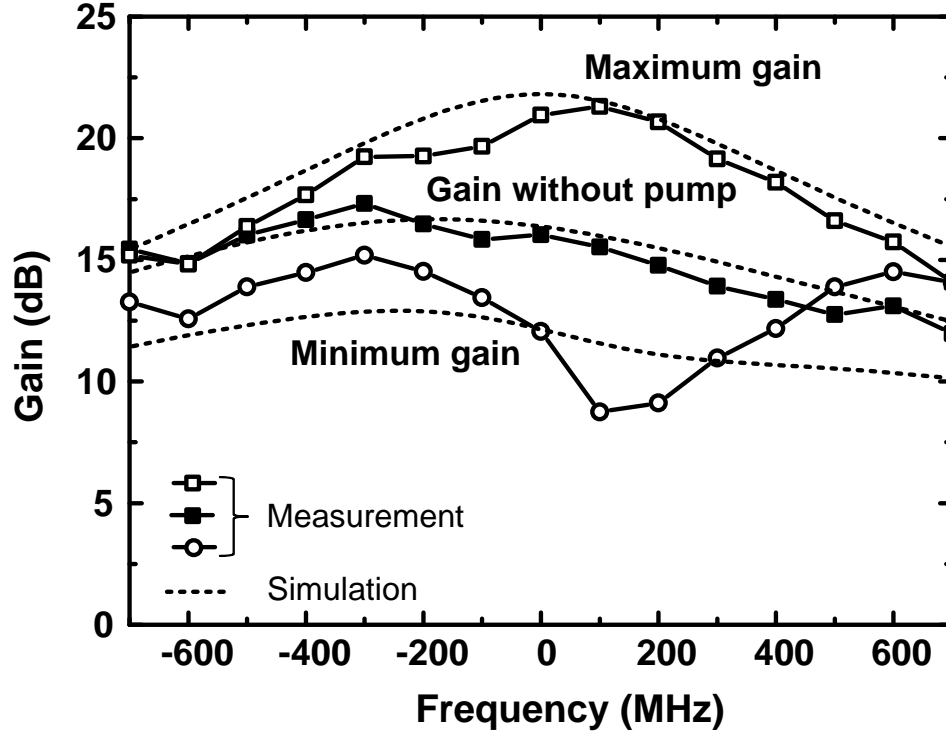
Figure 4.22: Measured and simulated phase-sensitive gain vs. frequency for the in-phase and quadrature components compared to gain in the absence of the pump.

enough, we can ignore the contribution of the amplifier to the output noise. The measured noise gain is shown in Fig. 4.25. The noise gain is equal to the average of in-phase and quadrature gains (i.e., $(G_I^2 + G_Q^2)/2$) according to the equi-partition theorem. Using this principle and the results of Fig. 4.22, we also calculate the noise gain from the signal gain, as shown in Fig. 4.25. The measured and calculated noise gain agree well within frequencies of interest, which proves that the phase-sensitive gain also works for noise input. From the measured noise gain, the output noise power can be estimated as $N'_{out} = G_N^2 N_{in0}$. Finally, the input-referred noise in the presence of the pump can be estimated by dividing the output noise power by the measured signal gain. Figure 4.26 shows the ratio of the measured input-referred noise (N_{in}) to input noise (N_i). This noise
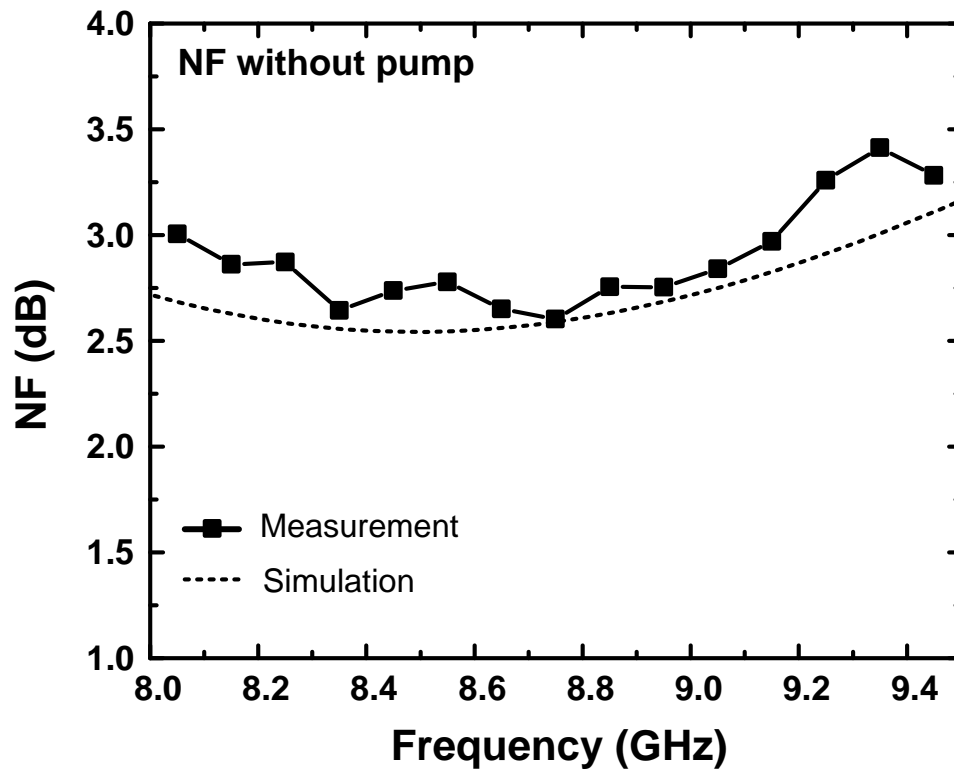
Figure 4.23: Measured and simulated NF in the absence of the pump.
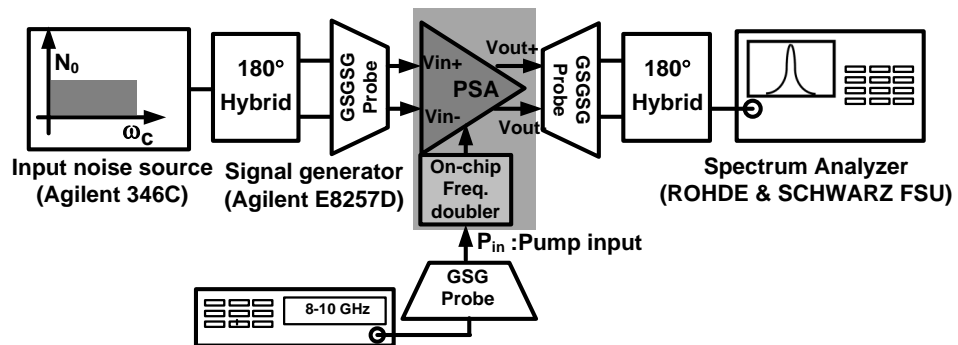
Figure 4.24: NF and noise gain measurement setup.
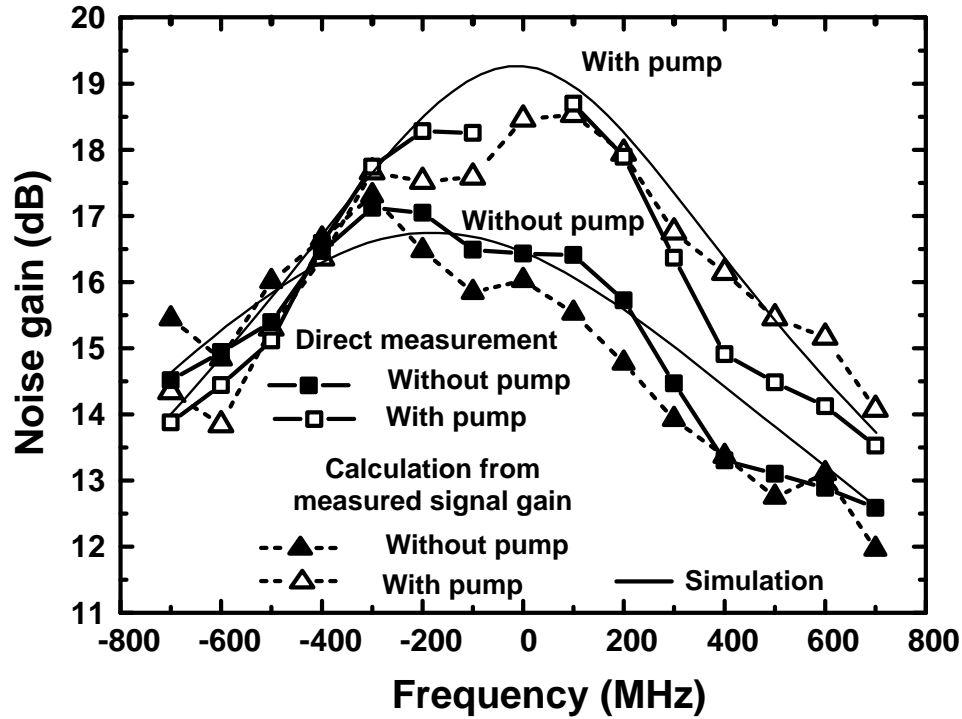
Figure 4.25: Measured and simulated noise gain compared with the calculation using the results of Fig. 4.22.

ratio is equal to NF when the information is placed only in the single quadrature phase. For the in-phase input signal, the measured minimum detectable power is around 0.1 dB below N_i at the expense of degrading the quadrature sensitivity. This demonstrates that sensitivity below the thermal noise limit can be achieved by the proposed amplifier.

Linearity performance is measured in terms of a 1-dB gain-compression point and input-referred IP3 with/without a pump. Figure 4.27 shows the measured 1-dB gain-compression point. P_{1dB} is around -2.1 dBm in the absence of the pump. After the pump injection, P_{1dB} is changed to -5 dBm for in-phase gain G_I and 1.1 dBm for quadrature gain G_Q. Figure 4.28 shows the measured IIP3 with/without the pump. IIP3 is -10.5 dBm in the absence of the pump and is
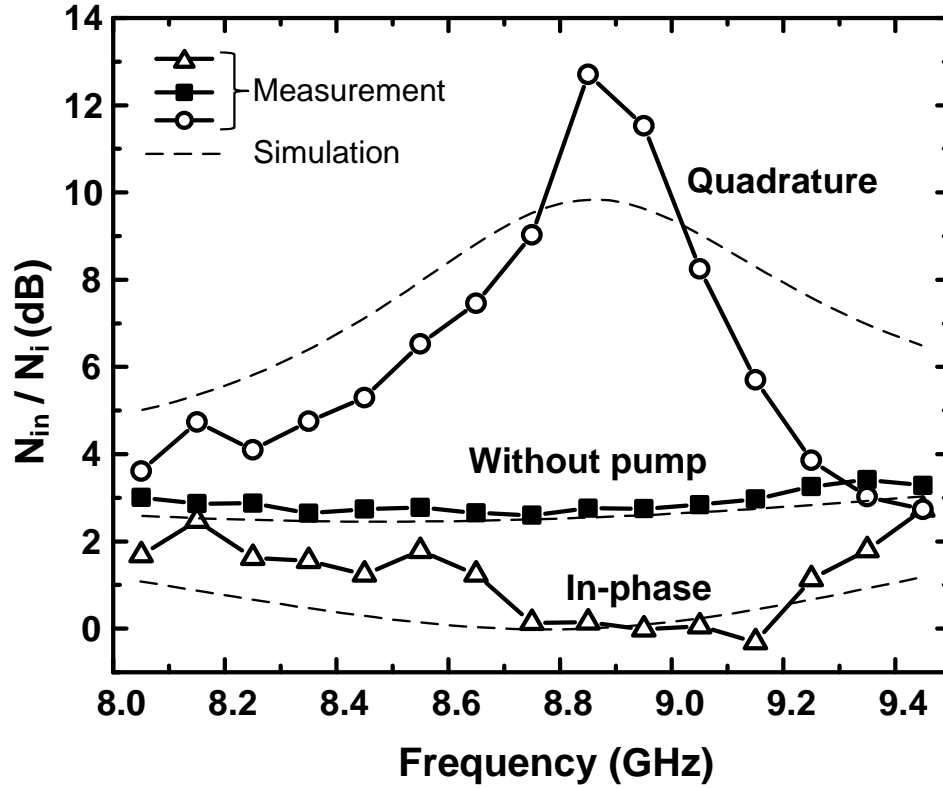
Figure 4.26: Measured and simulated input-referred noise normalized to N_i for in-phase and quadrature compared with when the pump is off.

decreased to -12.5 dBm for G_I when the pump is applied. To investigate how the nonlinear resonator affects the linearity performance, we simulated the performance after replacing the varactors with constant capacitors. The 1-dB compression point and IIP3 of the amplifier with linear resonator are less than 1 dB better than the nonlinear case. This proves that the varactors mainly generate the second-order nonlinearity and have minimal effect on the 1-dB compression point and IIP3, which capture the odd order nonlinearities.
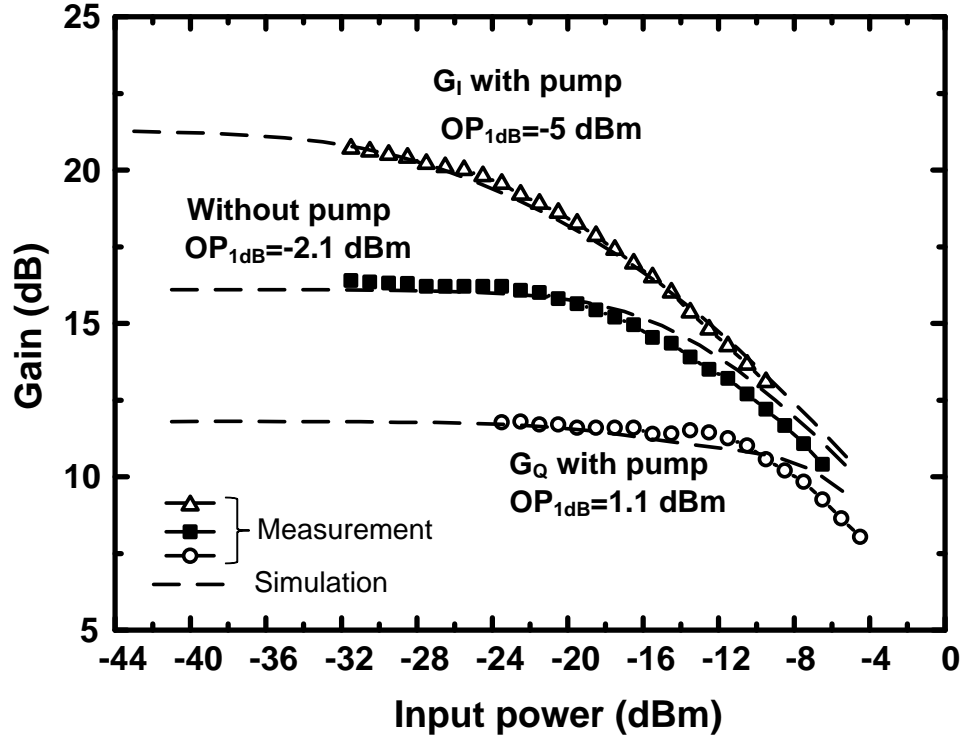
Figure 4.27: Measured and simulated gain saturation characteristics with
and without the pump.

4.6   Conclusion

We propose a resonant parametric amplifier with a low noise performance using
the noise squeezing effect. The phase-sensitive amplification process suppresses
one of the quadrature noise components and achieves around 3-dB noise reduc-
tion for single phase information compared to the phase-insensitive amplifica-
tion. The resonant structure of the amplifier, which resembles the *Fabry-Perot*
laser amplifier, enables parametric amplification for narrow-band signals with
a small number of lumped LC elements. The signal gain and squeezing factor
are analyzed theoretically based on the continuous transmission line approxi-
mation and the steady state assumption. In the measurement, we proved that
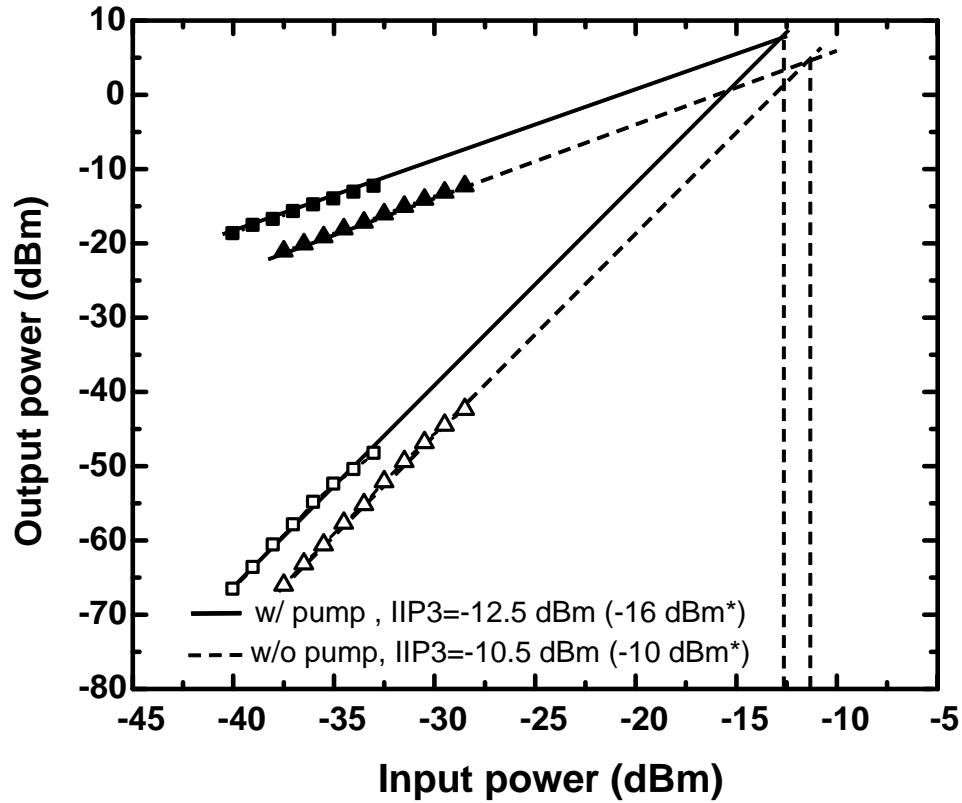
Figure 4.28: Measured and simulated IIP3 with and without the pump (* are the simulation results).

the implemented parametric resonant amplifier provides a gain difference of 9 dB between in-phase and quadrature at 8.75 GHz. This quadrature gain differ-ence results in a 2.5-dB improvement of the sensitivity for one quadrature at the expense of the degradation of the other quadrature. For linearity performance, P_{1dB} and $IIP3$ were measured to be -5 dBm and -12.5 dBm, respectively, which are comparable to a linear resonant amplifier.

BIBLIOGRAPHY

[1] D.K. Shaeffer and T.H. Lee, "A 1.5-V, 1.5-GHz CMOS Low Noise Amplifier," *IEEE J. Solid-Stat Circuits*, vol. 32, no. 5, pp. 745-759, May 1997.

[2] A. Nieuwoudt, T. Ragheb, H. Nejati, and Y. Massoud, "Numerical Design Optimization Methodology for Wideband and Multi-Band Inductively Degenerated Cascode CMOS Low Noise Amplifiers," *IEEE Trans. Circuits Syst. I, Reg. Papers*, vol. 56, no. 6, pp. 1088-1101, June 2009.

[3] X. Li, S. Shekhar, and D.J. Allstot, "G_m-Boosted Common-Gate LNA and Differential Colpitts VCO/QVCO in 0.18-μm CMOS," *IEEE J. Solid-Stat Circuits*, vol. 40, no. 12, pp. 2609-2619, Dec. 2005.

[4] A. Liscidini, M. Brandolini, D. Sanzogni, and R. Castello, "A 0.13 μm CMOS Front-End for DCS1800/UMTS/802.11b-g With Multiband Positive Feedback Low-Noise Amplifier," *IEEE J. Solid-Stat Circuits*, vol. 41, no. 4, pp. 981-989, Apr. 2006.

[5] L. Belostotski and J.W. Haslett, "Sub-0.2 dB Noise Figure Wideband Room-Temperature CMOS LNA With Non-50Ω Signal-Source Impedance," *IEEE J. Solid-Stat Circuits*, vol. 42, no. 11, pp. 2492-2502, Nov. 2007.

[6] J.M. Manley and H.E. Rowe, "Some General Properities of Nonlinear Elements –Part I. General Energy Relations," *Proc. IRE*, pp. 904-913, July 1956.

[7] Y. Yamamoto, "Characterisitics of AlGaAs Fabry-Perot cavity type laser amplifiers," *IEEE J. Quantum Electronics*, vol. 16, no. 10, pp. 1047-1052, Oct. 1980.

[8] K.G. Köprülü and O. Aytür,"Analysis of the Generation of Amplitude-Squeezed Light with Gaussian-Beam Degenerate Optical Parametric Amplifiers," *J. Opt. Soc. Am. B*, vol. 18, no. 6, pp. 846-854, June 2001.

[9] T. Hirano, K. Kotani, T. Ishibashi, S. Okude, and T. Kuwamoto, "3 dB Squeezing by Single-Pass Parametric Amplification in a Periodically Poled *KTiOPO$_4$* Crystal," *Optics Letters*, vol. 30, no. 13, pp. 1722-1724, July 2005.

[10] D. Rugar, "Mechanical Parametric Amplification and Thermomechanical Noise Squeezing," *Phys. Rev. Lett.*, vol. 67, no. 6, pp.699-702, Aug. 1991.

[11] R. Almog, "Noise Squeezing in a Nanomechanical Duffing Resonator," *Phys. Rev. Lett.*, doi:10.1103/PhysRevLett.98.078103, Feb. 2007.

[12] B. Yurke, "Squeezed-State Generation Using a Josephson Parametric Amplifier," *J. Opt. Soc. Am. B*, vol. 4, no. 10, pp. 1551-1557, Oct. 1987.

[13] B. Yurke, "Observation of 4.2-K Equilibrium-Noise Squeezing via a Josephson-Parametric Amplifier," *Phys. Rev. Lett.*, vol. 60, no. 9, pp. 764-767, Feb. 1988.

[14] M.A. Castellanos-Beltran, K.D. Irwin, G.C. Hilton, L.R. Vale, and K.W. Lehnert, "Amplification and Squeezing of Quantum Noise with a Tunable Josephson Metamaterial," *Nature*, doi:10.1038/nphys1090, Oct. 2008.

[15] W.H. Louisell, *Coupled Mode and Parametric Electronics*, Wiley, New York, NY, 1960.

[16] P.K. Tien and H. Suhl, "A Traveling-wave Ferromagnetic Amplifier," *Proc. IRE*, vol. 46, pp. 700-706, Apr. 1958.

[17] P.K. Tien, "Parametric Amplification and Frequency Mixing in Propagating circuits," *Journal of Applied Physics*, vol. 29, no. 9, pp. 1347-1357, Sep. 1958.

[18] D.M. Pozar, *Microwave Engineering*, Wiley, New York, NY, 2005.

[19] J. J. Waterston, "On the physics of media that are composed of free and elastic molecules in a state of motion,". *Roy. Soc. Proc.* vol. 5: 604, 1846.

[20] W. Greiner, L. Neise, and H. Stocker, *Thermodynamics and Statistical Mechanics*, Springer, New York, NY, 1995.

[21] R.F. Wiser, M. Zargari, D.K. Su, and B.A. Wooley, "A 5-GHz Wireless LAN Transmitter with Integrated Tunable High-Q RF Filter,", *IEEE J. Solid-Stat Circuits*, vol. 44, no. 8, pp. 2114-2125, Aug. 2009.

[22] Chien-Chih Ho, et al."0.13-um RF CMOS and Varactors Performance Optimization by Multiple Gate Layouts," *IEEE Tran. Electron Devices*, vol. 51, no. 12, pp. 2181-2185, Dec. 2004.

[23] *CMRF8SF Model Reference Guide*, IBM Microelectronics Division, Apr. 2007.

[24] L.E. Myers, R.C. Eckardt, M.M. Fejer, and R.L. Byer, "Quasi-Phase-Matched Optical Parametric Oscillators in Bulk Periodically Poled *LiNbO$_3$*," *J. Opt. Soc. Am. B*, vol. 12, no. 11, pp. 2102-2116, Nov. 1995.

[25] G.M. Roe and M.R. Boyd, "Parametric Energy Conversion in Distributed Systems," *Proc. IRE*, vol. 47, pp. 1213-1218, Jul. 1959.

[26] R. Landauer, "Parametric Amplification Along Nonlinear Transmission Lines," *Journal of Applied Physics*, vol. 31, pp. 479-484, 1960.

[27] Chien-Chih Ho, et al., "0.13-um RF CMOS and Varactors Performance Optimization by Multiple Gate Layouts," *IEEE Tran. Electron Devices*, vol. 51, no. 12, 2004.

[28] R. Bagheri et al., "An 800-MHz-6-GHz Software-Defined Wireless Receiver in 90-nm CMOS," *IEEE J. Solid-Stat Circuits*, vol. 41, no. 12, pp. 2860-2876, Dec. 2006.

[29] Agilent Application Note 57-1, http://cp.literature.agilent.com/litweb/pdf/5989-8359EN.pdf.

CHAPTER 5

A NONLINEAR LATTICE FOR HIGH-AMPLITUDE PICOSECOND PULSE GENERATION IN CMOS

5.1 Introduction

Recently, there has been growing interest in generating picosecond pulses for high-speed sampling, time-domain reflectometry, sensing and imaging, radar, and pulse-based wireless communication [1–5]. To generate a sharp pulse, a special form of nonlinear wave known as a soliton has been extensively studied in optics and electronics [6–12]. To implement an electrical nonlinear medium, a transmission line periodically loaded with voltage-dependent capacitors, e.g., Schottky diodes, was proposed in a GaAs technology in the early 1990s [11, 12]. Recently, a nonlinear transmission line in a CMOS technology has been proposed using accumulation-mode MOS varactors [13]. However, generating sharper pulses in CMOS is more challenging due to the high loss of passive components, lowering the effect of nonlinearity. For instance, the quality factor of varactors is less than 5 above 100 GHz in a typical CMOS technology.

To overcome this limit, the concept of the nonlinear transmission line has been extended to a two-dimensional nonlinear lattice to boost the harmonic generation resulting in higher-amplitude, narrower pulses [14–17]. Our prior work in [14] analyzed the optimum input frequency for the maximum harmonic generation based on numerical analysis, and the lattice was fabricated on a printed circuit board (PCB) for an input frequency of around 20 MHz. We also numerically analyzed a lossless nonlinear lattice based on a discrete model using a perturbative method [15, 16]. Although our recent work in [17] showed promising

simulation results of the nonlinear lattice in a CMOS process, there are several implementation challenges that need to be addressed, including the selection of an output node without pulse distortion as well as input power distribution with high enough power level to fully exploit nonlinearity.

In this chapter, by addressing the above issues, we implement an integrated nonlinear lattice in a standard 0.13-μm CMOS process to demonstrate 2.7-V_{pp}, 6.3-ps pulses from a 22-GHz sinusoidal input. To the best of our knowledge, among the high-amplitude pulses (>1 V), this work shows the sharpest pulse in a CMOS process. This chapter also has a significant theoretical extension towards the insightful understanding of a nonlinear lattice. First, we develop a continuous model of a nonlinear transmission line to obtain an analytical form of harmonic generation based on coupled wave equations in the presence of loss and dispersion. Based on this result, we analyze the limitation of a lossy nonlinear transmission line in a CMOS process and introduce a nonlinear lattice as an alternative. We show that the proposed structure exploits spatial power combining, higher cut-off frequency, and two-dimensional nonlinear interference to significantly enhance both the amplitude and pulse width, compared with a 1-D nonlinear transmission line.

The rest of the chapter is organized as follows. Section 5.2 explains the theory of the harmonic generation in a nonlinear transmission line. Then, Section 5.3 proposes a two-dimensional nonlinear lattice as an extension of the transmission line and discusses its operation principle. Section 5.4 presents the design, simulation results, and the implementation details. Section 5.5 presents the measurement results. Section 5.6 discusses the effect of high-order harmonics and presents a half-size triangular lattice.
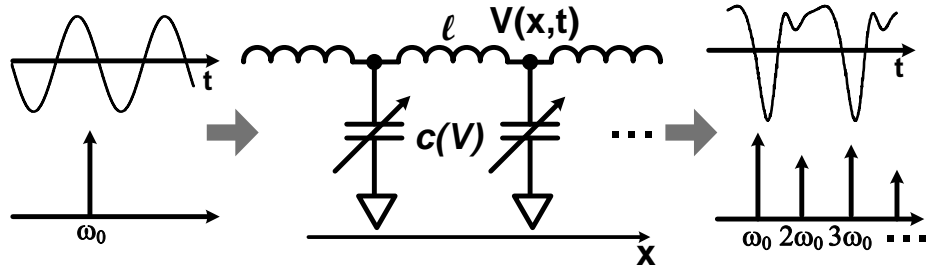
Figure 5.1: Nonlinear transmission line for harmonic generation and pulse
sharpening.

5.2   Distributed Harmonic Generation Theory

Fig. 5.1 shows a 1-D transmission line consisting of inductors l and voltage-dependant capacitors $c(V)$. As a sinusoid of frequency ω_0 travels along the line, the nonlinearity causes input energy at ω_0 to be transferred into multiple harmonics of the signal. This process results in sharpening the signal in the time domain, generating a narrow pulse. If the ratio of the energy of the higher-order harmonics to the total energy of the signal is larger, the resulting pulse becomes sharper. To describe the harmonic generation in a low-loss nonlinear transmission line, soliton propagation can be a useful model, which is reduced to the Burgers equation (zero-dispersion case) or the KdV equation (dispersion case) [8,9]. However, the problem with this method is that it presents only the steady-state solution. In this paper, to capture the harmonic generation as the signal propagates along the transmission line, we use coupled-wave equations.

The basic principle of harmonic conversion along the nonlinear transmission line is illustrated in Fig. 5.2. We conceptually model a nonlinear transmission line as multiple coupled transmission lines, each for a different harmonic. The generated harmonic component at each section is constructively added on the
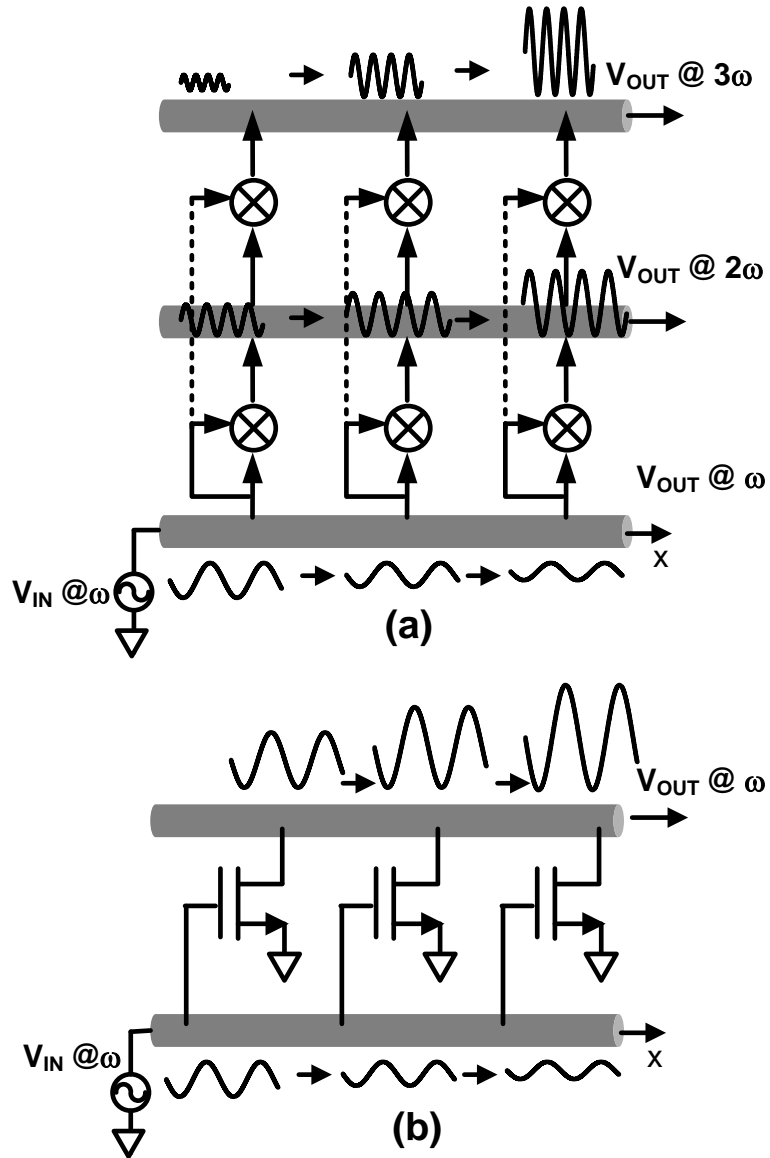
Figure 5.2: (a) Distributed harmonic generation principle similar to (b) distributed amplification.

upper lines during the propagation only if the fundamental and harmonic components are phase-matched. This is very similar to the principle of distributed amplification, in which phase matching between the two lines is necessary to achieve a gain that is proportional to the section number [20].

To analyze the harmonic generation on the nonlinear transmission line, we apply Kirchhoff's law at one section of the line and use approximated partial derivatives with respect to distance x from the beginning of the line, as shown in Fig. 5.1 [13]. This results in the wave equation for the voltage on the line $V(x, t)$ as

$$\frac{\partial^2 V}{\partial x^2} = L\frac{\partial}{\partial t}\left[C(V)\frac{\partial V}{\partial t}\right] + 2\sqrt{LC_0}\alpha\frac{\partial V}{\partial t} \tag{5.1}$$

where

$$\alpha = \frac{1}{2}\left(GZ_0 + \frac{R}{Z_0}\right) \tag{5.2}$$

and L, C, G, and R are unit length inductance, capacitance, parasitic conductance, and parasitic resistance, respectively. Z_0 is the characteristic impedance for zero-biased varactors, which is $\sqrt{L/C_0}$. We also approximate the nonlinear capacitors with a first-order function $C(V) = C_0(1 + bV)$ where b is the slope of C/V characteristic. Next, we apply a sinusoidal signal at ω_0 to the left end of the transmission line and use the Fourier series to find the steady-state solution as

$$V(x, t) = \sum_{n=1}^{3}[V_n(x)e^{jn\omega_0 t} + V_n^*(x)e^{-jn\omega_0 t}], \tag{5.3}$$

where "*" represents complex conjugate and V_n is the voltage of the nth harmonic. In (5.3), for simplicity it is assumed that the maximum generated harmonic component is the third. This assumption is valid if we introduce an ideal dispersion-less low-pass filter with the cut-off frequency around the fourth harmonic in each section of the line. In a real scenario, this filtering can be done

by adjusting the Bragg frequency of the transmission line. However, this introduces dispersion into the line, which will be discussed in Section 5.2.1.

Substituting (5.3) into (5.1), we obtain three traveling-wave equations for V_n's as

$$\frac{\partial^2 V_1}{\partial x^2} - \gamma_1^2 V_1 = -b\omega_0^2 LC_0[V_2 V_1^* + V_3 V_2^*] \tag{5.4a}$$

$$\frac{\partial^2 V_2}{\partial x^2} - \gamma_2^2 V_2 = -b\omega_0^2 LC_0[2V_1^2 + 4V_3 V_1^*] \tag{5.4b}$$

$$\frac{\partial^2 V_3}{\partial x^3} - \gamma_3^2 V_3 = -b\omega_0^2 LC_0[9V_1 V_2], \tag{5.4c}$$

where γ_n is the complex propagation constant for $n\omega_0$, given by

$$\gamma_n^2 = 2j\sqrt{LC_0}\alpha(n\omega_0) - (n\omega_0)^2 LC_0. \tag{5.5}$$

Equation (5.5) can be approximated as

$$\gamma_n = \sqrt{-\beta_n^2(1 - j2\alpha/\beta_n)} \simeq j\beta_n(1 - \tfrac{j}{2Q_n}), \tag{5.6}$$

where $\beta_n = n\omega_0\sqrt{LC_0}$ is the propagation constant for the nth harmonic in the absence of dispersion, and $Q_n = \beta_n/2\alpha \gg 1$ is the quality factor of the line for the nth harmonic. The propagation velocity for the nth harmonic is

$$v_{p,n} = \frac{n\omega_0}{\beta_n} = \frac{1}{\sqrt{LC_0}}. \tag{5.7}$$

Equation (5.7) shows that all harmonics are phase-matched, since the propagation velocity is the same for all frequencies due to the continuous line approximation. In other words, we have neglected the dispersion of the line due to discreteness, which will be discussed in the next section.

To solve (5.4), we use the perturbation theory and expand V_n in terms of b using coefficients V_{nm} up to the second order:

$$V_n = \sum_{m=0}^{2} b^m V_{nm} = V_{n0} + bV_{n1} + b^2 V_{n2} \tag{5.8}$$

121

By substituting (5.8) into (5.4) and sorting by the powers of b

For b^0,

$$\frac{\partial V_{10}^2}{\partial x^2} - \gamma_1^2 V_{10} = 0 \tag{5.9}$$

For b^1,

$$\frac{\partial V_{21}^2}{\partial x^2} - \gamma_2^2 V_{21} = -2\beta_1^2 V_{10}^2 \tag{5.10}$$

For b^2,

$$\frac{\partial V_{32}^2}{\partial x^2} - \gamma_3^2 V_{32} = -9\beta_1^2 V_{10} V_{21}, \tag{5.11}$$

where we applied boundary condition $V_2(x = 0) = V_3(x = 0) = 0$ which results in $V_{20}(x) = V_{22}(x) = V_{30}(x) = V_{31}(x) = 0$. From (5.9), we can obtain a traveling-wave solution given by

$$V_{10}(x) = V_{10}(0)e^{-\gamma_1 x} \tag{5.12}$$

and plug this into the equation for V_{21} in (5.10) to study the second order harmonic generation:

$$\frac{\partial V_{21}^2}{\partial x^2} - \gamma_2^2 V_{21} = -2\beta_1^2 V_{10}^2(0)e^{-2\gamma_1 x}, \tag{5.13}$$

which shows that the square of the voltage at the fundamental frequency is a forcing function for the wave equation of the second harmonic.

Using the boundary conditions $V_2(x = 0) = V_2(x = \infty) = 0$ (beginning of the line and the effect of loss at infinity), the solution of (5.13) is calculated as

$$V_{21}(x) = -\frac{2\beta_1^2 V_{10}^2(0)}{2\gamma_1 + \gamma_2} \left[\frac{e^{-(2\gamma_1 - \gamma_2)x} - 1}{2\gamma_1 - \gamma_2} \right] e^{-\gamma_2 x}. \tag{5.14}$$

Based on (5.6), (5.14) can be simplified to

$$|V_{21}(x)| = \frac{\beta_1 V_{10}^2(0)}{2} x e^{-\alpha_2 x}. \tag{5.15}$$

Equation (5.15) shows that the coherent addition at each section results in a linear increase of the second harmonic component with respect to distance x, while the transmission line loss causes an exponential decay. The maximum amplitude of the second harmonic is

$$V_2|_{max} = b|V_{21}(x_{opt})| = \frac{bQ_2}{2e} V_{10}^2(0), \tag{5.16}$$

where $x_{opt} = 1/\alpha_2$ is the length of transmission line that maximizes the second harmonic. We can also calculate the equivalent optimum phase shift as $\phi_{2,opt} = \beta_2 x_{opt} = 2Q_2$, which is a function only of the line quality factor.

Similarly, we calculate the third order harmonics from (5.11). It is interesting that the forcing function is the mixing term between V_{10} and V_{21}, which shows that cascading second-order nonlinearity generates the third-order harmonics without the third-order nonlinearity. By inserting (5.12) and (5.14) into (5.11) with the boundary condition $V_3(x = 0) = V_3(x = \infty) = 0$, we have

$$|V_{32}(x)| = \frac{3\beta_1^2 V_{10}^3(0)}{8} x^2 e^{-\alpha_3 x}. \tag{5.17}$$

This result shows that the third-order harmonics are proportional to x^2. When $x = x_{opt} = 2/\alpha_3$ or the propagation phase shift is $\phi_{3,opt} = \beta_3 x_{opt} = 4Q_3$, (5.17) has its maximum of

$$V_3|_{max} = b^2|V_{32}(x_{opt})| = -\frac{2(bQ_3)^2 V_{10}^3(0)}{3e^2}. \tag{5.18}$$

Equation (5.18) shows greater dependence on the nonlinearity, loss, and input amplitude, compared with the second harmonic generation in (5.16).

5.2.1 Dispersion Effect

So far, we have approximated the line with a continuous line and neglected the effect of dispersion that arises from the discreteness of the line. However, in a real transmission line with lumped varactors, the dispersion changes phase velocity with respect to frequency, especially close to the cut-off frequency. In the presence of the dispersion, equation (5.14) for the second harmonic becomes

$$V_{21}(x) = -\frac{\beta_1 V_{10}^2(0)}{2} e^{-j\Delta\beta_2 x/2} sinc(\Delta\beta_2 x/2) x e^{-\gamma_2 x}, \tag{5.19}$$

where $2\gamma_1 - \gamma_2$ is approximated as $j\Delta\beta_2 = j(2\beta_1 - \beta_2)$ using (5.6). Here, $\beta_2 \neq 2\beta_1$ due to the phase mismatch caused by dispersion. Equation (5.19) is proportional to the sinc function of the accumulated phase mismatch $\Delta\beta_2 \cdot x$. When $\Delta\beta_2 \cdot x$ increases, the sinc function decreases from unity, decreasing the amplitude of the second harmonic. If $\Delta\beta_2 \cdot x = 2\pi$, the amplitude of the second harmonic becomes zero. The dispersion degrades the third harmonic generation even more severely since the third harmonic is closer to the cut-off frequency.

5.2.2 Simulation Results

Fig. 5.3 shows the Cadence simulation of harmonic generation on the nonlinear transmission line, compared with our analysis in the presence of dispersion. The simulations are performed using a standard 0.13-μm CMOS process. Accumulation-mode MOS varactors and ground-shielded coplanar waveguides are used as varactors and inductors, respectively. For the input frequency of 25 GHz, the line is designed to have a cut-off frequency of 80 GHz to suppress any harmonics that are higher than the third one. In this simulation, the character-
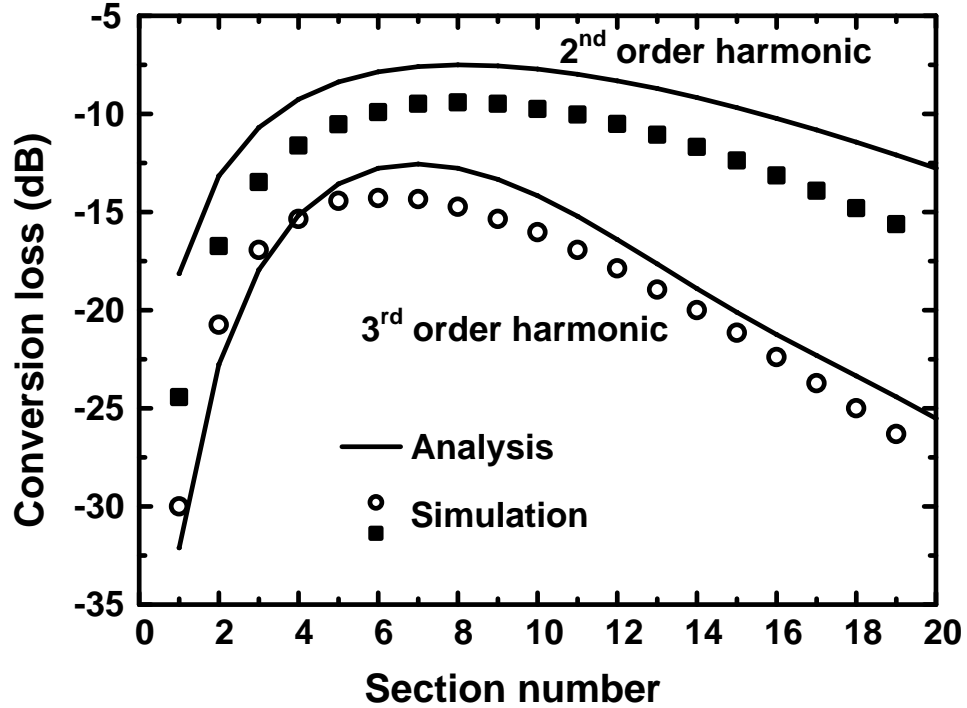
124

Figure 5.3: Simulated 2nd and 3rd harmonic generation on the nonlinear transmission line in comparison with the analysis.

istic impedance of the line is around 20 Ω and the input power at 25 GHz is 3.5 dBm.

As shown in Fig. 5.3, the optimum length of the transmission line for maximum harmonic generation is only around 6 sections. Furthermore, the best conversion losses at the second and third harmonics are higher than 10 dB. This is because of two major challenges. First, since the quality factor of the CMOS nonlinear transmission line is low, the optimum length is short according to (5.16) and (5.18). In other words, before enough harmonic power is generated, the effect of loss becomes dominant. The second challenge is dispersion that degrades the harmonic generation due to the phase mismatch. As we can see from Fig. 5.3, the loss and phase mismatch have greater influence on the third har-
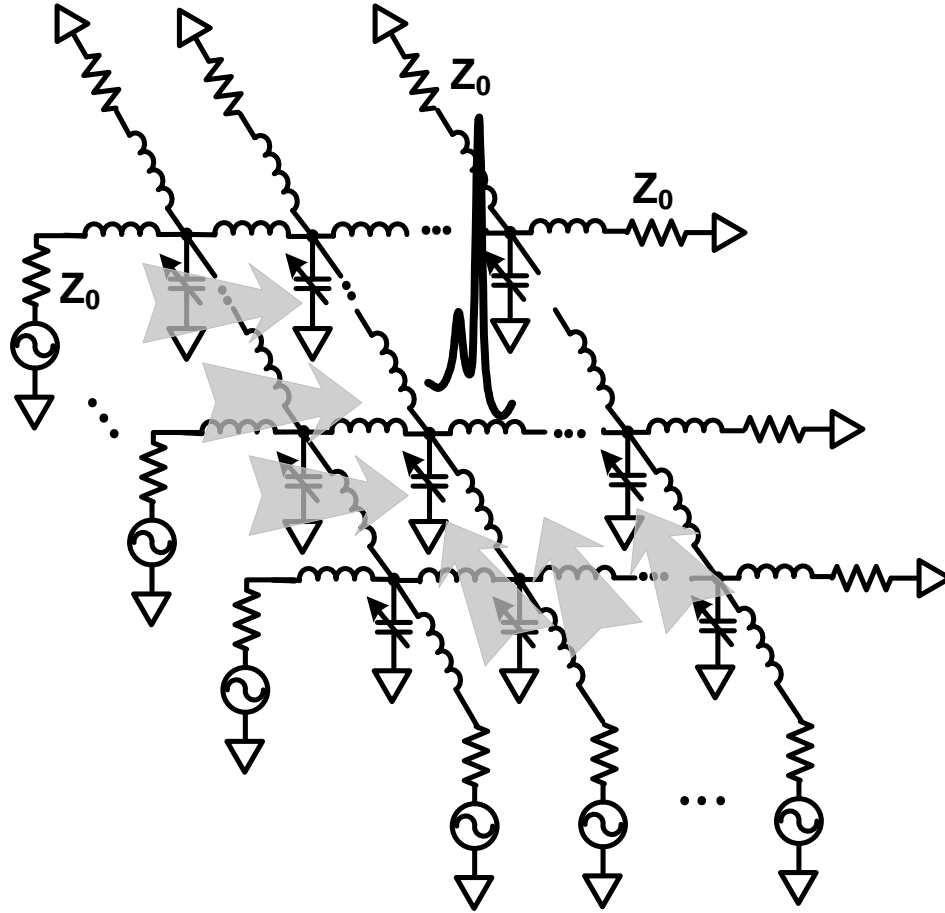
Figure 5.4: Proposed nonlinear LC lattice as a two-dimensional extension of a nonlinear transmission line.

monic, as it is closer to the cut-off frequency. This example demonstrates that the high loss and phase mismatch of the nonlinear transmission line in CMOS lowers the efficiency of the harmonic conversion. This limits the minimum pulse width and amplitude that can be generated using this structure.

5.3 Nonlinear Lattice for Sharp Pulse Generation

For a given quality factor, input amplitude, and varactor nonlinearity, we can significantly increase harmonic generation by extending a nonlinear transmission line to a two-dimensional nonlinear lattice as shown in Fig. 5.4. A series of in-phase sinusoidal sources are applied to the left and bottom of the lattice, generating two incident perpendicular plane waves. The top and right boundaries are terminated with matched resistors. These two waves interact diagonally to produce high-amplitude, sharp pulses at the center of the lattice. The lattice improves the harmonic generation by three mechanisms: (a) spatial power combining, (b) higher cut-off frequency, and (c) nonlinear constructive interference to generate more harmonics from each traveling wave. Next, we discuss these three effects that result in sharper and higher-amplitude pulses.

Figure 5.5 shows the simulated voltage amplitude of different points of the lattice as a plane wave propagates from the left to the right in a 12×12 lattice. The input amplitude is 1 V_{pp} at 20 GHz, and the inductors and capacitors are 80 pH and 200 fF, respectively. The propagation of the plane wave in the lattice is similar to wave propagation in a transmission line. However, the simulation results show that the plane wave has the maximum amplitude of 1.5 V_{pp} after six sections, which is 25-% larger than the maximum amplitude in a nonlinear transmission line with the same component values.

Spatial Power Combining This voltage increase is partly due to the spatial combining mechanism inside the lattice. In the previous simulation in Fig. 5.5, since the top and bottom boundaries are terminated with matched resistors, the effective shunt impedance of the lattice closer to its boundaries is lower. As
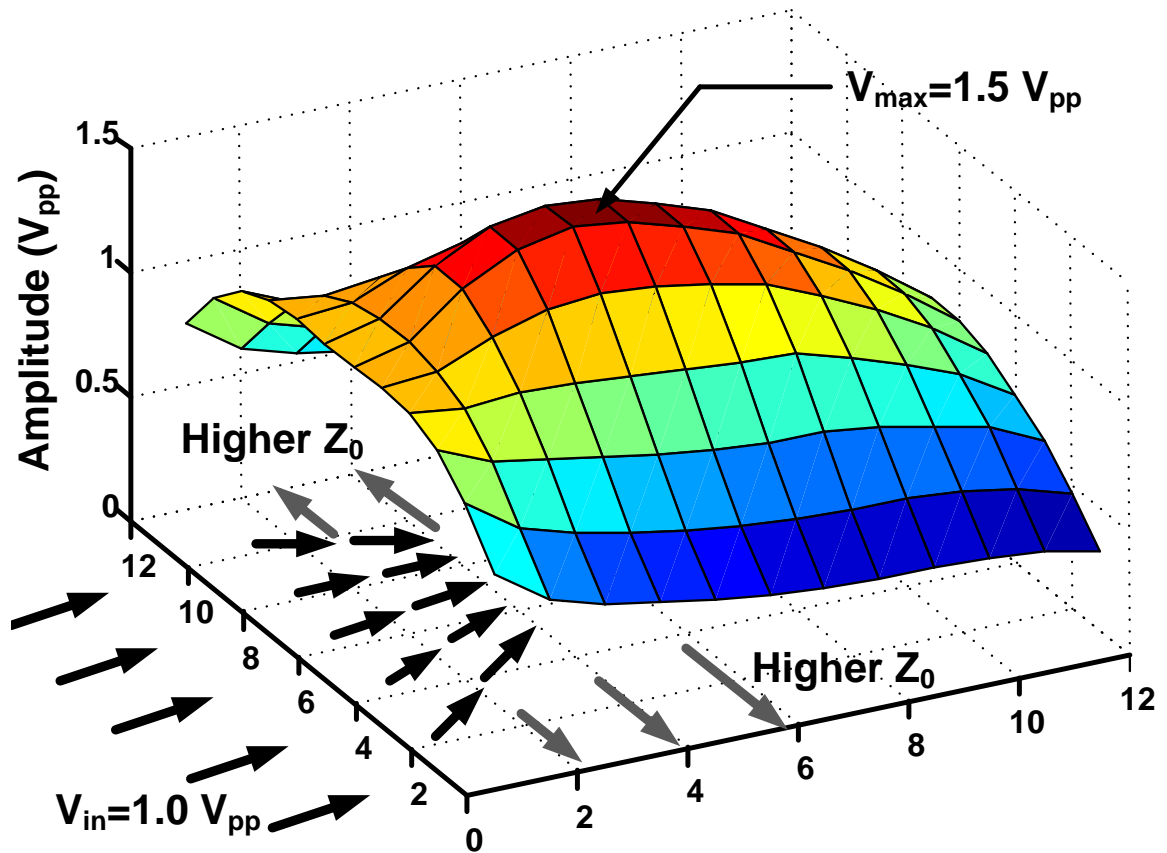
Figure 5.5: Simulated voltage amplitude of different points of a 12×12 non-linear lattice driven by a plane wave propagating from the left to the right. The top, bottom, and right boundaries are terminated with matched loads.

shown in Fig. 5.5, this results in higher characteristic impedance at the top and bottom, which pushes some of the signal to the center of the lattice where the characteristic impedance is relatively lower.

Higher Cut-Off Frequency   In addition, the lower characteristic impedance at the center of the lattice creates some diagonal wave component. For a plane wave that propagates diagonally, the cut-off frequency of the lattice is

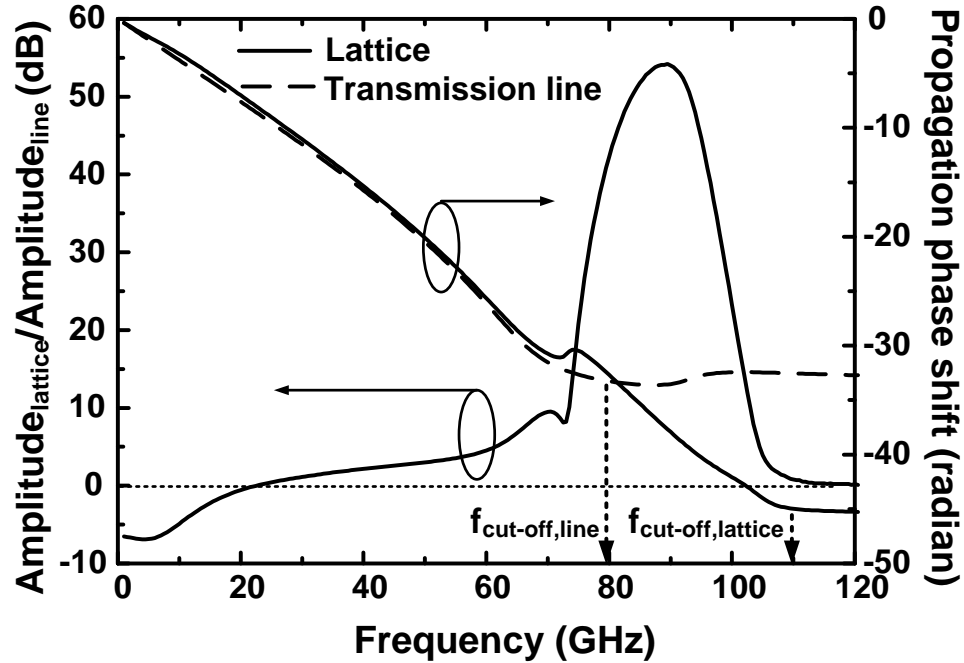$$\omega_{c,diagonal} = \frac{2\sqrt{2}}{\sqrt{LC}},$$
(5.20)

Figure 5.6: Simulated amplitude and phase response of the lattice compared with the line.

which is higher than the cut-off frequency of the transmission line with the same L and C by a factor of $\sqrt{2}$ [21]. This higher cut-off frequency improves the phase matching and loss for higher frequency components.

To summarize these two effects, Fig. 5.6 shows the small-signal response of the lattice and a transmission line with the same values of L and C. The amplitude and propagation phase shift are simulated at the middle node when the input is applied only to the left. As shown in Fig. 5.6, the signal amplitude in the lattice is higher than the transmission line for frequencies higher than 20 GHz due to the power-combining effect. After 70 GHz, the lattice shows significantly larger voltage amplitude due to its higher cut-off frequency. This higher cut-off frequency also results in better phase matching in the lattice at above 70 GHz.
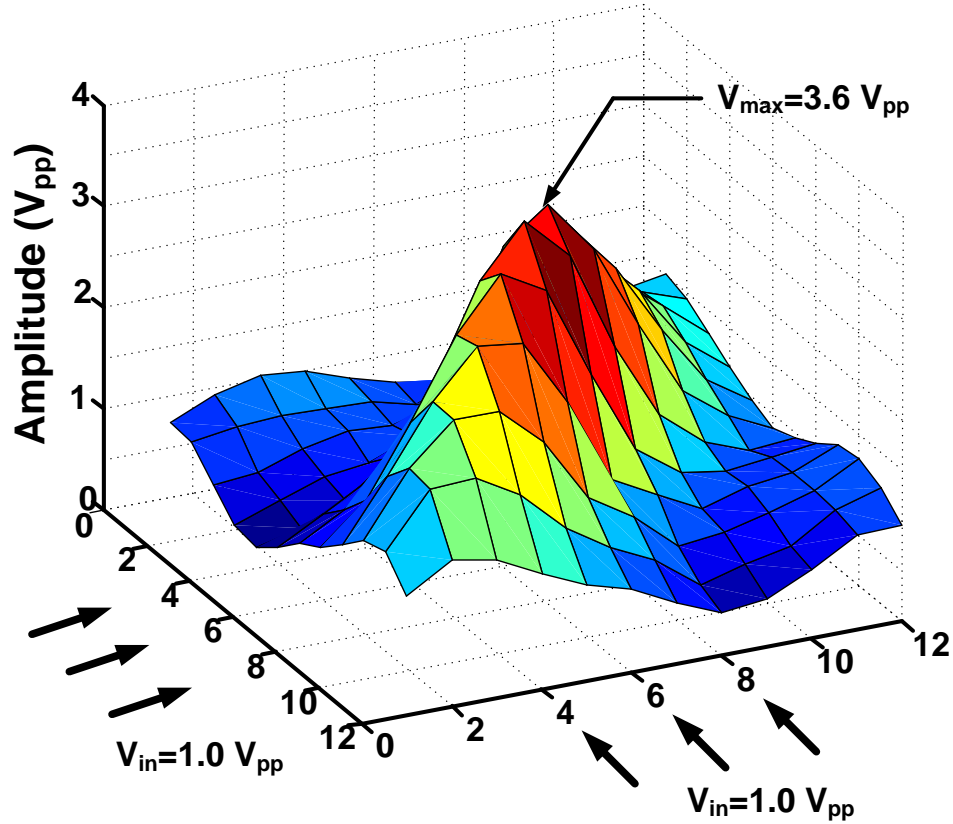
Figure 5.7: Nonlinear constructive interference in a 12×12 nonlinear lattice.

Nonlinear Constructive Interference   Next, we add the second plane wave to the bottom of the lattice as shown in Fig. 5.7. The two waves interact nonlinearly, which means that the amplitude of the generated pulse is more than the sum of two incoming waves despite its passive structure. This is because the nonlinear interaction focuses the energy both in time and space, resulting in higher localized power. This phenomenon has been observed in plasma and fluid mechanics [22] and more recently in the simulation of the discrete LC lattices [15]. Figure 5.7 shows the maximum amplitude of 3.6 V_{pp}, which is more than twice of the maximum amplitude of each plane wave.

   To compare the lattice performance to a nonlinear transmission line, we sim-
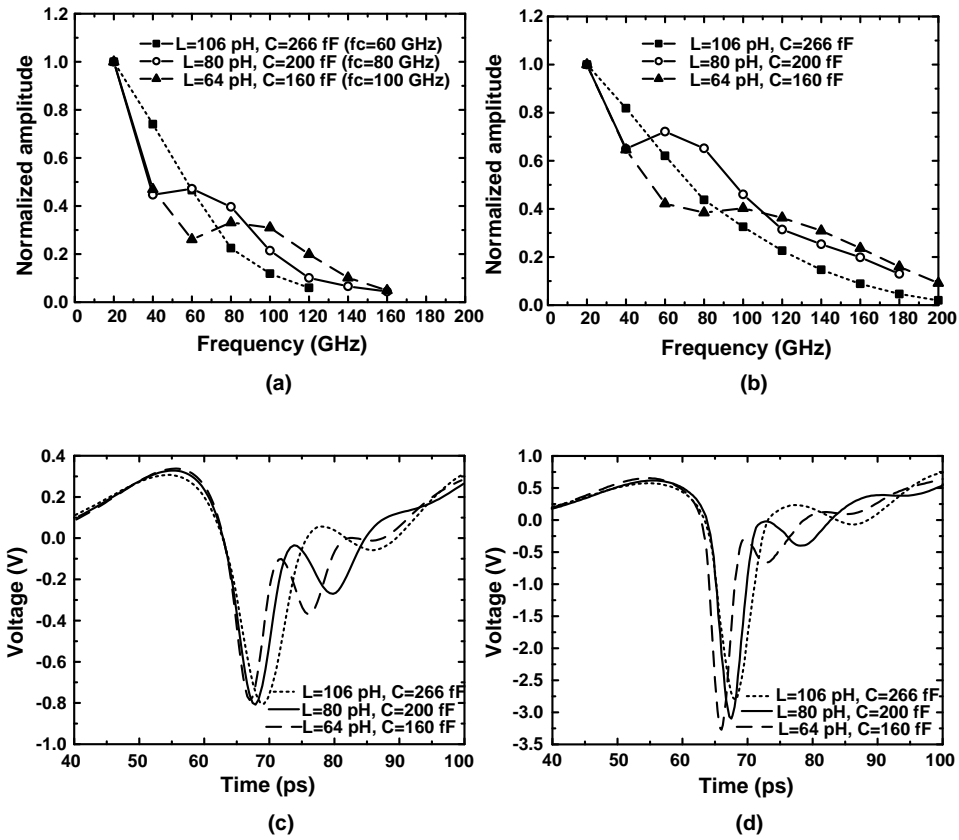
Figure 5.8: Simulated output spectrum for (a) the transmission line and (b) the lattice, and time-domain response for (c) the transmission line and (d) the lattice.

ulate both structures with different cut-off frequencies for a given propagation phase shift (i.e., the same effective electrical length) as shown in Fig. 5.8. The input frequency and amplitude are set at 20 GHz and 500 mV, respectively. The input source impedance and termination resistance are matched to the characteristic impedance. Figures 5.8(a) and (b) show the spectrum of the output normalized to the amplitude of the input frequency for the transmission line and the lattice, respectively. As shown here, the lattice has significantly higher harmonic components due to the spatial combining, better phase matching, and nonlinear wave interaction. Figures 5.8(c) and (d) show the output waveforms

of the transmission line and the lattice, respectively. The lattice has higher amplitude at all harmonics that results in a much sharper pulse with higher amplitude. The output amplitude of the lattice is around four-times higher than that of the transmission line. Finally, since the lattice output has more high frequency components, it approaches a single pulse.

5.4   Lattice Design in CMOS

In this section, we overview the design of a nonlinear lattice in a standard 0.13-μm CMOS technology.

5.4.1   Passive Elements

Accumulation-mode MOS varactors are employed as voltage-dependent capacitors that generate nonlinearity in the lattice. The nonlinearity is determined by C_{max}/C_{min} and the slope of the capacitance-voltage curve. In parallel with a bias-dependent capacitance and C_{ox}, parasitic capacitances exist due to fringing fields and poly and drain/source overlap, degrading the capacitance nonlinearity. Hence, the channel length L_{ch} and width W_{ch} should be sufficient to minimize the portion of parasitics to the total capacitance. On the other hand, the varactors are the dominant source of loss in the lattice for frequencies higher than 50 GHz, and hence their quality factor needs to be maximized.

Figure 5.9 shows the simulated varactor capacitance as well as its quality factor as a function of the bias voltage for different channel lengths. In this simulation, the signal frequency is 20 GHz, and the capacitance at zero bias
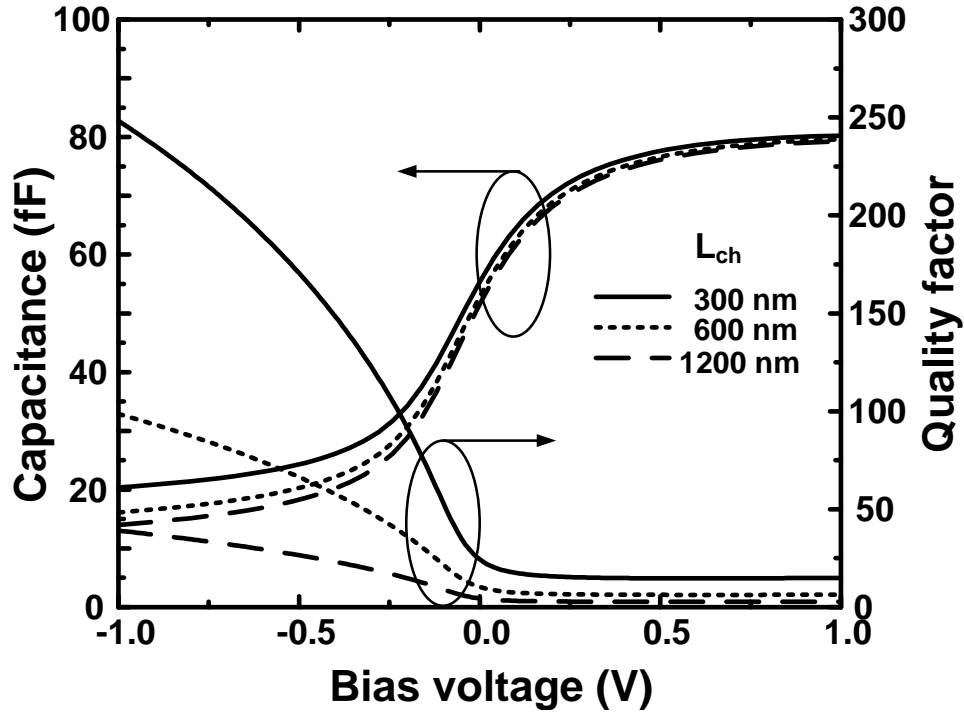
Figure 5.9: Varactor capacitance and quality factor vs. bias voltage

(C_0) is kept constant. When L_{ch} increases, C_{max}/C_{min} increases due to the lower portion of parasitics. However, the increase in L_{ch} also decreases the quality factor since the bias-dependent channel resistance R_{ch} is proportional to L_{ch}, as illustrated in Fig. 1.7. From the simulation, we found that the optimum channel width and length are 1.5 μm and 0.3 μm, respectively. These values result in nonlinearity of $b \simeq 2 \; V^{-1}$ and a quality factor of $\sim$ 10 at 50 GHz.

The lattice inductors are implemented using a coplanar waveguide with ground shielding [26]. The signal and ground lines are on the top metal layer (a 4-μm aluminum layer), and the ground shield is made of the bottom metal. The individual inductors as well as their coupling are simulated using an E/M simulator, SONNET. Figure 5.10 shows the simulated quality factors of stand-alone inductors and varactors for a range of frequencies.
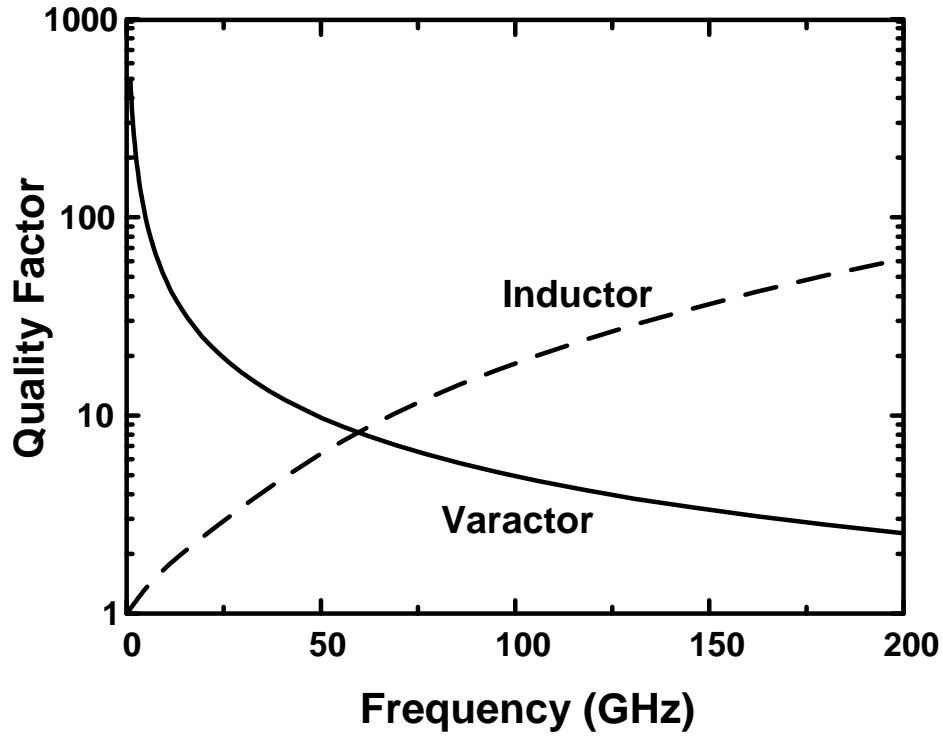
Figure 5.10: Quality factor of the employed inductor and varactor vs. frequency

5.4.2 Optimization and Simulation

The design parameters of the lattice are the cut-off frequency, the size, and the characteristic impedance. For a given input frequency of 20 GHz, the cut-off frequency of 110 GHz is selected from Fig. 5.8, considering the trade-off among the pulse width, the amplitude, and the side peak. Then, to determine the optimum size, we simulate the lattice for different sizes as shown in Fig. 5.11. As the lattice size increases, the signal travels longer, resulting in higher harmonic generation. On the other hand, for lattices larger than 16×16, the loss becomes dominant, and the harmonic generation is degraded, as discussed in Section 5.2. Consequently, we select a 16×16 lattice for this design.
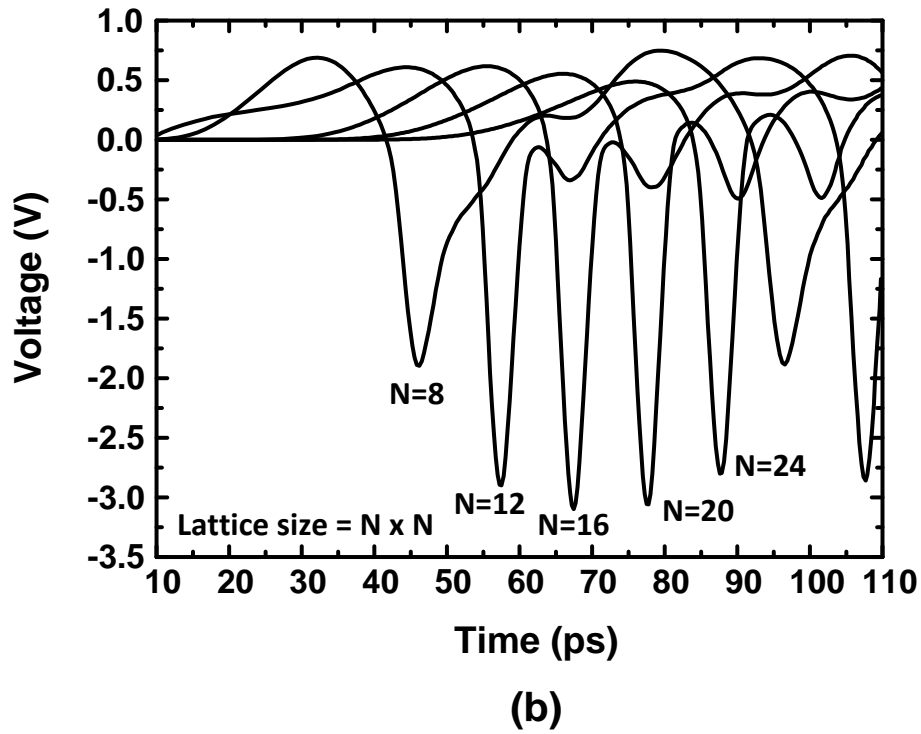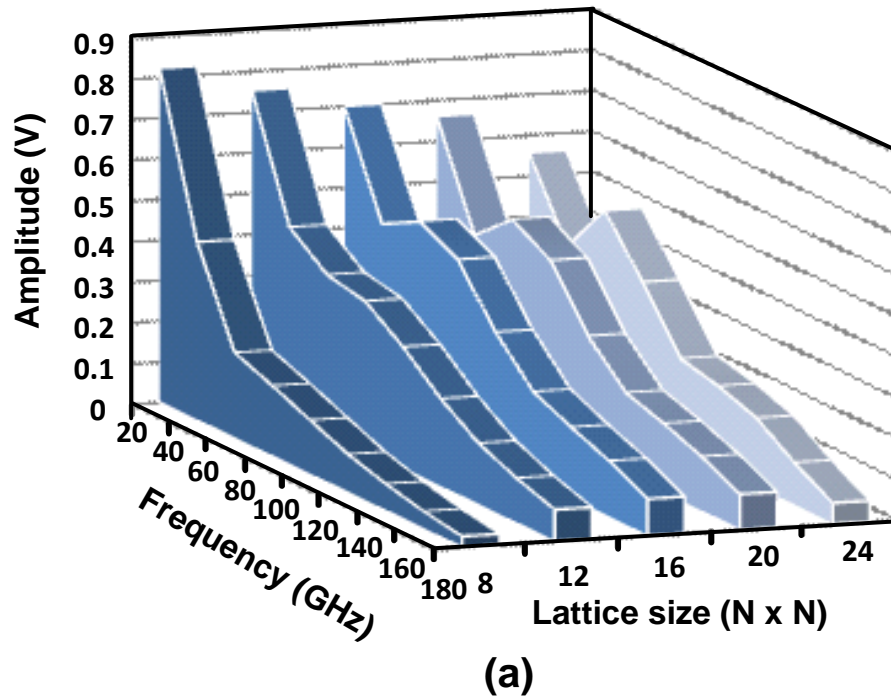
134

Figure 5.11: Lattice size optimization in (a) a frequency spectrum and (b) a time domain.

To determine the optimum characteristic impedance of the lattice, we observe that the output pulse is a result of interference between the two plane waves and is not a traveling wave. This means that ideally the load impedance at the center of the lattice should be much higher than the characteristic impedance to avoid the disturbance of the flow of two incoming waves. For values of inductors and capacitors that are integrable in CMOS, our simulation shows that the output pulse is narrower than 5 ps if the characteristic impedance is lower than 10 Ω for a 50-Ω load. This low characteristic impedance requires higher input power for a fixed input voltage amplitude to the lattice. To alleviate this effect, two nodes of the lattice are connected to the output instead of the center of the lattice, as shown in Fig. 5.12. Since these two symmetric points have the same voltage, the effective output load for each one of them is 100 Ω. This means that the characteristic impedance of the lattice can be increased to 20 Ω. This output configuration also halves the effective output parasitic capacitance C_p, which reduces the loading effect of the output pad. To easily probe the output and to reduce the chip area, the upper left quarter of the lattice is cut off, as shown in Fig. 5.16. With proper termination, this has no significant effect on the lattice performance.

Figure 5.13 shows the simulated boosting ratio and the pulse width with respect to the input amplitude for the designed 16×16 lattice and a 20-GHz input signal. The amplitude of the steady-state output signal nonlinearly depends on the amplitude of the input signal. We characterize this effect using the boosting ratio, defined as the ratio of output amplitude to input amplitude. As shown in Fig. 5.13, the higher input amplitude boosts the harmonic generation, resulting in higher boosting ratio and narrower pulse width. However, as the input amplitude becomes larger than ~ 0.5 V, the boosting ratio and the pulse width
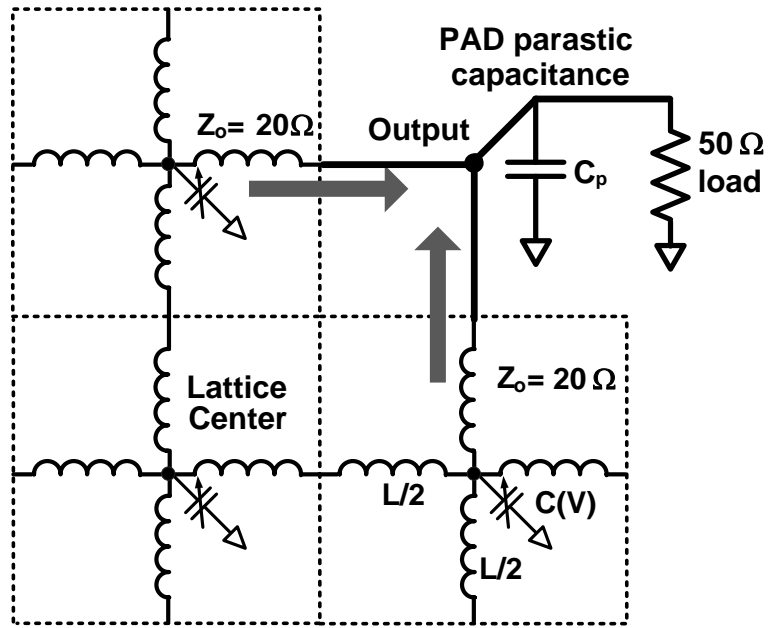
Figure 5.12: Output is connected to two symmetric adjacent nodes to the center of the lattice to minimize the output loading.
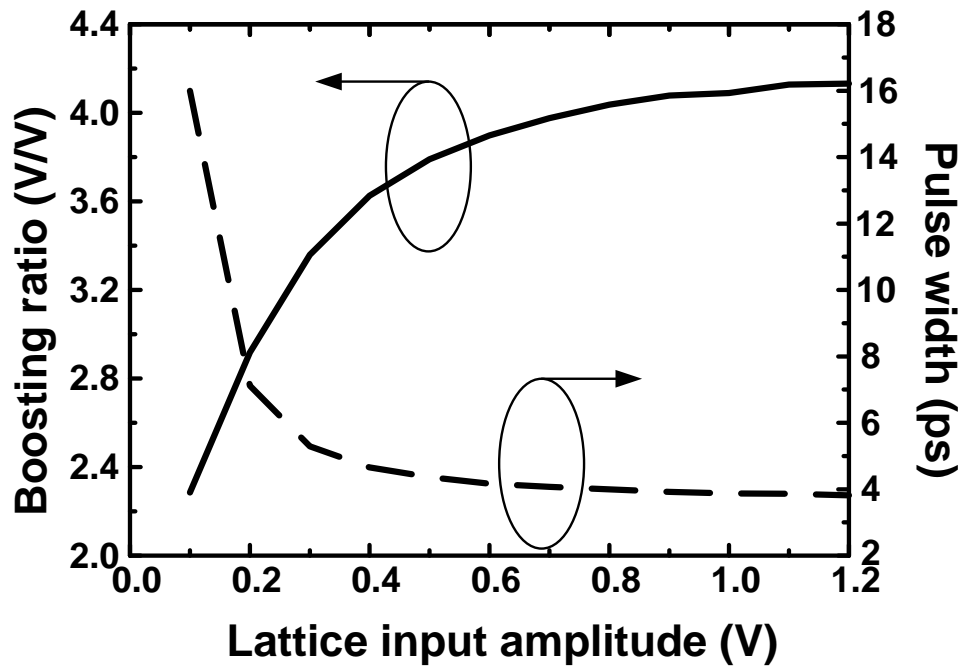

Figure 5.13: Simulated boosting ratio and pulse width vs. input amplitude for the 16 ×16 lattice.
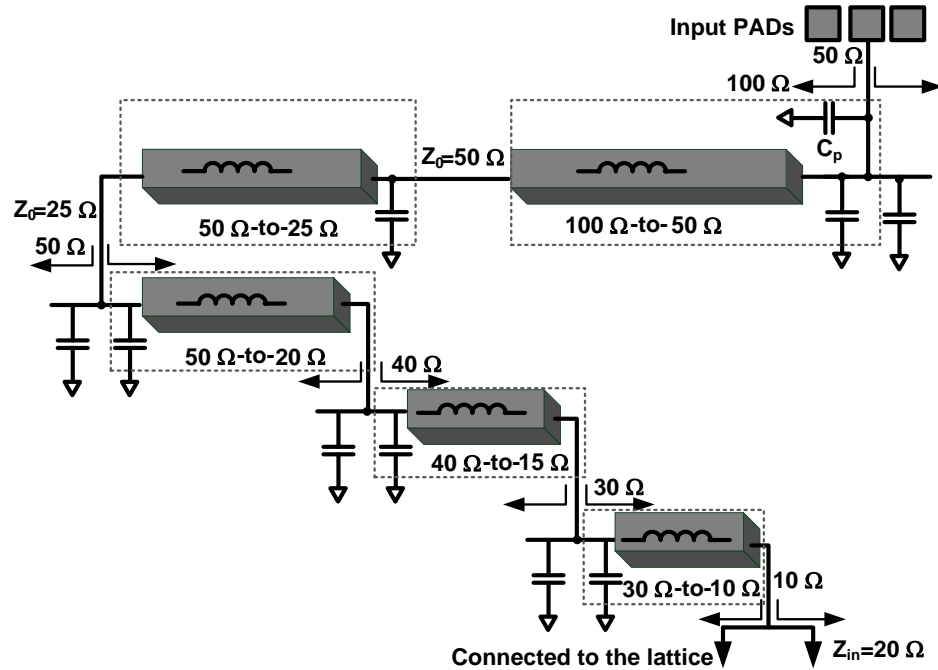
Figure 5.14: Distribution network from input to the lattice.

saturate to 4.1 V/V and 3.8 ps, respectively. This saturation occurs due to the varactor saturation, as shown in Fig. 5.9.

5.4.3 Distribution Network

Figure 5.14 shows the power divider that distributes input power into 32 ports in the left and bottom boundaries of the 16×16 lattice. The input impedance of 50 Ω is also transformed to 20 Ω, which is the characteristic impedance of the lattice. The power divider has a tree structure that consists of different L-matches at each division point. The impedance transformation ratios of all L-matches are not higher than three for the broad bandwidth. The input pad capacitance and the inductance of transmission lines of the distribution network are absorbed
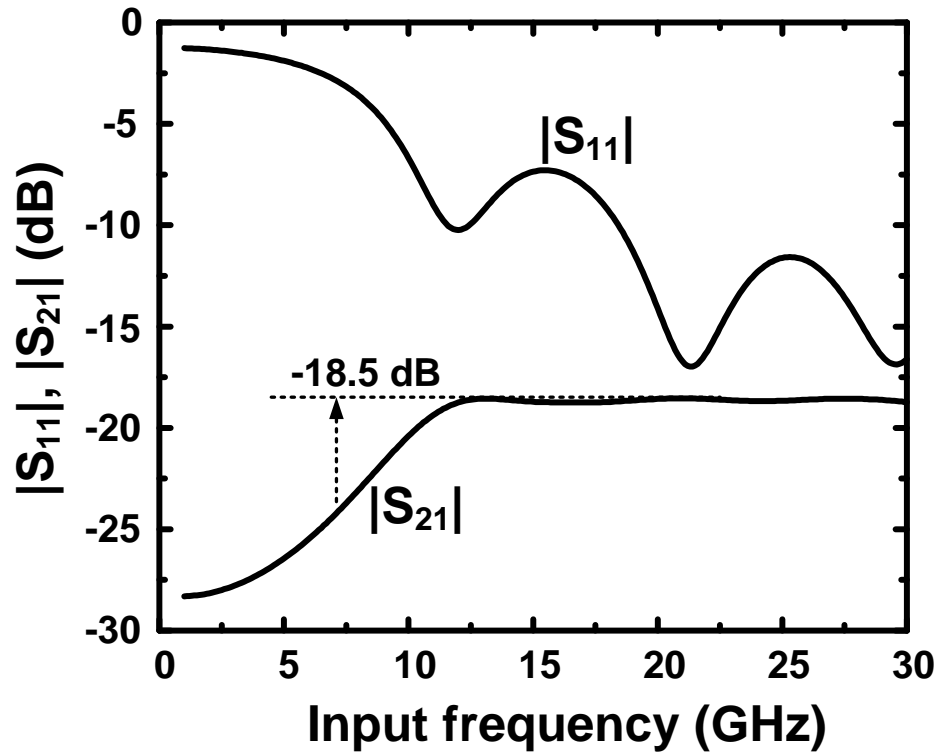
Figure 5.15: Simulated S-parameter of the distribution network.

into the matching network. Transmission lines are implemented with a coplanar waveguide to minimize the loss for a given inductance. The vertical natural capacitors (VNCAPs) are used as the matching capacitors [29]. Figure 5.15 shows the simulated S-parameter of the designed power divider when the output ports are connected to 20-Ω terminations. The $|S_{21}|$ is around -18.5 dB at around 20 GHz. Since the ideal loss for 32 divisions is $-20log(32) = -15$ dB, each L-match has an insertion loss of around 0.5 dB, considering that the signal passes through seven L-match networks. The power divider also has $|S_{11}|$ of below -10 dB at around 20 GHz.

Figure 5.16: Die photograph of the chip.
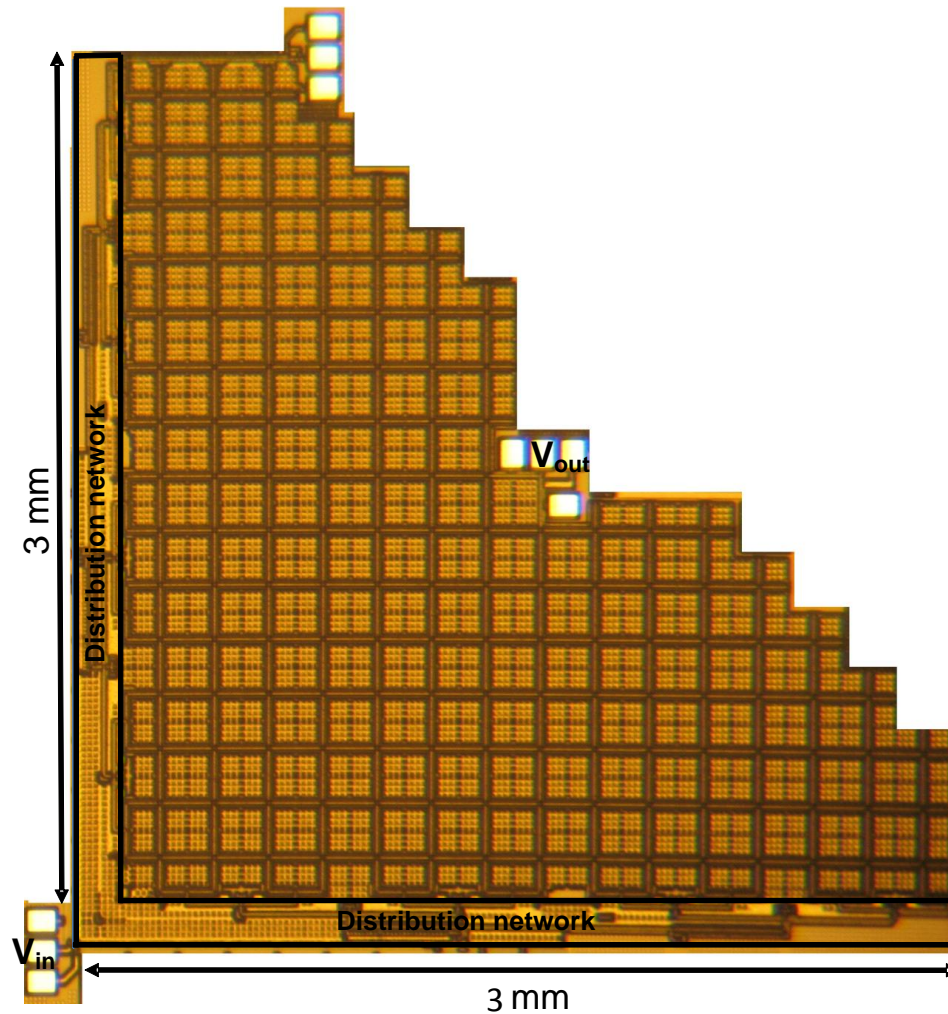
5.5 Measurement

A 15×15 lattice is fabricated in a standard 0.13-μm CMOS technology as shown in Fig. 5.16. The size of the chip is 3 mm×3 mm, including the distribution network and the lattice. As mentioned, to probe the center of the lattice, the upper left quarter of the lattice is cut off.

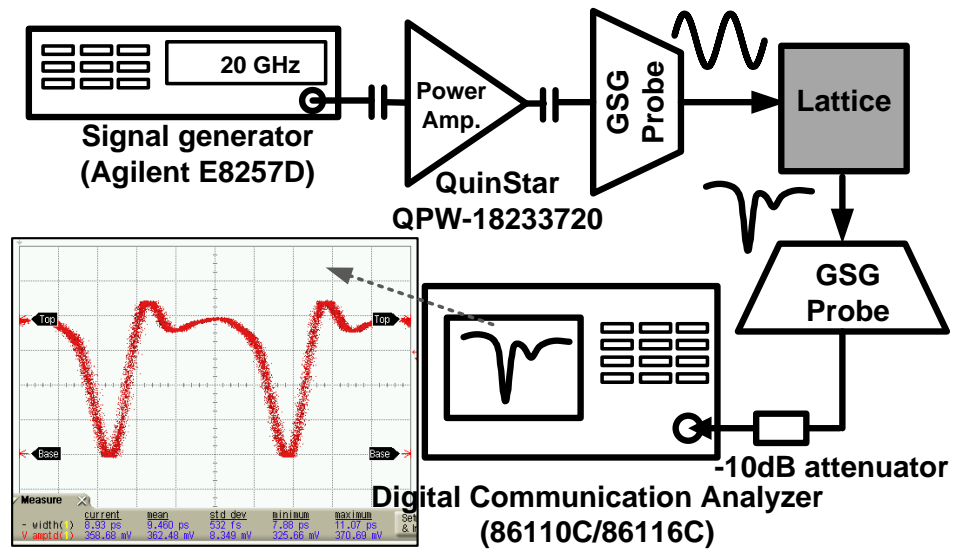Fig. 5.17 shows the experimental setup to measure the output waveform of

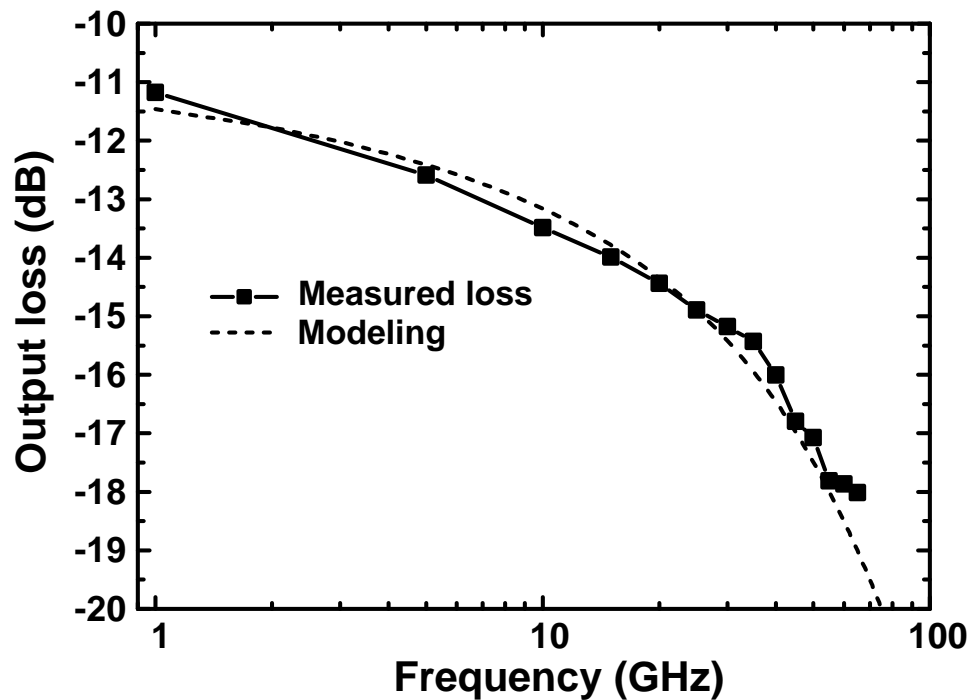Figure 5.17: Experimental setup.

Figure 5.18: Measured loss of the output test setup and its model.

the lattice. An external power amplifier, which has a 1-dB compression point of 34 dBm, is placed after the signal source to provide enough power into the distribution network. The input power level is controlled using the signal generator. Both input and output are connected using GSG probes. The output signal is attenuated and connected to an 80-GHz sampling oscilloscope. The loss of cables, connectors, and the attenuator is measured by a broadband signal generator, a spectrum analyzer, and the oscilloscope. The response of the oscilloscope is estimated from its user manual, which is based on the measurement by a wideband power meter [33]. The total loss of the output measurement setup including the oscilloscope is shown in Fig. 5.18. Since this loss is due mainly to the skin effect and limited bandwidth, we model the transfer function of the test setup as

$$H(j\omega) = 10^{-A/20} e^{-\alpha \sqrt{\omega}} / (1 + j\omega/\omega_B), \tag{5.21}$$

where ω_B is the bandwidth of the system, and α is a parameter that represents the loss of the cable, connectors, and pads. "A" is a frequency-independent attenuation that mainly results from the 10-dB attenuator in Fig. 5.17. To fit the measured loss with $|H(j\omega)|$, A and α are estimated to be 10.6 dB and 1.1×10^{-7}, respectively. Due to the limited bandwidth of the measurement setup, capturing the output pulse without distortion is very challenging. In simulation, the lattice output pulse has a significant power even at the 9th harmonic frequency around 180 GHz. For a conservative estimation of the output pulse amplitude, we first perform the Fourier analysis of directly measured waveform from the oscilloscope, and neglect the harmonic components beyond the electrical bandwidth of the oscilloscope. Then, output loss measured in Fig. 5.18 is compensated at each harmonic frequency in terms of magnitude and phase. Finally, we perform

the inverse Fourier transform to recover the waveform in the time domain.

When a 20-GHz sinusoid is applied into the lattice and its amplitude at the lattice input is around 1.3 V_{pp}, the measured output waveforms are shown in Figs. 5.19(a) and (b), before and after de-embedding the loss of the measurement setup, respectively. The lattice input amplitude is calculated from the input power and the simulated loss of the distribution network. Fig. 5.19(c) shows the measured frequency spectrum of the output pulse.

Next, we change both input frequency and amplitude, and measure the amplitude of the output pulse as shown in Fig. 5.20. For comparison, we also simulate the same lattice with linear capacitors. Since the nonlinearity is a function of signal amplitude, the output amplitude increases nonlinearly with the input amplitude. To quantify this nonlinear behavior, the boosting ratio, i.e., the ratio of output and input amplitudes, is also measured, as shown in Fig. 5.21. When the input amplitude is low and harmonic generation rarely occurs, the nonlinear lattice behaves much like the simulated linear lattice with the boosting ratio of 1.4 V/V. However, as the input amplitude increases, the boosting ratio increases up to 2.3 V/V. The increase in the boost ratio is saturated at an input amplitude of around 0.9 V_{pp} to 1 V_{pp} since the varactors saturate, as shown in Fig. 5.9. Another reason for this saturation is the bandwidth limitation of the test setup shown in Fig. 5.18. As the input amplitude increases, the generated signal has a higher portion of its energy above the cut-off frequency of the measurement setup.
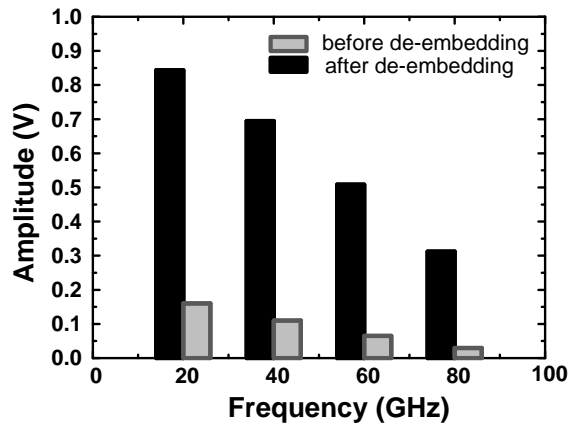
The pulse width is also measured in Fig. 5.22. As the input amplitude increases, the measured pulse width is reduced to 8 ps for an input frequency of 22 GHz. To investigate the minimum pulse width that can be measured with
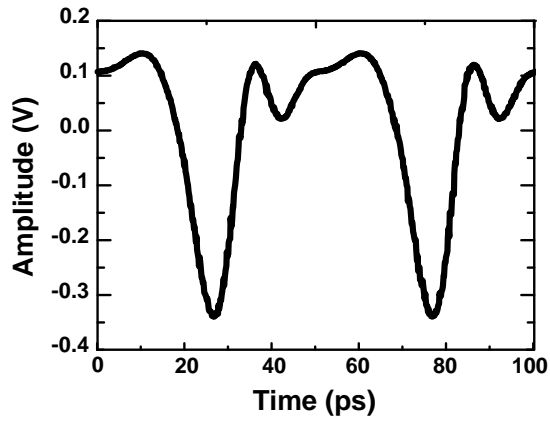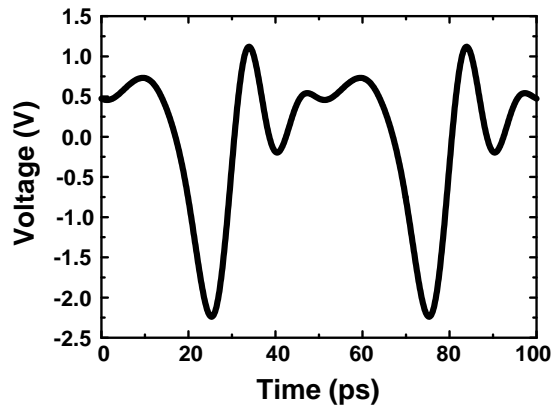
Figure 5.19: Measured output waveforms (a) before and (b) after de-embedding the loss of the measurement setup and (c) their frequency spectrum
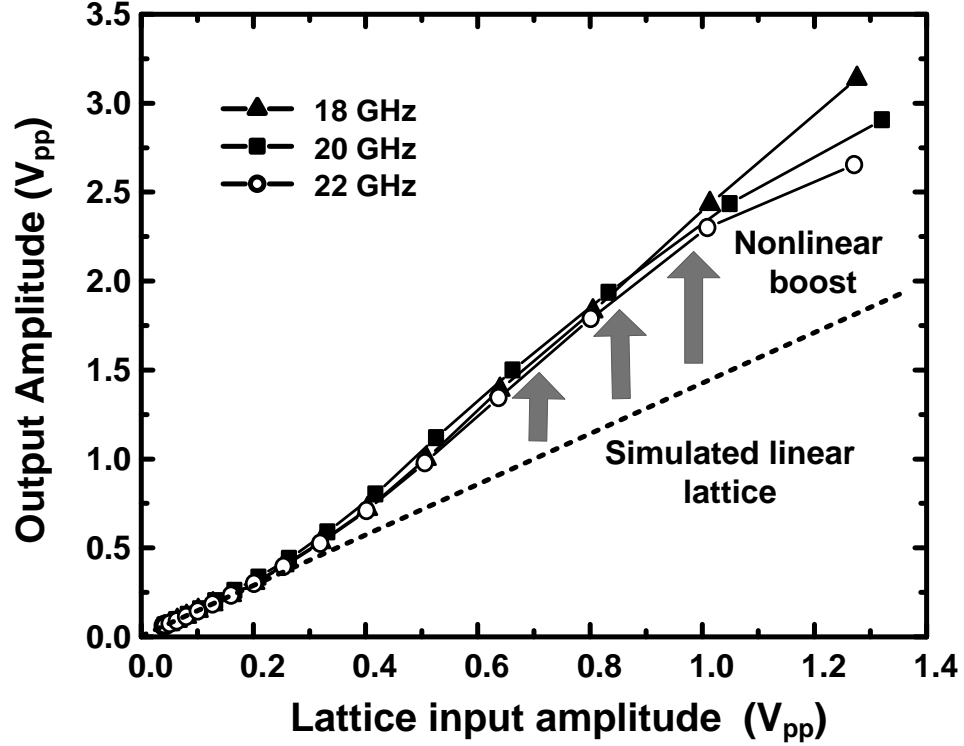
Figure 5.20: Measured output amplitude versus input amplitude for different frequencies.

our experimental setup, the 10-% - 90-% rise time is calculated based on the loss equation in (5.21). The calculated rise time is 7.2 ps, and, under the assumption that the waveform is symmetric, the minimum pulse width that can be measured in our setup is also around 7.2 ps. The actual pulse width can be estimated from the measured pulse width and the bandwidth of the setup as [34]

$$t_{meas} = \sqrt{t_{pulse}^2 + t_{system}^2},$$
(5.22)

where $t_{meas} = 9.6$ ps is the minimum measured pulse width before de-embedding the loss, $t_{system} = 7.2$ ps is the response of the system to an ideal impulse, and t_{pulse}
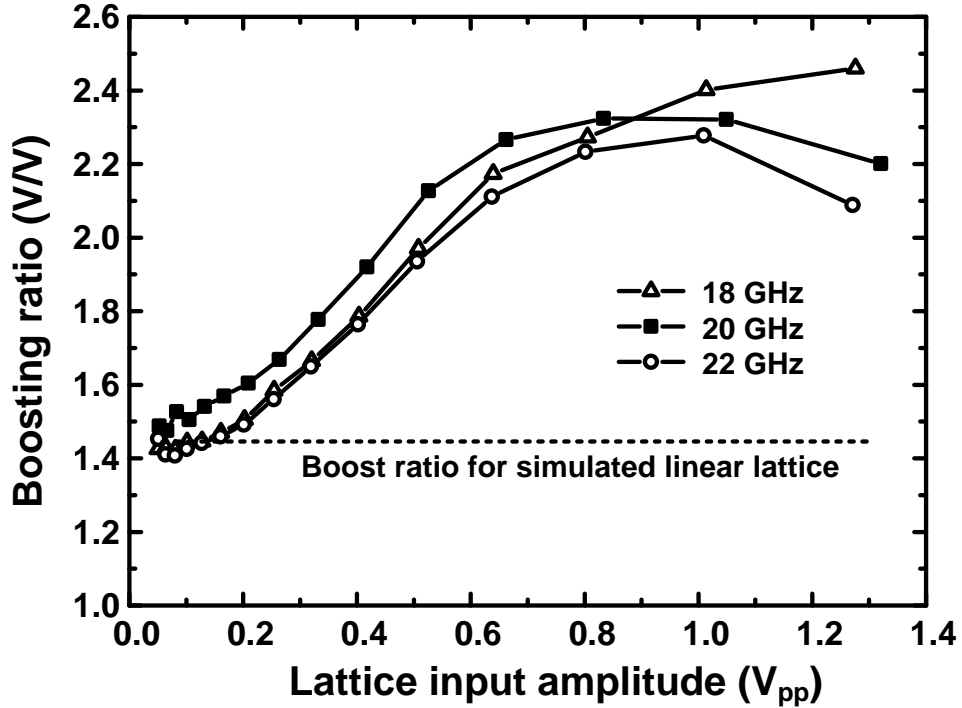
Figure 5.21: Measured boosting ratio versus input amplitude for different frequencies.

is the actual pulse width. Based on the measured results and (5.22), the actual pulse width is around 6.3 ps. To the best of our knowledge, this is the sharpest pulse with amplitude higher than 1 V in a CMOS process, as depicted in Table 5.1.

5.6   Discussion

In this section, we discuss the effect of high-order harmonics in a nonlinear lattice, which were neglected in the measurement. We also discuss a triangular lattice with a half size and the same performance using diagonal symmetry.

146
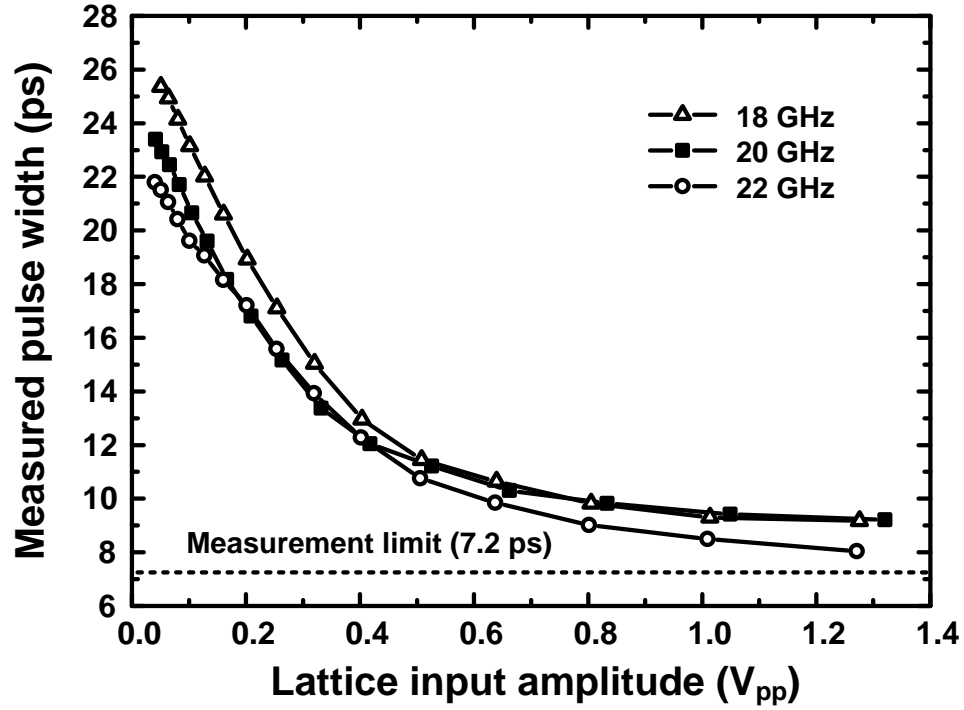
Figure 5.22: Measured pulse width suppression versus input amplitude for different frequencies.

Table 5.1: Comparison with prior art

	Pulse width (ps)	Duty cycle (%)	Amplitude (V_{pp})	Technology	Type
[12]	5.5	4.4	3.9	GaAs	Transmission line
[13]	23	21	0.95	0.18-μm BiCMOS	Transmission line
[18]	293	33	1.5	0.18-μm CMOS	Oscillator
[19]	16	30	0.5	GaAs	Oscillator
This work	**9.6 (6.3*)**	**21 (14*)**	**2.7**	**0.13-μm CMOS**	**Lattice**

Pulse width and duty cycle are measured directly from sampling-circuit or oscilloscope without de-embedding the bandwidth of the measurement setup.
* is the estimated value after de-embedding.

5.6.1 High-order Harmonics Consideration

We estimated the lattice performance based on the measurement that neglects higher harmonics than the fourth because of the equipment bandwidth limit. However, the simulation showed that a considerable portion of pulse power still exists beyond the fourth harmonics, which predicts that the amplitude is underestimated and the pulse width is overestimated in the measurement. To investigate the difference depending on the number of harmonics taken into account, Fig. 5.23 shows the simulation results when the input amplitude is $1V_{p-p}$ at 20 GHz. As more harmonics is taken into account, the amplitude increases and the pulse width decreases. As shown in Fig. 5.23, the boost ratio is increased by 0.9 V/V and the pulse width is significantly decreased from 8.6 ps to 4.8 ps when we include up to the tenth harmonics for the waveform recovery. Based on this analysis, we can estimate the pulse width of less than 4.8 ps from the measured pulse width of 8 ps when the input frequency and amplitude are 22 GHz and 1.3 V_{p-p}.

5.6.2 Half-size Triangular Lattice

Using diagonal symmetry, we can reduce the size of a rectangular lattice by folding it in the diagonal direction as shown in Fig. 5.24. After folding, inductance and capacitance at each node are changed into $L/2$ and $2C$ due to parallel combination except for diagonal boundary capacitors. Therefore, the characteristic impedance is reduced by half, while the cut-off frequency does not change. This means that the total input energy into a half-sized lattice is the same as a full-sized one, since input energy into each port is doubled to maintain the
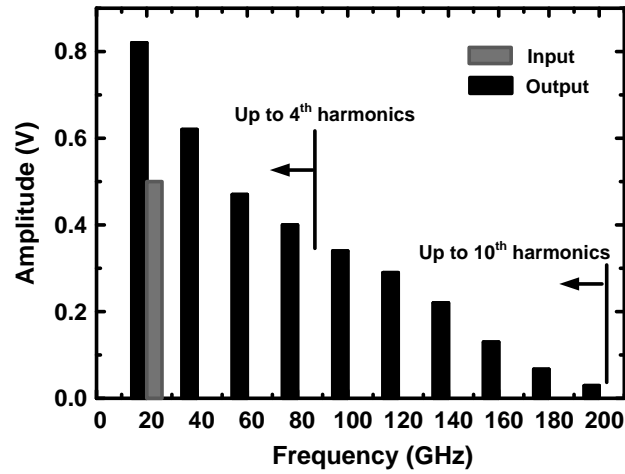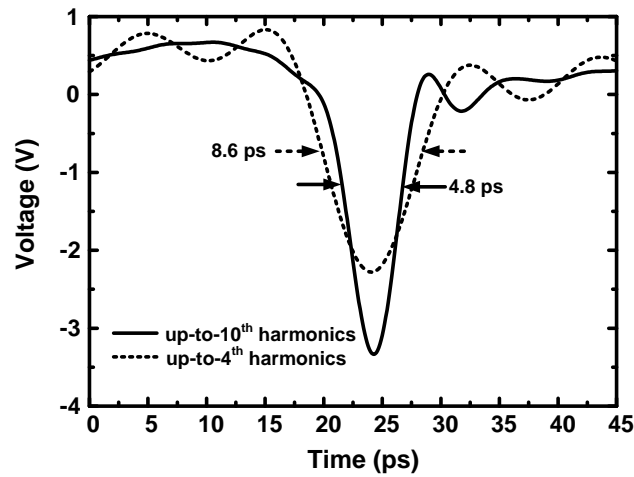
Figure 5.23: (a)Frequency and (b)time domain lattice output when we take into account up to fourth harmonics and tenth harmonics.

same input voltage amplitude but the number of input ports is halved. Fig. 5.25 shows the simulation result of amplitude profile in a 12×12 lattice for full-size and half-size ones. These two graphs demonstrate that a half-size triangular lattice exhibits the same amplitude as well as the same interference pattern as a full-size rectangular lattice for a given input energy.
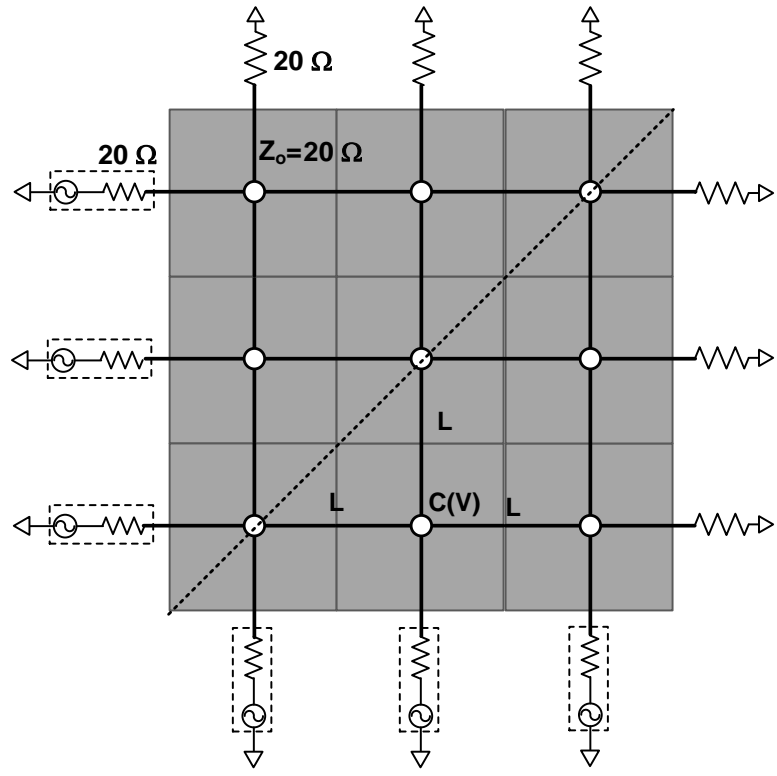
(a)
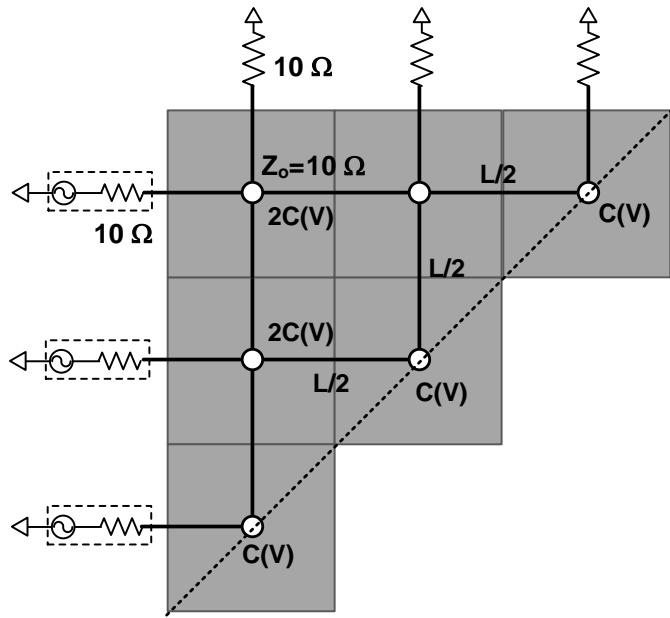
(b)

Figure 5.24: A full lattice (a) can be half-sized by folding it diagonally as shown in (b) due to diagonal symmetry without degrading the performance. 150

(a)

(b)
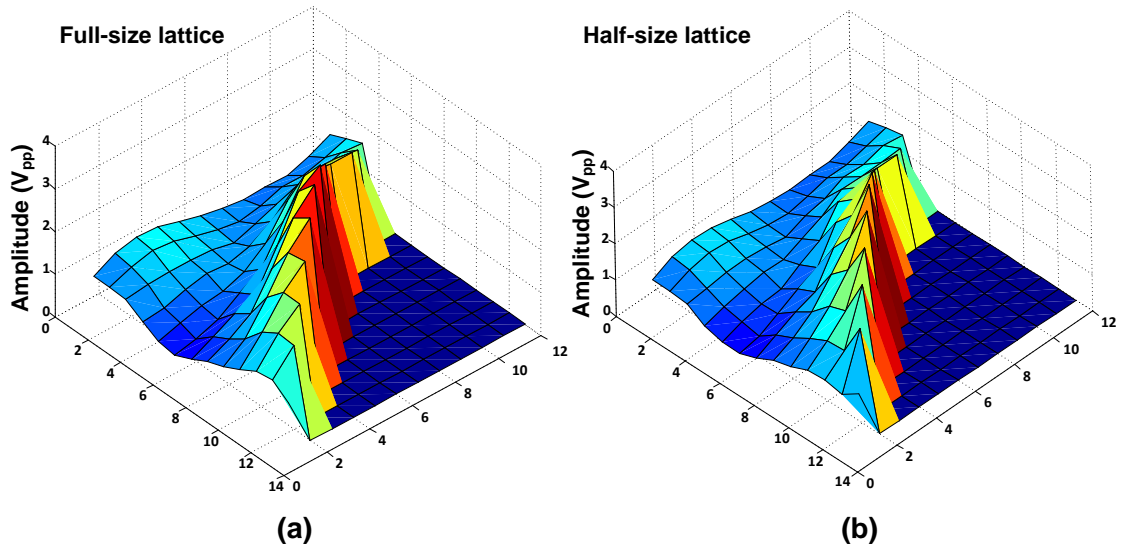
Figure 5.25: Amplitude profile in (a) a full-size lattice and (b) a half-size lattice (we only plot the upper half even for a full-size lattice.)

5.7   Conclusion

In this chapter, we have demonstrated the generation of very narrow and high-amplitude pulses using a nonlinear 2-D lattice in a lossy CMOS process. This has been accomplished by exploiting the constructive interference of two plane waves traveling perpendicular to each other in an optimally-designed nonlinear medium. Despite its large chip area, the nonlinear lattice enables picosecond pulse generation in a standard CMOS process, opening a new door to several new applications, such as millimeter-wave imaging, spectroscopy, and ultra-wideband systems.

BIBLIOGRAPHY

[1] P. H. Siegel,"Terahertz Technology," *IEEE Trans. Microwave Theory Tech.*, vol. 50, no. 3, pp. 910-928, Mar. 2002.

[2] M. Kahrs, "50 years of RF and microwave sampling," *IEEE Trans. Microwave Theory Tech.*, vol. 51, no. 6, pp. 1787.1805, Jun. 2003.

[3] J. B. Jackson, et al.,"Terahertz Time-Domain Reflectometry Applied to the Investigation of Hidden Mural Paintings," in *CLEO/QELS 2008*, May, 2008.

[4] T. W. Crow, et al.,"Opening the Terahertz Window with Integrated Diode Circuits" *IEEE J. Solid-Stat Circuits*, vol. 40, no. 10, pp. 2104-2110, Oct. 2005.

[5] W. Vereecken and M. Steyaert, "Ultra-Wideband Pulse-based Radio" *Ulta-Wideband Pulse-baded Rngineering*, Springer, New York, 2009.

[6] L. F. Mollenauer, R. H. Stolen, J. P. Gordon, and W. J. Tomlinson, "Extreme Picosecond Pulse Narrowing by Means of Soliton Effect in Single-mode Optical Fibers," *Optics Letter*, vol. 8, no. 5, pp. 289-291, May 1983.

[7] J. R. Alday, "Narrow pulse generation by nonlinear transmission lines," *Proc. IEEE*, vol. 22, no. 6, pp. 739, Jun 1964.

[8] D. Jaeger and F.J. Tegude, "Nonlinear Wave Propagation along Periodic-Loaded Transmission Line," *Appl. Phys.*, vol. 15, pp. 393-397, Apr. 1978.

[9] E. Carman, M. Case, M. Kamegawa, R. Yu, K. Giboney, and M. J. W. Rodwell, "V-Band and W-Band Broad-Band, Monolithic Distributed Frequency Multipliers," *IEEE Microwave Guided Wave Lett.*, vol. 2, no. 6, pp. 253-254, June 1992.

[10] D. Jaeger, "Characteristics of travelling waves along the nonlinear transmission lines for monolithic integrated circuits: a review" *INT. J. Electronics*, vol. 58, no. 4, pp. 649-669, 1985.

[11] M. J. W. Rodwell, M. Kamegawa, R. Yu, M. Case, E. Carman, and K. Giboney, "GaAs nonlinear transmission lines for picosecond pulse generation and millimeter-wave sampling," *IEEE Trans. Microwave Theory Tech.*, vol. 39, no. 7, pp. 1194-1204, Jul. 1991.

[12] M. Case, M. Kamegawa, R. Yu, M. J. W. Rodwell, and J. Franklin, "Impulse compression using soliton effects in a monolithic GaAs circuit," *Appl. Phys. Lett.*, vol. 58, no. 2, pp. 173-175, Jan. 1991.

[13] E. Afshari and A. Hajimiri, "Nonlinear Transmission Lines for Pulse Shaping in Silicon," *IEEE J. Solid-Stat Circuits*, vol. 40, no. 3, pp. 744-752, Mar. 2005.

[14] G. N. Lilis, J. Park, W. Lee, G. Li, H. S. Bhat, and E. fshari, "Harmonic Generation Using Nonlinear LC Lattices," *IEEE Trans. Microwave Theory Tech.*, vol. 58, no. 7, pp. 1713-1723, July. 2010.

[15] H. S. Bhat, E. Afshari, "Nonlinear constructive interference in electrical lattices",*Phys. Rev. E*, Vol. 77, No. 6, pp. 066602 1-13, June 2008.

[16] H. S. Bhat, W. Lee, G. N. Lilis, and E. Afshari,"Steady-State Perturbative Theory for Nonlinear Circuits," *Journal of Physics A: Math. Theor.*, vol. 43, no. 20, May 2010.

[17] W. Lee, F. Amoozegar, and E. Afshari,"Picosecond Pulse Generation on CMOS: Design Beyond Transistor Limits," Proc. of IEEE Radar Conference, May 2009.

[18] D. S. Ricketts, X. Li, N. Sun, K. Woo, and D. Ham,"On the Self-Generation of Electrical Soliton Pulse," *IEEE J. Solid-Stat Circuits*, vol. 42, no. 8, pp. 1657-1668, Aug. 2007.

[19] O. O. Yildirim, D. Ha, and D. Ham,"Fully Monolithic 18.7 GHz 16 ps GaAs Mode-Locked Oscillator" *Proc. of IEEE RFIC Symposium 2011*, Baltimore, Maryland, USA

[20] H. Wu and A. Hajimiri, "Silicon-Based Distributed Voltage Controlled Oscillator," *IEEE J. Solid-Stat Circuits*, vol. 36, no. 3, pp. 493-502, Mar. 2001.

[21] O. Momeni and E. Afshari, "Electrical Prism: A High Quality Factor Filter for Milimeter-Wave and Terahertz Frequencies," *IEEE Trans. Microwave Theory Tech.*, vol. 57, no. 11, pp. 2790-2798, Nov. 2009.

[22] E. Okutsu and L. Schott, "Nonlinear interference of ion acoustic waves," *Plasma Phys.*, vol. 23, no. 10, pp. 955-961, 1981.

[23] T. Soorapanth, C. P. Yue, D. K. Shaeffer, T. H. Lee, and S. S. Wong, "Analysis and Optimization of Accumulation-Mode Varactor for RF ICs," in *IEEE Symp. VLSI Circuits Dig. Tech. Papers,* June 1998, pp. 32-33.

[24] S. Song and H. Shin, "An RF Model of the Accumulation-Mode MOS Varactor Valid in Both Accumulation and Depletion Regions" *IEEE Tran. Electron Devices*, vol. 50, no. 9, pp. 1997-1999, Sep. 2003.

[25] Chien-Chih Ho, et al."0.13-um RF CMOS and Varactors Performance Optimization by Multiple Gate Layouts," *IEEE Tran. Electron Devices*, vol. 51, no. 12, pp. 2181-2185, Dec. 2004.

[26] A. Niknejad and H. Hashemi, *mm-Wave Silicon Technology 60 GHz and Beyond*, Springer, New York, NY, 2007.

[27] D.M. Pozar, *Microwave Engineering*, Wiley, New York, NY, 2005.

[28] Chien-Chih Ho, et al."0.13-um RF CMOS and Varactors Performance Optimization by Multiple Gate Layouts," *IEEE Tran. Electron Devices*, vol. 51, no. 12, pp. 2181-2185, Dec. 2004.

[29] *CMRF8SF Model Reference Guide*, IBM Microelectronics Division, Apr. 2007.

[30] L.E. Myers, R.C. Eckardt, M.M. Fejer, and R.L. Byer, "Quasi-Phase-Matched Optical Parametric Oscillators in Bulk Periodically Poled *LiNbO$_3$*," *J. Opt. Soc. Am. B*, vol. 12, no. 11, pp. 2102-2116, Nov. 1995.

[31] G.M. Roe and M.R. Boyd, "Parametric Energy Conversion in Distributed Systems," *Proc. IRE*, vol. 47, pp. 1213-1218, Jul. 1959.

[32] R. Landauer, "Parametric Amplification Along Nonlinear Transmission Lines," *Journal of Applied Physics*, vol. 31, pp. 479-484, 1960.

[33] Agilent 86116C, http://cp.literature.agilent.com/litweb/pdf/5989-8359EN.pdf.

[34] T.H. Lee, *The Design of CMOS Radio-Frequency Integrated Circuits*, Cambridge, New York, NY, 2004, p.262.

CHAPTER 6

CONCLUSION

In this study, we have applied interesting nonlinear phenomena, mostly studied in optics and physics, to CMOS analog circuit design in order to overcome the performance limit in noise, speed, and power. Using this concept, we have demonstrated passive frequency division, noise squeezing, and nonlinear pulse generation.

To reduce the overall system power and phase noise in high-speed frequency synthesizers, we have proposed a new frequency divider that can operate at high frequencies with very low noise without any DC power consumption. In this circuit, the oscillation at target frequency is sustained by the energy injection from input signal through parametric amplification, instead of noisy and power-consuming transistors. Based on this concept, a passive 20-GHz frequency divider with close to ideal noise performance was implemented in a CMOS process for the first time. In terms of power efficiency and phase noise, this is better than the widely used injection-locked frequency division.

Next, to achieve sensitivity toward the thermal noise limit, we have demonstrated noise squeezing in electrical circuits for the first time. By exploiting degenerate parametric amplification, in which a pump at twice the signal frequency supplies energy to or extracts energy from the signal depending on the phase difference, we proposed a method to trade the amplitude and phase noise, squeezing the circular noise portrait into an oval shape. In other words, we can enhance the sensitivity of one signal aspect (e.g., the phase or in-phase component) at the expense of degrading the other orthogonal aspect (e.g., the amplitude or quadrature component). The first prototype was a 10-GHz CMOS

low-noise amplifier with a sensitivity enhancement factor(i.e., squeezing factor) of 2.5 dB for one quadrature phase.

Lastly, we have demonstrated the generation of very narrow and high-amplitude pulses using a nonlinear lattice in a lossy CMOS process. Narrow pulse generation with a sufficient power level is essential in high data rate sampling, time-domain reflectometry, sensing and imaging, spectroscopy, and pulse-based wireless communication. For high-amplitude sharp pulse generation, we proposed to use the nonlinear wave interaction in a two-dimensional electrical medium. In this system, when two waves collide orthogonally, they combine in a nonlinear fashion: The amplitude of the outgoing wave is greater than the sum of the incoming waves with much higher frequency components. After analyzing this concept, we demonstrated a 2.7-V pulse generation with a 6-ps pulse width from a 22-GHz input in a standard 130-nm CMOS process. To the best of our knowledge, regarding the high-amplitude pulses, this work shows the sharpest pulse in any CMOS process.